1-1-2013

Directed Synthesis and Doping of Wide Bandgap Semiconducting Oxide Nanocrystals

Thomas Ross Gordon
University of Pennsylvania, tgor@sas.upenn.edu

Directed Synthesis and Doping of Wide Bandgap Semiconducting Oxide Nanocrystals

Abstract
Wide bandgap semiconducting oxide nanocrystals are a useful class of materials with high stability and numerous useful properties. In the field of catalysis, high surface area oxides are commonly used as catalytic supports and have been found to be photocatalytically active for the production of renewable fuels. Ultra high vacuum studies of single crystals indicate that the surface structure and faceting of oxides dramatically influence their catalytic properties. For plasmonics applications, degenerately doped oxide nanocrystals may act as low-loss substitutes for metals, but little is known regarding the influence of particle shape or assembly on their optical response. With the discovery of nonaqueous surfactant assisted synthesis, methods to produce nanocrystals which provide precise control over size, shape, and crystal structure have improved dramatically. On the other hand, exploration of the influence of morphology on the properties of many materials, including wide bandgap oxide materials, is only in its infancy. Herein, improved methods are described to control both the size and shape of semiconducting oxide nanocrystals. The influence of nanocrystal shape on the photocatalytic activity for hydrogen evolution and other environmentally relevant reactions is then described, as well as the shape dependent plasmonic response and dielectric properties of conductive oxide nanocrystals.

Degree Type
Dissertation

Degree Name
Doctor of Philosophy (PhD)

Graduate Group
Chemistry

First Advisor
Christopher B. Murray

Keywords
Doping, Nanocrystals, Oxides, Photocatalysis, Plasmonics, Shape Control

Subject Categories
Nanoscience and Nanotechnology | Physical Chemistry

DIRECTED SYNTHESIS AND DOPING OF WIDE BANDGAP SEMICONDUCTING OXIDE NANOCRYSTALS

Thomas Ross Gordon

A DISSERTATION

in

Chemistry

Presented to the Faculties of the University of Pennsylvania

in

Partial Fulfillment of the Requirements for the

Degree of Doctor of Philosophy

2013

Supervisor of Dissertation

_____

Dr. Christopher B. Murray
Richard Perry Professor of Chemistry and Materials Science and Engineering

Graduate Group Chairperson

_____

Dr. Gary A. Molander
Hirschmann-Makineni Professor of Chemistry

Dissertation Committee

Dr. Larry G. Sneddon, Blanchard Professor of Chemistry (CHAIR)

Dr. Donald H. Berry, Professor of Chemistry

Dr. Andrew M. Rappe, Professor of Chemistry

DIRECTED SYNTHESIS AND DOPING OF WIDE BANDGAP SEMICONDUCTING OXIDE NANOCRYSTALS

To my wife and family…

ACKNOWLEDGMENT

This work would not have been possible without contributions from many incredible individuals. First and foremost, I'd like to thank Prof. Christopher Murray, my advisor, who made the completion of this work possible. Chris gave me incredible freedom to pursue my own interests, but was also always available to give valuable advice. His passion for science is truly an inspiration to me. Also, I'd like to thank every member of the Murray group. First, to the "original 7," Ko, Xingchen, Jun, Weon-kyu, Yijin and Danielle. We had the tough job of setting up the lab, but in the end, we pulled it off. And to, Ben, Ashley, Hong-seok, JBP, Nick, Chen, Bianca, Amy, and Don, thank you all for your contributions to my research, but also to making lab life an enjoyable and amusing experience.

I'd like to thank DKKo, for agreeing to spend hours teaching me how to operate the 2010F (the Korean way), a process which continues in his absence. Also, he introduced me to the magic of Koreana and the horror of K-pop, and always found the perfect way to shatter my dreams while also motivating me to work harder. Thank you to Vicky for her group therapy sessions which included intense commiseration, as well as for helping me learn to code. The appendix of this thesis would not have been possible without her help in debugging or declarations to int that! TJ Paik was an incredibly important contributor to this thesis work. I thank him for encouraging me to aim high, while also questioning every part of my work. He was willing to help with any measurement and coached me in how to craft my research into a cohesive story. I also thank Matteo, PhDude, who completely turned my research around when he joined our lab. I am always mesmerized and inspired by Matteo's optimistic spirit and his ability to consistently lead by example. In addition, I am amazed by the array of English words he is capable of inventing for a particular purpose (e.g. helpy, gerarchy, solidal, etc.). Matteo has been an incredible collaborator, mentor, and friend, and this work truly would not have been possible without his contributions.

There are also several undergraduates and masters students who contributed to this thesis work. I thank Dahlia for her contributions to the work in chapters 4 and 5. She picked up lab work incredibly quickly, and always wanted to understand the big picture, which contributed to her success. My estimation is that she may one day rule the world, let's just hope she is a benevolent leader. I thank Yupeng for contributions to chapter 2 in synthesizing TiO_2 nanorods and running catalytic reactions, it was great to have an extra set of hands around to pursue this work. Also, Abdul Rahman-Raji was an REU student who spent a summer making ZnO and contributed significantly to the results in chapter 3.

I also had many contributors and friends from outside of my lab whom I'd like to thank. Thank you to Prof. Cherie Kagan and the entire Kagan lab for their support during the progression of my Ph.D. Special thanks to Aaron, David, Ed, and Eric for enjoyable trips to Koreana and for generally letting the good times roll. I also appreciate the support of Prof. Paolo Fornasiero in Trieste, Italy who supported many catalytic studies. In addition, my collaborators for the work involving metamaterials, including Prof. Nader Engheta and Dr. Humeyra Caglayan at Penn and Gururaj Naik and Prof. Alexandra Boltasseva at Purdue University who helped me begin to understand this intriguing field. Also at Penn, the Saven group, including Prof. Saven, Chris, and Will are acknowledged for providing protein samples and helping to make the work in chapter 5 possible. I'd also like to thank Dr. Susan Phillips for supporting my teaching endeavors at Penn and inspiring me to pursue undergraduate education.

Finally, I'd like to thank all my friends at Penn and from home who have supported me throughout my time in graduate school. The process took a lot out of me, but you all were always there to provide support when needed. I especially want to thank my entire family who are a huge source of inspiration and encouragement in my life. My sister, Erica, is truly one of my biggest fans and I greatly value all of her love and support throughout the years. I also would like to thank my in-laws, Terri and Nick, who were ever encouraging during my studies. Thank you to my mom for encouraging me to get involved in science early on and for always believing in the best of me.

Thank you to my dad, who taught me to never stop searching until I'm satisfied and made my research feel more important by always trying to understand it. And finally, to the love of my life, Kate, you are my world and I can't imagine life without you. Thank you for making this work possible through your love and commitment over our years together.

"Imagination will often carry us to worlds that never were. But without it we go nowhere."

Carl Sagan, *Cosmos*

ABSTRACT

DIRECTED SYNTHESIS AND DOPING OF WIDE BANDGAP SEMICONDUCTING OXIDE NANOCRYSTALS

Thomas Ross Gordon

Dr. Christopher Bruce Murray

Wide bandgap semiconducting oxide nanocrystals are a useful class of materials with high stability and numerous useful properties. In the field of catalysis, high surface area oxides are commonly used as catalytic supports and have been found to be photocatalytically active for the production of renewable fuels. Ultra high vacuum studies of single crystals indicate that the surface structure and faceting of oxides dramatically influence their catalytic properties. For plasmonics applications, degenerately doped oxide nanocrystals may act as low-loss substitutes for metals, but little is known regarding the influence of particle shape or assembly on their optical response. With the discovery of nonaqueous surfactant assisted synthesis, methods to produce nanocrystals which provide precise control over size, shape, and crystal structure have improved dramatically. On the other hand, exploration of the influence of morphology on the properties of many materials, including wide bandgap oxide materials, is only in its infancy. Herein, improved methods are described to control both the size and shape of semiconducting oxide nanocrystals. The influence of nanocrystal shape on the photocatalytic activity for hydrogen evolution and other environmentally relevant reactions is then described, as well as the shape dependent plasmonic response and dielectric properties of conductive oxide nanocrystals.

TABLE OF CONTENTS

ACKNOWLEDGMENT ..... **IV**

ABSTRACT ..... **VII**

LIST OF TABLES ..... **XI**

LIST OF ILLUSTRATIONS ..... **XI**

1. INTRODUCTION **1**

1.1 Nanocrystalline Wide Bandgap Semiconducting Oxides **1**

1.1.1 Properties and Uses 1

1.1.2 Aqueous Synthetic Techniques 3

1.1.3 Nonaqueous Synthetic Techniques 6

1.1.4 Doping Oxide Nanocrystals 11

1.2 Photocatalysis **14**

1.2.1 Introduction 14

1.2.2 Measurement Techniques 19

1.2.3 Surface Structure 20

1.3 Transparent Conducting Oxide Nanocrystals **22**

1.3.1 Introduction and Materials 22

1.3.2 Transparent Conducting Oxide Films 23

1.3.3 Plasmonic Oxide Nanocrystals 24

1.3.4 Metamaterials 26

1.4 Materials Characterization Techniques **28**

1.4.1 Electron Microscopy 28

1.4.2 X-ray Scattering and Simulation 29

2. TITANIUM DIOXIDE NANOCRYSTALS **32**

2.1 Introduction 32

2.2 Using TiF_4 to Engineer Morphology and Photocatalytic Activity 35

2.2.1 Introduction 35

2.2.2 Experimental 37

2.2.3 Results and Discussion 45

2.2.4 Conclusions 75

2.3 Ultrathin Anatase Nanorods 77

2.3.1 Introduction 77

2.3.2 Experimental 78

2.3.3 Results and Discussion 80

2.3.4 Conclusions 88

2.4 Highly Photocatalytically Active Brookite TiO_2 Nanorods 89

2.4.1 Introduction 89

2.4.2 Experimental 90

2.4.3 Results and Discussion 93

2.4.4 Conclusions 100

2.5 Future Work 101

3. ZINC OXIDE NANOCRYSTALS 102

3.1 Synthesis of Uniform Zinc Oxide Building Blocks 102

3.1.1 Introduction 102

3.1.2 Experimental 103

3.1.3 Results and Discussion 105

3.1.4 Conclusions and Future Work 110

4. DOPED CADMIUM OXIDE NANOCRYSTALS 112

4.1 Shape Directed Plasmonic Response in Cadmium Based TCOs 112

4.1.1 Introduction 112
4.1.2 Experimental 116
4.1.3 Results and Discussion 118
4.1.4 Conclusions 135
4.2 Tunable Metallic Thin Films from TCO Nanocrystal Precursors 136
4.2.1 Introduction 136
4.2.2 Experimental 138
4.2.3 Results and Discussion 139
4.1.4 Conclusions 146
4.3 Future Work 147
5. PROTEIN-NANOCRYSTAL HYBRIDS 148
5.1 Soluble Gold-Protein-Cofactor Complexes for Enhanced Fluorescence 148
5.1.1 Introduction 148
5.1.2 Experimental 150
5.1.3 Results and Discussion 152
5.1.4 Conclusions and Future Work 158
6. CONCLUSIONS 159
7. APPENDIX A – X-RAY SCATTERING SIMULATION CODE 162
8. BIBLIOGRAPHY 181

LIST OF TABLES

Table 1: Particle size of 3 anatase TiO_2 NC samples based on statistical analysis of TEM images and best fitting XRD pattern and derived percentages of {001} and {101} facets and surface area. 58

Table 2: Tabulated XPS results for three samples of blue TiO_2 NCs deposited on Si wafers and subjected to 4 min of Ar ion plasma. 66

Table 3: Textural properties of the fluorinated and NaOH-treated samples. [a]According to BET method. [b]The surface area calculated as described in figure S4. For F-ODOL, size parameters are estimated from TEM analysis to be L = 12.4 nm, W = 80.1 nm. [c]According to BJH method, maximum of the pore size distribution taken from the desorption branch. 73

Table 4: Properties of ICO NCs determined by ICP and UV-Vis-NIR spectroscopy. 125

Table 5: Table of optical information extracted from several samples of spherical ICO nanocrystals. Γ is the FWHM of the peak at the resonance wavelength. The quality factor is defined as $QF = \omega max/\Gamma$, where ω_{max} is the photon energy at the LSPR maximum. 131

LIST OF ILLUSTRATIONS

Figure 1: A) La Mer plot, along with cartoon depicting the stages of nucleation and growth for the preparation of monodisperse NCs in the framework of the La Mer model. Courtesy of C. B. Murray[27] (B) Representation of the simple synthetic apparatus employed in the preparation of monodisperse NC samples. 8

Figure 2. Energy diagram for the photosynthetic water splitting in which an electron and hole form due to photooxidation, the electron reduces protons to hydrogen and oxidizes water to oxygen. 16

Figure 3. Photocatalytic gas reactor with online gas chromatography. 20

Figure 4. Plotted real (ε_1) and imaginary (ε_2) parts of permittivity for the Drude model of metals. 25

Figure 5: Unit cells of the three polymorphs of TiO_2, rutile, anatase, and brookite. 33

Figure 6: Typical spectral output (black) of a solar simulator (there is negligible output from 250-300 nm) and standard AM1.5G spectrum(blue). 41

Figure 7: Representative TEM image of anatase TiO_2 seeds formed at 290°C before addition of stock solution. 46

Figure 8. TEM images of TiO_2 nanocrystals synthesized using the precursor TiF_4 (a,d) a mixed precursor of TiF_4 and $TiCl_4$ (b,e) and $TiCl_4$ (c,f). Those depicted in a – c and d – f are synthesized in the presence of OLAM and 1-ODOL, respectively..... 46

Figure 9: HRTEM images of samples a) F–OLAM, b) F–ODOL, c) M–OLAM, and d) Cl–OLAM. 48

Figure 10: Representative TEM images of particle growth of sample F-OLAM as function of time with addition of F stock solution at 0.3 mL min^{-1}. 49

Figure 11: a) TEM image of $TiOF_2$ nanocrystals, inset shows HRTEM image of a single $TiOF_2$ NC and a unit cell of hexagonal $TiOF_2$ (space group R-3c), where grey atoms are Ti, light blue atoms are F and red atoms are O (oxygen and fluorine atoms reside on the same sites in a random configuration). b) XRD pattern of $TiOF_2$ nanocrystals compared with cubic (PDF#77-0132) and hexagonal[183] $TiOF_2$ patterns from the literature. 52

Figure 12: Actual atomistic models used in X-ray simulations, which represent the average NC size in the labeled sample. 55

Figure 13. Experimental XRD patterns (thick black lines) plotted with simulation (thin colored lines) for TiO_2 nanocrystals a) M-OLAM, b) F-OLAM and c) M-ODOL. 56

Figure 14: Model of perfect tetragonal bipyramid with labels indicating measured dimensions. 57

Figure 15: XRD patterns for samples a) Cl-OLAM and b) F-ODOL, and c) Cl-ODOL. 59

Figure 16. a) Optical absorption of sample F-OLAM dispersed in CCl_4 (dashed line at 2500 nm indicates where data is joined) and b) EPR spectra of sample F-OLAM at several temperatures. Inset of a) shows proposed band diagram of blue TiO_2 nanocrystals and an optical image of TiO_2 nanocrystals dispersed in toluene. 60

Figure 17: Diffuse reflectance spectra covering the UV-Vis-NIR (300 – 2000 nm) of TiO_2 NCs synthesized in a) OLAM and b) 1-ODOL. 61

Figure 18: EDS spectrum of sample F–ODOL 64

Figure 19: a) XPS survey spectrum and b) high resolution XPS spectrum of the F 1s peak for sample F-OLAM. 65

Figure 20: HR XPS spectra of the (a-c) F 1s and (d-f) Ti 2p peaks for samples (a,d) M-OLAM, (b,e) F-OLAM, and (c,f) F-ODOL. 66

Figure 21. Hydrogen production rate from 1 wt. % Pt loaded samples of ligand exchanged, a) fluorinated and b) NaOH-treated TiO_2 NCs under solar illumination in 1:1 mixtures of MeOH:H_2O. Samples are M-OLAM (green triangles), M-ODOL (black circles) and F-ODOL (blue squares). 68

Figure 22: Hydrogen production rate from 1 wt. % Pt loaded samples of ligand exchanged TiO_2 nanocrystals under simulated solar illumination in 1:1 mixtures of MeOH:H_2O. Samples are M-OLAM (blue triangles), F-OLAM (green circles), M-ODOL (red diamonds) and F-ODOL (black squares). 70

Figure 23: H_2 production rate for methanol photoreforming under simulated solar irradiation over fluorinated M-OLAM with 0.1 wt. % Pt (green triangles) or 1.0 wt. % Pt (red squares) loadings. 71

Figure 24: TEM images of samples a) M-OLAM and b) F-ODOL loaded with 1 wt. % Pt after 15 hours of photoreforming reaction in the presence of methanol. 72

Figure 25: Reaction mechanism describing the (1) formation of carboxylate from TTIP and oleic acid and (2) aminolysis of the carboxylate to form hydroxylated Ti centers and an oleyl amide byproduct. 81

Figure 26: TEM images of anatase TiO_2 nanorods (a) before and (b-d) after size selective precipitation, where b is the first fraction separated, and d is the last fraction. 82

Figure 27: A) SAXS data with Debye simulation plotted and B) WAXS pattern of anatase TiO_2 nanorods with HRTEM as inset. 84

Figure 28: Self-assembled structures of TiO_2 nanorods, indicating A) lamellar type assembly and B) hexagonally close-packed vertical alignment. 85

Figure 29: TEM images of TiO_2 nanorods A) as synthesized and B) after $NOBF_4$ treatment. 86

Figure 30: Temporal progression of methylene blue absorbance during photocatalysis in the presence of ultrathin anatase nanorods. 87

Figure 31: Synthetic schemes for two methods of producing brookite nanorods. 94

Figure 32: TEM images of brookite nanorods produced by seeded growth after 8 mL of stock addition (a,c) and heating up methods (b,d) using stock #2 (a,b) and stock #1 (c,d). 95

Figure 33: TEM images of aliquots taken from a seeded growth reaction using stock #1 (scale bars = 100nm) 96

Figure 34: Experimental XRD patterns, simulation prepared using the Debye equation, and standard PDF patterns for brookite nanorods produced using seeded growth and A) stock solution #1 and B) stock solution #2. 98

Figure 35: Hydrogen production rates from 1 wt. % Pt loaded samples of ligand-exchanged brookite nanorods and one sample of anatase under UV illumination in 1:1 mixtures of MeOH:H_2O. Triangle and circle are heating-up method with stock #2 and #1, respectively. Square is seeded growth, stock #1 and the star is M-OLAM from section 2.2.3. 99

Figure 36: ZnO nanocrystals produced using synthesis I, using a) 1,2-DDIOL and b) using 1-octadecanol. 106

Figure 37: TEM images of a) undoped and b) Co-doped ZnO nanocrystals with insets showing photographs of the particle solutions. c) Absorbance and d) photoluminesence from ZnO nanocrystal solutions and e) WAXS patterns of undoped and doped ZnO nanocrystals. 107

Figure 38: TEM images of ZnO nanocrystals produced using synthetic method II a) as a monolayer and b) assembled into a hexagonally close packed superlattice, inset shows electron diffraction pattern indicating hexagonal packing. c) Absorbance and photoluminescence spectra of ZnO nanocrystals synthesized using synthetic method II dispersed in hexanes. 110

Figure 39: TEM images of octahedral ICO nanocrystals produced at 300 °C using a) 4 mmol and b) 3 mmol OLAC and SEM image of sample shown in b). TEM image of spherical nanocrystals produced at reflux using d) 5 mmol and e) 3 mmol OLAC. f) The unit cell of rock-salt type indium doped cadmium oxide (ICO). 120

Figure 40: Plasmonic optical response (A), and TEM images (B, C) of tin doped cadmium oxide nanocrystals with octahedral and spherical morphology. 121

Figure 41: TEM tilt series confirming the octahedral geometry of the ICO nanocrystals, shown for A) tilting in the positive x direction and B) tilting in the negative x direction. 122

Figure 42: SAXS and WAXS patterns for a) 51 nm (tip-to-tip) octahedral ICO nanocrystals dispersed at 10 wt. % in polyvinyl butyral and b) 8 nm spherical ICO nanocrystals dispersed in CCl_4 and loaded into a glass capillary. 123

Figure 43: a) Solution phase spectra of ICO nanocrystals dispersed in CCl_4 for 5 levels of % atomic doping of In (inset shows the blue shift of the bandgap with increasing In content). b) Solution phase spectra of three shapes/sizes (spherical, small octahedral and large octahedral) of nanocrystals with similar levels of In doping, where the TEM image above each image corresponds to the sample measured optically (scale bar = 50 nm). c) Solution phase spectra of ICO nanocrystal sample dispersed in CCl_4, TCE, and CS_2, with inset indicating the wavelength shift. d) Plot of LSPR wavelength with increasing In content for octahedral and spherical nanocrystals. 124

Figure 44: Optical absorbance of four samples of ICO octahedra with different concentrations of indium. 125

Figure 45: Plots of $(\alpha h\nu)^2$ vs. photon energy (eV) for 5 samples of spherical ICO NCs. Open circles are measured data, dotted lines are linear fits, and the legend shows the extracted direct bandgap energies. 127

Figure 46: Calculated extinction coefficients simulated with FDTD using values of permittivity for ICO extracted using spectroscopic ellipsometry. 130

Figure 47: Plot of resonance wavelength vs. refractive index of solvent for a single sample dispersed in 3 different solvents. 133

Figure 48: Self assembled structures formed at a liquid-air interface. a, b) SEM images of ICO octahedra, forming 3-D Minkowski-type superlattice structures. c) Long range [001] projection of an $MgZn_2$-type BNSL of 8 nm ICO nanocrystals and 5 nm PbSe nanocrystals, inset shows electron diffraction pattern of BNSL. Depictions of the d) unit cell and e) [001] projection of the $MgZn_2$-type BNSL. e) Higher magnification TEM image of BNSL. 134

Figure 49: A) NIR/IR transmission spectra of 10% ICO nanocrystals dissolved in CCl_4 solution, as deposited on quartz, and after annealing. *indicates C-H vibrations from surfactants on particle surfaces. B) NIR/IR transmission spectra and reflectance spectra for 10% ICO nanocrystals as deposited on quartz, and after annealing. C) Photograph of ICO nanocrystal films before (left) and after (right) annealing. 140

Figure 50: Simulated optical constants for optical models of TCO films, a) Lorentz-Lorentz and b) Drude-Lorentz. 143

Figure 51: Extracted complex permittivity for films of 10, 15, and 20% ICO a) before and b) after annealing. 144

Figure 52: a) TEM image, absorbance spectrum and photographs of highly monodisperse gold nanorods with tunable longitudinal plasmonic resonance peaks, ranging from 600 to 900 nm. b) Chemical structure of diphenylporphyrin zinc (PZn) and RuPZn and an artistic representation of a computationally designed protein with two PZn molecules bound within it. 153

Figure 53: Schematic diagram for assembly of the nanorod-protein complex. . 155

Figure 54: b) Optical absorbance (dark green) and emission spectra at 419 nm excitation (light green) of the PZn cofactor bound to the protein and the extincation spectrum of two different samples of gold nanorods with different aspect ratios. a) Time-resolved photoluminescence of the PZn fluorophore in DMSO. 156

Figure 55: Optical absorbance of buffer-soluble gold-protein-cofactor heterostructure. 157

1. INTRODUCTION

1.1 Nanocrystalline Wide Bandgap Semiconducting Oxides

1.1.1 Properties and Uses

The discovery and utilization of semiconductors has truly revolutionized modern life. While electricity fundamentally changed everyday activities, the discovery of semiconductors enabled the technological advances which have transformed our society into the vibrant, interconnected one it is today. Semiconductors are basis of computing, allowing for the storage of binary data in transistors, but this is only one of many uses. They also are central to important devices and applications such as switches, photovoltaics, light emitting diodes (LEDs), photocatalysis, smart windows, sensors, photodetectors, thermoelectrics, and many, many more.

The bandgap of a semiconductor, which is equivalent to the HOMO-LUMO gap in chemical terms, is arguably its most important feature and is often used to classify a given semiconductor.[1,2] Semiconductors are often referred to as narrow or wide bandgap depending on the energetic spacing of the bandgap, with the value of 1 eV representing an approximate cross over point. Narrow bandgap semiconductors often are utilized in thermoelectrics or infrared photodetectors, applications in which the materials must have appreciable thermal carriers at

moderate temperatures.[3] Wide bandgap materials, in contrast, must typically be doped or illuminated in order to observe interesting properties.

In this thesis, I will primarily be discussing the properties of a certain class of wide bandgap semiconductors, transition metal oxides, excepting those with magnetic properties. Many transition metal oxides have very large bandgaps (> 3 eV) relative to conventional semiconductors, such as Si (1.1 eV). In fact, many of the oxides I will discuss are often referred to as insulators or dielectrics, because under many circumstances they have negligible conductivities. Despite this fact, transition metal oxides find many applications, and are among the most heavily studied and mass produced materials in the world. Much of this stems from the high stability of oxide materials. Phosphides, chalcogenides and other classes of semiconductors have often been shown or predicted to show high performance are doomed by stability issues, particularly to oxidation.[4,5] Oxides, in contrast, are typically far less susceptible to oxidation and can persist even under extreme conditions, for instance, in solid oxide fuel cells which operate at temperatures in excess of 600 °C.[6] Oxide materials are currently used ubiquitously in consumer products and in industry, including in the following applications[7]:

1) Catalytic support materials[8]
2) Pigments/Coatings[9,10]
3) Cosmetics[11]

4) Photovoltaics[12]

5) Sensors[13]

6) Fuel Cells[6]

7) Electrochromics[14]

8) Batteries[15]

Research to improve the properties of oxides for these applications and others emerging applications continues to be extremely active.

One strategy towards improving oxide properties is through the engineering of particles at the nanoscale. Nanocrystalline oxide materials, which have particle sizes less than a few hundred nanometers, have been synthesized for many years, but primarily only to provide higher surface area supports for catalysts. Synthetic advances which allow for the production of oxide nanoparticles with precise control over shape, size, and phase has led to discovery of new properties and improved performances. This section will review the solution synthesis of oxide nanoparticles and introduce improved methods using nonaqueous solvents.

1.1.2 Aqueous Synthetic Techniques

Solution dispersible transition metal oxide particles, which are also referred to as colloids, have been synthesized for several decades using well established methods. In industry, gas phase approaches are paramount for the formation of high surface area oxides, due to the low cost of production. Useful

nanocrystalline oxides can be produced using these methods, but control over the particle size and phase of the material is quite limited. For example, Degussa P25 TiO_2 (now produced by Evonik Corp.) is the most heavily studied form of nanocrystalline TiO_2, and is formed through a gas phase method. This material has very high activity for many photocatalytic reactions, but is found to be composed of 78% anatase phase, 14% rutile phase, and some amorphous TiO_2 and contains particles with sizes ranging from 10-100 nm.[16] Such variability in material's composition makes correlation of particle size and properties incredibly difficult. Admittedly, mixed phase materials such as P25 may exhibit better performance than single phases by inducing favorable charge separation, but without the ability to systematically vary the phase and the interactions of those phases at the molecular level, there is little chance of determining the origin of improved performance.[17]

Better control over particle morphology and phase is afforded through liquid phase synthetic methods, which allow for chemical control over the formation of oxides, and will be focus of this thesis.[7] Perhaps the most exploited technique for the synthesis of oxides is the sol-gel process. When first discovered in the 1950s, sol-gel represented a fundamentally different approach to the synthesis of ceramics.[18] For centuries prior, ceramic materials were prepared simply by melting down minerals into homogeneous liquids and molding them into the desired shapes, where crystalline phase was determined

purely by thermodynamics. Sol-gel processing allowed for molecular manipulation of the microstructure of ceramic materials, such that chemical principles could be used to direct the properties of the synthesized material.[18]

The sol-gel method is essentially a polymerization reaction, in which metal complexes, such as alkoxides or chlorides, are the monomer and water is the catalyst.[7] Upon exposure of a metal complex to water, hydrolysis occurs, producing hydroxylated metals which condense to form networks of metal-oxygen linkages. In the early stage, when hydrolysis begins, a sol, or dispersion of colloidal particles, forms. After aging the sol, continued hydrolysis of the metal centers results in the formation of the gel. The gel is typically a viscous mixture composed of a network of amorphous metal oxide particles. In some circumstances, the particles which compose the sol or gel can have very high uniformity and tunable shape depending on the reaction conditions.[19] To induce crystallinity in the amorphous gel, the material usually must be heated to high temperatures (> 600 °C), forming the nanocrystalline oxide powder.[19] The morphology of the nanocrystalline powders is tuned through the various synthesis conditions, including the solution pH, type of metal precursor, anions, organic additives, aging time, and annealing temperature.[19] The major disadvantage of sol-gel processing is the annealing step which is required to form a crystalline material, but is often detrimental to the particle uniformity and morphology.[7,20]

Other popular aqueous phase synthetic techniques to produce transition metal oxides are hydrothermal and solvothermal methods, which rely on high pressure reactors to heat reactions beyond the typical boiling point of their solvents, i.e. to a supercritical state.[21] Similar to sol-gel method, hydrolysis of metal complexes is the most common method to prepare oxide materials under solvothermal/hydrothermal conditions, although direct oxidation of metals can also be accomplished for some materials. The essential difference between the two methods is the solvent utilized in the reaction, where hydrothermal is majority water and solvothermal uses organic solvents. The major advantage of solvothermal/hydrothermal methods is that the resulting materials are typically crystalline as synthesized due to the elevated reaction temperature, and do not require high temperature annealing, as in the case of the sol-gel method. On the other hand, due to a large variability in reactions conditions, reproducibility has been an issue with hydrothermal and solvothermal reactions.

1.1.3 Nonaqueous Synthetic Techniques

The nonaqueous synthesis of oxide particles began in the 1980s, intensified in the 1990s, and was initially a modification of aqueous sol-gel techniques.[7,22] The terms nonaqueous sol-gel and nonhydrolytic sol-gel were coined early on and continue to be used to describe the synthesis of nanocrystals in organic solvents, although they are not always well-distinguished in the literature. Nonhydrolytic sol-gel describes reactions in which an oxide

forms without any involvement from water, through reactions with oxygen-containing organic molecules, while in nonaqueous sol-gel processes hydrolysis occurs with water produced *in situ*.[7] On the other hand, it is important to note that without careful study, it is not always obvious whether water is produced during a given reaction, so the terms are often used interchangeably. One proposed advantage of the nonaqueous approaches is better control over reaction rates than possible in sol-gel chemistry, where hydrolysis typically occurs very quickly and is difficult to modulate.[22] A pioneer of this early work was Andre Vioux, who carefully studied the mechanisms by which metal precursors such as alkoxides and halides react with organic molecules to form oxides in the absence of water.[22] Niederberger, et al. have established a versatile nonhydrolytic sol-gel approach to produce many binary and ternary oxide systems with some control over particle shape and size, primarily using benzyl alcohol as a coordinating solvent.[23] On the other hand, many of these syntheses are also run under solvothermal conditions, requiring elevated pressure.

In parallel to these early investigations of nonaqueous synthetic approaches to oxide materials, novel methods were being developed for the production of other inorganic nanomaterials, particularly semiconductor quantum dots.[24] These methods are commonly referred to as nonaqueous surfactant-assisted synthesis, high temperature colloidal synthesis, and nonhydrolytic colloidal synthesis.[25,26] Whatever term is used, these methods revolutionized the

synthesis of nanocrystals. The reactions are conducted in solutions of high boiling point surfactants and solvents along with metal organic or organometallic precursors at relatively high temperatures (200 – 350°C), typically under an inert atmosphere.[11,26-28] At these elevated temperatures, thermal decomposition of the precursors occurs, resulting in atomic species which polymerize to form the nanocrystals. By adjusting the reaction temperature and type of surfactant, one can effectively tailor the morphology of nanocrystals with better precision and reproducibility than previous methods. The resulting nanocrystals are highly crystalline isolated particles, and are terminated by the surfactants present in the reaction mixture, leading to high solubility in non-polar media.

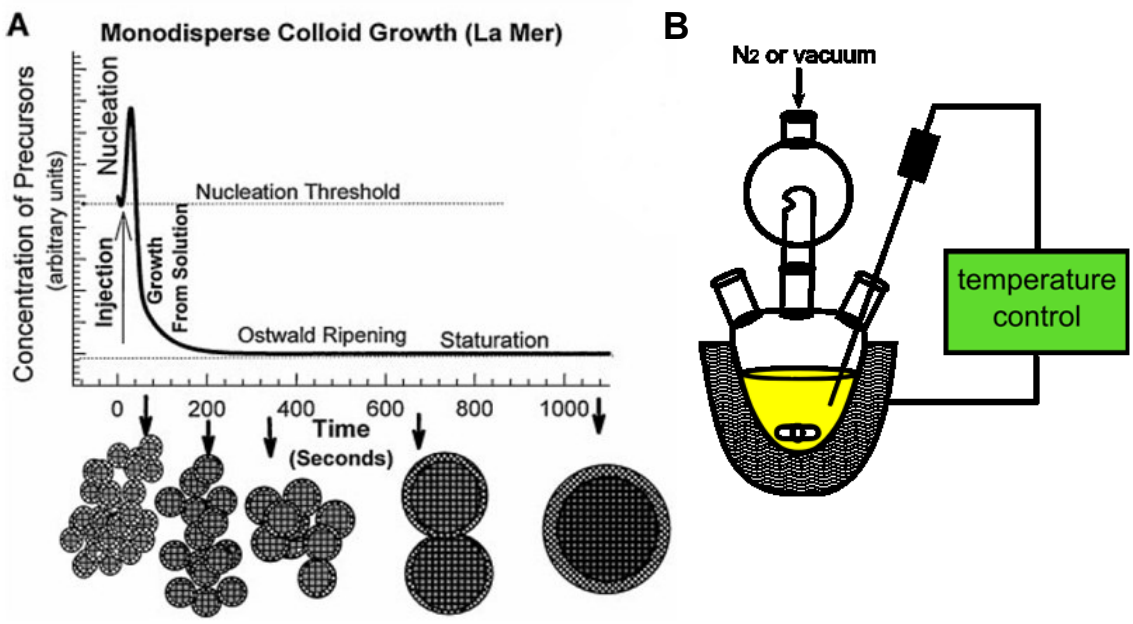

Figure 1: A) La Mer plot, along with cartoon depicting the stages of nucleation and growth for the preparation of monodisperse NCs in the framework of the La Mer model. Courtesy of C. B.

Murray[27] (B) Representation of the simple synthetic apparatus employed in the preparation of monodisperse NC samples.

Much of the improvement in monodispersity can be interpreted in terms of classical nucleation theory or LaMer theory. The hot-injection method, first described by Murray, et al. involved the injection of precursors at high temperature, and subsequent heating at slightly reduced temperature.[24] The quick injection of precursor results in a supersaturation of reactive monomer species to a concentration above the nucleation threshold, leading to nucleation of seed crystals (Figure 1).[27] If the temperature were to remain elevated, nucleation could continue to occur, resulting in polydispersity. By allowing the reaction mixture to cool, nucleation is suppressed, and uniform particle growth occurs instead. With extended reaction time, Ostwald ripening can occur as the concentration of monomers dwindles, and large particles grow at expense of small particles, which preferentially dissolve, leading to polydispersity.[27] Early studies of hot injection methods primarily focused on the synthesis of semiconductor and metal particles.[24,29,30]

The two communities of nonaqueous sol-gel and surfactant assisted synthesis remained separate for some years, until 1999, when two independent reports demonstrated the synthesis of transition metal oxide nanocrystals through nonaqueous surfactant assisted approaches.[31,32] Since that time, surfactant assisted methods have been shown to be suitable for preparing most

material types, including oxides,[32,33] phosphides,[34-36] halides,[37-39] and even ternary compounds.[40-42] In addition, different modifications of the surfactant assisted synthesis were developed, including the heating-up method and seeded growth method.

The heating-up method is a one-pot synthesis, in which the metal organic precursors and surfactants are combined at room temperature and heated to high temperature, simplifying the procedure by eliminating the need for injection. This approach, pioneered by Hyeon, has been particularly useful in the synthesis of highly uniform transition metal oxides.[43-48] Careful study of the kinetics of the heating-up method has revealed that the reaction mechanisms enabling high uniformity also fall within the LaMer model used to interpret hot-injection.[49]

Seeded growth methods were first developed in aqueous solvents for the synthesis of metal particles with uniform size and shape.[50,51] Essentially, seeded growth methods inherently separate nucleation and growth through the initial production of seed particles, followed by the slow addition of a growth solution, forming monomers which deposit on the seeds. This method allows for particle size to be carefully controlled, as demonstrated for iron oxide nanocrystals with size tunable in one nanometer increments.[52] It is also the basis for the preparation of core-shell materials which enable near unity quantum yields for fluorescent quantum dots.[53]

The nonaqueous synthetic methods developed in the past decade not only improved the uniformity of oxide nanoparticles, but are also scalable. Hyeon, et al. have demonstrated several materials for which multi-gram scale quantities of highly uniform particles can be made simply by increasing the reaction size.[44-48,54] This elevates the uniform nanocrystals from series of interesting discoveries to an industrially viable set of materials. In fact, several startup companies and large corporations are currently using nonaqueous surfactant assisted methods for applications in biological imaging, photovoltaics, and light emitting diodes.[55-57]

1.1.4 Doping Oxide Nanocrystals

Doping is the process by which atoms or atomic vacancies are introduced into a crystal lattice either intentionally or unintentionally. In the semiconductor industry, doping is the primary method in which the materials properties are altered, allowing for tuning of the electrical conductivity and carrier type of the material through judicious choice of atomic dopants. For these applications, materials are incredibly sensitive to the addition of small numbers of atomic dopants, with typical intended doping levels being 10^{15} – 10^{18} atoms/cm^3 (0.000001 to 0.001 % atomic doping), thus the need for extremely clean environments for semiconductor processing. In the case of nanocrystals, doping is typically performed at a much higher concentrations, due to the small size of nanocrystals, which contain in the range of 10^3 to 10^6 atoms. In this case, uniform doping at levels typically used in bulk semiconductors would lead to a

large percentage of nanocrystals which are undoped. As a result, much of the doping described in this work could be alternatively referred to as alloying.

Doping of oxide nanocrystals became a topic of interest to improve photocatalytic properties soon after solution methods to oxide synthesis were developed. Some early studies concerned the influence of transition metal dopants on oxide colloids, particularly TiO_2, both the spectroscopically and photochemically.[58-60] At this point, doped colloids were primarily formed through sol-gel methods, in which soluble transition metal compounds were simply added along with titanium precursors prior to preparation of the sol.[61] A comprehensive review of the effects of transition metal dopants on TiO_2 sols revealed that some metals resulted in slightly higher photoactivity for CCl_4 photoreduction, including Fe^{3+} and Mo^{5+}, while others had deleterious effects, acting as trap states.[61] Doping often results in visible light absorption, but rarely does this result in enhanced visible light photoactivity.

More recently, anionic doping of oxides has shown more promise towards enabling visible light photoactivity. In 2001, Asahi, et al. reported enhanced photocatalytic activity from nitrogen doped TiO_2, which popularized this approach.[62] Since that time, other anions, including B, C, N, F and S have all been claimed as improving the visible light photoactivity of TiO_2 and other oxides,[63-67] although controversy regarding the reliability of some of these claims exists.[68] Doping of colloidal oxide particles has also been of great interest for the

production of dilute magnetic semiconductors which display room temperature ferromagnetism and are the potential building blocks for spintronics devices.[69]

The nonaqueous surfactant assisted approaches described above have been shown to be amenable to the doping of nanocrystals. Both cationic and anionic doping can be accomplished, often simply through addition of multiple metal or anionic precursors into the reaction mixture. In quantum dot systems, doping is used to manipulate the bandgap of the material.[70,71] For metal nanocrystals, formation of alloys and intermetallics is common and allows for tunability in the catalytic activity of the materials.[30,72-74] Doping of oxide materials, in contrast, has not been as heavily studied, except in the formation of various ferrite materials for magnetic applications.[41]

Efforts to dope wide bandgap oxides have resulted in the observation of interesting phenomena. In the case of ZnO, Yang, et al. observed that addition of Mg dramatically influenced the growth of the nanoparticles by modifying the crystal structure of the seeds, resulting in the production of uniform rods and tetrapods of $Mg_xZn_{1-x}O$ nanocrystals.[75] Another recent focus has been on the production of nanocrystals of transparent conducting oxides (TCOs). This topic will be discussed in more detail in section 1.3.

Overall, the doping allows for the modification of the electronic, optical, and magnetic properties of nanocrystals, and can be used as a tool to improve

the physical properties of materials or as a means to observe emergent phenomena.[71]

1.2 Photocatalysis

1.2.1 Introduction

Photocatalysis is the process by which photons enable a reaction which would not occur spontaneously. Investigation on this topic began in 1972 when Fujishima and Honda observed the photoinduced splitting of water on a TiO_2 photoanode with Pt cathode to produce hydrogen and oxygen.[76] If useful fuels, such as hydrogen, can be formed efficiently under solar irradiation through photocatalysis, distinct advantages exist over other renewable solar technologies. Unlike photovoltaics which generate electricity, photocatalytic processes can directly create a chemical fuel, eliminating the need for batteries or other methods to store electrical energy. In addition, photocatalysis has been demonstrated to convert CO_2 and other carbon waste materials into fuel products, thus simultaneously capturing carbon and producing an energy source.[77] Photocatalysis should be defined separately from photosynthesis, although confusion exists in the literature. A photosynthetic process is one in which the products have more potential energy than the reactants, as in the case of splitting water to hydrogen and oxygen, while if the products have less potential energy, the process is photocatalytic.

As with typical catalysts, photocatalysts are broadly categorized as either homogeneous or heterogeneous. Homogeneous catalysts reside in the same phase as the reactants, while heterogeneous catalysts are of a different phase. Homogeneous catalysts are typically molecular species soluble in solutions, while heterogeneous catalysts are usually solids catalyzing reaction in liquids or gases. While incredible progress has been made with homogeneous photocatalysts, particularly with respect to compounds which mimic the photosynthetic reaction center of plants,[78] heterogeneous catalysts are advantageous because they are more easily separated and are typically more robust.

Heterogeneous photocatalysts are almost exclusively wide bandgap semiconductors, often of oxide materials which are more resistant to photooxidation. The process of photocatalysis proceeds as follows. First, the semiconductor absorbs a photon with energy larger than the bandgap, producing an electron in the conduction band and a hole in the valence band. Electrons in the conduction band are then available to reduce surface species, while holes are available for oxidations (Figure 2). In order for such surface reactions to occur, recombination of the electron and hole should be prevented, which is normally necessitates high crystallinity and low trap densities.[79] In addition, the band potential levels must be appropriately aligned with the redox potentials of the given reaction. For example, in the case of photosynthetic splitting of water,

not only must the bandgap of the semiconductor be greater than 1.23 eV, but the conduction band potential of the semiconductor must be more negative than 0 V and the valence band potential should be more positive than 1.23 V, as depicted in Figure 2. In practice, the bandgap must be somewhat larger than 1.23 eV to overcome overpotential barriers for electron transfer, with a bandgap of 2 eV considered optimal.

Figure 2. Energy diagram for the photosynthetic water splitting in which an electron and hole form due to photooxidation, the electron reduces protons to hydrogen and oxidizes water to oxygen.

Heterogeneous photocatalysts are studied in two ways, in the form of photoelectrochemical cells or as dispersed catalysts in solution. Both have certain advantages. In photoelectrochemical cells, the reduction and oxidation reactions are spatially separated, eliminating the possibility of the reaction products recombining. Dispersed photocatalysts, on the other hand, are more easily expanded to larger scales. The nanocrystals described in this work will be studied as dispersed catalysts, probing the fundamental properties of the colloids, rather than those of assembled structures.

Several photocatalytic reactions are targets for both energy and environmental applications. For many years, photocatalysts have been utilized for the photooxidation of organic pollutants, such as chlorinated aromatics and other harmful contaminants.[80] For the production of renewable energy sources, water splitting to form hydrogen and oxygen, as described above, is very promising as a potential source of renewable hydrogen. Recently, researchers have focused on enhancing hydrogen evolution rates from aqueous solutions through addition of renewable biomass, a process referred to as photoreforming.[81,82] Early in the investigation of photocatalysts, small organic molecules were found to enhance the rate of hydrogen evolution from water, and were referred to as "hole scavengers" or "sacrificial donors," which increase hydrogen production rates because they are more easily oxidized than water.[83] Recently, researchers showed that the additional hydrogen evolved may result from the oxidation of more complex organic species (see Equation 1).[84,85]

Equation 1 $$C_nH_mO_k + (2n-k)\,H_2O \rightarrow n\,CO_2 + (2n + m/2 - k)H_2$$

Materials such as ethanol, which is a renewable product of fermentation; glycerol, which is a by-product of biodiesel production; glucose, which can be easily extracted from plants; and even wastewater have been proposed or demonstrated as renewable feedstocks to improve hydrogen evolution.[82,86] Furthermore, if oxidation of the biomass can be controlled, oxidation products such as formic acid could be harvested as value-added byproducts.[82]

Photoreduction of CO_2 is another reaction which is favorable because it can directly form liquid fuels, such as methanol or formic acid, which are feedstocks for chemical industry.[87]

Many photocatalysts, including TiO_2, must be loaded with metallic nanoparticles in order to display significant photocatalytic activity for the evolution of hydrogen. These metal particles are referred to as “co-catalysts” and act as electron sinks upon deposition on the semiconductor surface, improving electron hole separation.[80] The surface of the metals also catalyzes the formation of hydrogen, increasing reaction rates.[82] Typical reduction cocatalysts include Pt, Pd, Ni, and Au, with Pt typically resulting in the largest enhancement. Water oxidation catalysts, such as IrO_2, RuO_2, and cobalt phosphate complexes can also be added to improve the other half-reaction.[87-89]

As mentioned above, the materials most promising candidates as photocatalysts are wide bandgap semiconductor oxides. TiO_2 has many of the desired characteristics of an ideal photocatalyst: high stability under irradiation, relatively fast electron transfer kinetics, and appropriate band alignments for many reactions. On the other hand, TiO_2 absorbs less than 5% of the solar spectrum, severely limiting its overall efficiency.[80] While research continues in the discovery of complex multimetallic and alloyed materials with more favorable photocatalytic properties, the remarkable properties of TiO_2 continue to fuel intense interest.[90]

1.2.2 Measurement Techniques

Experimental techniques for measuring the photocatalytic activities of powders are not satisfactorily standardized. Many experimental factors influence the results of photocatalytic reactions, including reactor geometry, light source, optical components, catalyst dispersibility, catalyst concentration, phase of reactants, etc. For this reason, it is often difficult to establish proper comparisons between materials in the literature, although the use of standards such as P25 allows for comparisons to be made. For solution reactions, reactor geometries include annular reactors, in which a mercury lamp is inserted inside of a jacketed glass or quartz reactor with an additional cooling jacket, and directional reactors in which light is incident on a glass, sapphire, or quartz window behind which a solution resides.

The products of photocatalytic reactions can be identified using many methods depending on the reaction type. For liquid phase products, high performance liquid chromatography (HPLC) and gas chromatography mass spectrometry (GC-MS) are useful tools, although typically require manual injection. For hydrogen evolution reactions, because the major product is gaseous, a flow reactor connected to an on-line gas chromatograph or mass spectrometer is convenient approach as it can be easily automated to monitor reaction rates continuously. An example of such a reactor, which was utilized to measure the activity of nanocrystals in this thesis, is diagrammed in Figure 3.

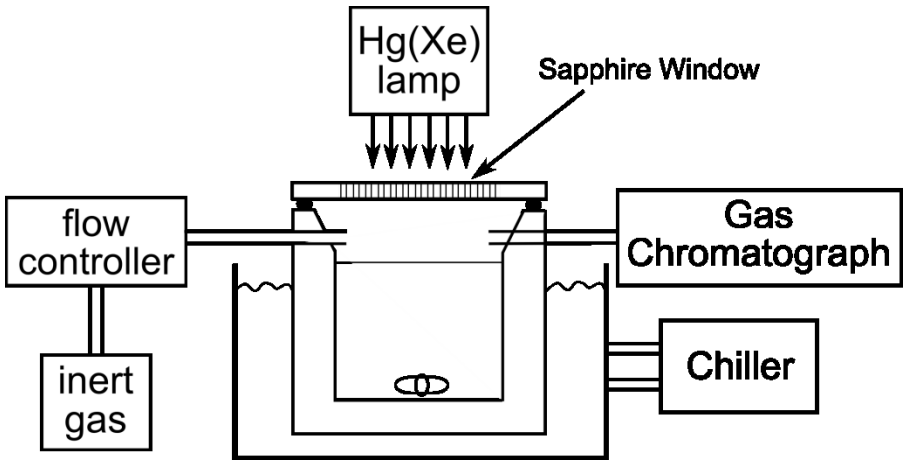

Figure 3. Photocatalytic gas reactor with online gas chromatography.

1.2.3 Surface Structure

The surface structure of a photocatalyst is a very important factor controlling the reactivity of the material. This fact has been established through careful study of single crystalline surfaces using ultra high vacuum techniques.[87,91] On the other hand, realizing the effects of surface structure in actual catalysts is difficult due to the relatively poor uniformity of the materials. This issue is collectively referred to as the “pressure gap” of catalysis, because materials performing catalysis under industrial conditions are difficult to compare to the pristine surfaces studied under high vacuum. Nanocrystals with controlled morphology may act as model systems to fill the pressure gap, as comparisons can only be made if very uniform particles with control over faceting can be produced synthetically. In this vein lies the future of catalysis engineering.

Significant work has been devoted to describing the effect of faceting and particle shape on the catalytic activity and selectivity of metal particles to correlate with studies of single crystals.[74,92-96] This work has been enabled by the evolution of new synthetic methods which enable the production of metal particles with tunable shape. Similar studies have not been undertaken to determine the influence of oxide particle shape on photocatalytic reactions, due to the modest synthetic control described, but represents an opportunity to improve photocatalytic activities and selectivities and understand more about the influence of surface structure on reaction mechanisms.

1.3 Transparent Conducting Oxide Nanocrystals

1.3.1 Introduction and Materials

Transparent electrodes are important class of materials for energy applications and consumer electronics. For photovoltaics, one of the electrodes must be highly conducting while also highly transparent so that light can enter to illuminate the absorbing material. In displays and touch screens, the transparent electrode allows for light to be transmitted out of the device. Among the transparent electrodes, transparent conductive oxides (TCOs) are the most heavily utilized materials for these applications, due to their robustness. The dominant TCO materials which have been mass produced are based on heavy impurity doping of oxides such as tin oxide (SnO_2), indium oxide (In_2O_3), and zinc oxide (ZnO). Particular examples include indium tin oxide (ITO In_2O_3:Sn), fluorine doped tin oxide (FTO, SnO_2:F), and aluminum doped zinc oxide (AZO, ZnO:Al). Addition of cations with additional electrons relative to the host cation or fluorine contributes electrons to the conduction band of the material, doping the material n-type. P-type conductive oxides have been described, but are difficult to prepare, due to the tendency of oxides to form oxygen vacancies, which contribute to n-type conductivity.[97]

The TCOs currently mass produced have been satisfactory for many applications, but the search for new materials continues. One set of materials which was found early on to be an excellent TCO candidate is CdO-based

oxides.[98] In fact, Cd_2SnO_4 TCOs are among the highest performing, but concerns about toxicity have discouraged thorough investigation.[99] For certain applications, such as CdTe based solar cells and non-consumer electronics, Cd-based TCOs may be an option if the device performance warrants use.[100-102]

TCO films have been prepared using many methods including magnetron sputtering, chemical vapor deposition, pulsed laser deposition, and spray pyrolysis.[103] Among solution-phase methods, sol-gel based approaches have been developed for the preparation of TCO films or TCO nanocrystals, although annealing is required to fully crystallize the materials.[104-106] Niederberger, et al. reported the first synthesis of ITO nanocrystals using nonhydrolytic sol-gel methods, which resulted in dispersible materials which high crystallinity at mild termperatures. Since that time, several groups have reported the nonaqueous synthesis of TCO particles, including ITO,[107-109] antimony doped tin oxide (SnO_2:Sb),[110] AZO,[111] and indium doped zinc oxide (ZnO:In).[112] These materials may be used as precursors to form conductive films or potentially for the preparation of novel optical devices based on metamaterials, as will be described in more detail.

1.3.2 Transparent Conducting Oxide Films

The production of transparent electrodes has been the primary focus for the preparation of TCO nanocrystals.[113] TCO nanocrystal solutions are advantageous because they can be spin casted or printed from solution onto a

variety of substrates, including flexible plastics, to form conductive films under some conditions.[113,114] This is in contrast to the typical methods, such as sputtering or spray pyrolysis, which are not compatible with plastic substrates.[104,113,114] The key to this research is to produce highly conductive, transparent films under the mildest conditions possible to allow for the widest range of substrates. This necessitates the creation of conductive pathways between TCO particles after the film formation, which becomes particularly difficult if the nanocrystals are capped with insulating ligands.[114]

1.3.3 Plasmonic Oxide Nanocrystals

In addition to being potential precursors for transparent electrodes, TCO nanocrystals have been recently identified to support tunable localized surface plasmon resonances (LSPRs) in the near infrared (NIR) spectral range.[108] LSPRs are well-known in noble metal nanoparticles, such as gold and silver, and result when free electrons collectively oscillate in a material at certain frequencies. The wavelength of the resonance is dependent on the optical properties of the material, namely the dielectric function. The dielectric function of materials with high free electron concentrations, including TCO materials and other materials, can typically be fitted in part using the Drude model, the equation of which is:

Equation 2

$$\varepsilon(\omega) = 1 - \frac{{\omega_p}^2}{\omega^2 - i\gamma\omega}$$

, where ω is the photon energy, ω_p is the plasma frequency, and γ is the damping constant.[115] ω_p is an important constant for any metal, and physically is the frequency below which photons cause electrons to collectively oscillate. This oscillation results in high reflectivity, and can be thought of as the frequency at which the material "becomes metallic" in the optical sense. In terms of the dielectric function, the real part of permittivity ε_1 becomes negative below the plasma frequency (see Figure 4). For typical metals, the plasma frequency lies in at UV or visible frequencies, while for TCOs, the plasma frequency is in the NIR and is tunable depending on the free electron concentration. In the absence of other absorptions, a plasma frequency in the NIR results in high transparency in the visible range, which is desirable for transparent electrodes

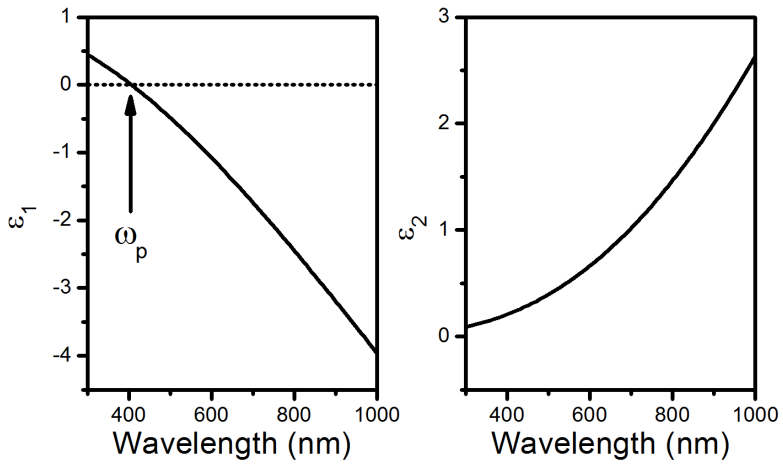

Figure 4. Plotted real (ε_1) and imaginary (ε_2) parts of permittivity for the Drude model of metals.

The extinction coefficient for a particle composed of a Drude material can be calculated using Mie's theory.[115] For particles much smaller than the

wavelength of light (< λ/20), only the dipolar coupling is significant, and the extinction coefficient for N particles of volume V is calculated to be:

Equation 3
$$\kappa = \frac{18\pi NV{\varepsilon_m}^{1/2}}{\lambda}\frac{\varepsilon_2}{[\varepsilon_1 + 2\varepsilon_m]^2 + {\varepsilon_2}^2}$$

, where λ is the wavelength of the light, and ε_m is the dielectric constant of the medium.[115] From this equation, it becomes apparent that a resonance will occur when $\varepsilon_1(\omega) = -2\varepsilon_m$ as long as $\varepsilon_2(\omega)$ is weakly dependent on ω.[115] Thus, the LSPR frequency is directly determined by the dielectric function of the material, but correlates with the value of ω_p. By tuning the free electron concentration through adjustment of doping concentration, the ω_p and the LSPR frequency can be carefully tuned throughout the NIR.

LSPRs have been reported for TCO nanocrystals of ITO,[108] AZO,[111] and tungsten oxide ($WO_{2.83}$).[116] In addition, copper chalcogenide nanocrystals, particularly $Cu_{2-x}S$ and $Cu_{2-x}Se$, have also been discovered to support LSPR, resulting from heavy p-type doping through cationic vacancies. These materials are particularly interesting when the particle size is very small, as quantum confinement is expected, creating the possibility of observing interactions between confined excitons and the oscillating electrons. On the other hand, the copper chalcogenides are quite susceptible to oxidation, resulting in optical changes upon air exposure.

1.3.4 Metamaterials

Metamaterials are artificial materials which posses properties that depend on the organizational structure of their components, rather than only on the intrinsic properties of the building blocks.[117] Through careful design, materials can be produced that exhibit unnatural optical properties, such as negative index of refraction, which could enable cloaking devices and superlensing at optical frequencies. As a proof of theoretical predictions, early optical metamaterials were produced at macroscopic length scales which exhibited such properties as negative refractive index at microwave frequencies.[118] More recent research moves toward the preparation of metamaterials at visible and NIR frequencies, with some promising demonstrations already described in the literature.[119,120]

Metallic films and particles, including TCOs, have been proposed and proven as useful building blocks for designs of metamaterials at optical frequencies.[121,122] In the case of negative refractive index, for a material to display this phenomenon it must simultaneously have negative permittivity and permeability.[123] As described in section 1.3.3, metallic materials have negative permittivity at energies below their plasma frequency. By organizing plasmonic particles into the proper ordered structures, such as split-ring resonators or nano-fishnets, it may be possible to induce negative permeability, also referred to as artificial magnetism, at optical frequencies. Together, this could potentially result in the formation of materials with negative refractive index at visible or near-infrared frequencies.

1.4 Materials Characterization Techniques

1.4.1 Electron Microscopy

Electron microscopy is an incredibly important tool for the investigation of nanomaterials. The real-space imaging of sub-optical wavelength objects has led to advances in the fields of catalysis, as well as cell biology, allowing for visualization of both catalytic reaction centers and cellular interactions.[124,125] Even more, the interactions of electrons with atoms results in the release of characteristic X-rays and electrons which are utilized for elemental analysis. With the advent of aberration corrected imaging, the quality of information gained regarding the structural and elemental composition of a material is ever increasing, and the introduction of environmental conditions allows for imaging to be performed under more relevant operating conditions.[124]

Transmission electron microscopy (TEM) has been a workhorse for much of the work conducted in this thesis. In this instrument, a beam of electrons is focused onto a sample, and the electrons which pass through the sample are imaged. The de Broglie wavelength of an electron can be calculated based on the accelerating voltage of the microscope, and lies in the range of 1-10 pm (0.001-0.01 nm), allowing for interatomic spacings to be easily probed and imaged.[126] There is no other method to reliably and quickly determine the morphology and phase of a sample, or to gain deep insight into the atomic structure of individual building blocks. While the majority of the data is taken in

bright-field mode, electron diffraction is also utilized to probe a material's phase (at low camera length) or to characterize self-assembled structures (at high camera length). Scanning electron microscopy (SEM) is also a valuable tool for morphological screening and microanalysis. While is it difficult to visualize depth in TEM, SEM is ideal to characterize textured materials and can also be combined with elemental analysis.

1.4.2 X-ray Scattering and Simulation

X-ray scattering (or diffraction) is a commonly utilized tool to investigate crystalline materials. The advantage of X-ray scattering is that it represents a bulk measurement of a nanocrystalline material. Because only a small portion of any sample is probed at one time, electron microscopy is plagued by "selective imaging," where uniform portions of a grid are made to represent an entire sample. X-ray scattering is not susceptible to such selectivity. In addition, X-ray scattering can probe multiple length scales depending on angle, with wide-angle x-ray scattering (WAXS) probing interatomic spacings and small-angle x-ray scattering (SAXS) investigating interparticle spacings. SAXS is very commonly used for the investigation of biomolecules and polymers.[127,128]

WAXS, as it is commonly utilized in the form of powder x-ray diffraction, probes the crystalline structure of materials, but can also be used to investigate particle shape. In small nanocrystals (< 30 nm), broadening of the peaks that exceeds instrumental broadening occurs as a result of finite size effects.[27] In

addition, anisotropic particle shapes will result in variations in the strength of reflections in a predictable way. SAXS is very sensitive to changes in particle size, as well as the particle size distribution.[27] Together they provide a total picture of particle morphology and uniformity.

The Debye equation describes the intensity of X-ray scattering from an isotropic collection of particles with known atomic structure. The q-dependent powder X-ray diffraction intensity, I(q) may be calculated as described previously[27]:

Equation 4 $$I(q) = I_0 \sum_m \sum_n F_m F_n \frac{\sin(q r_{mn})}{q r_{mn}},$$

where I_0 is the incident intensity, $q = 4\pi \sin\theta / \lambda$ is the scattering parameter for X-rays of wavelength λ diffracted through the angle θ, r_{mn} is the distance between atoms m and n, with atomic form factors F_m and F_n, respectively. Atomic form factors are calculated from tabulated Cromer-mann coefficients, as shown below (see Appendix A for tabulated values).[129] To improve calculation time, the Debye equation can be discretized by binning identical distances to give the following equation[130]:

Equation 5 $$I(q) = \frac{I_0}{q} \sum_m \sum_n F_m F_n \frac{\rho(r_{mn})}{r_{mn}} \sin(q r_{mn}),$$

where $\rho(r_{mn})$ is the multiplicity of each unique distance (r_{mn}) in the structure. Thermal vibrations are known to distort the XRD pattern (more strongly at higher angles) due to uncertainty in the atomic positions. This may be simulated

through multiplication of the atomic form factors by a temperature factor, which has the Debye-Waller factor as the input[130]:

Equation 6

$$F_m(\theta) = \exp\left(-\frac{B_j \sin^2(\theta)}{\lambda^2}\right)\left(\sum_{i=1}^{4} a_i \exp\left(-\frac{b_i \sin^2(\theta)}{\lambda^2}\right) + c\right),$$

where B_j is the Debye-Waller factor, and a_i, b_i and c_i are the Cromer-Mann coefficients. A size distribution may be incorporated into the simulation using a Gaussian weighted sum of many nanocrystal simulations.

Two scripts written in perl and C++ have been prepared to calculate the X-ray scattering patterns at arbitrary angle using the Debye equation, as outlined above. This code and information regarding its implementation are available in Appendix A.

2. TITANIUM DIOXIDE NANOCRYSTALS

2.1 Introduction

Titanium dioxide (TiO_2) is an industrially important wide-band gap semiconductor, with an annual production of greater than one million metric tons each year in the United States alone.[131] In addition to the traditional applications of TiO_2 in the fields of coatings, ceramics, and cosmetics, nanostructuring of TiO_2 has enabled its use as an active material in sensors, electrochromics, gas-phase catalysts, fuel cells, lithium-ion batteries, photovoltaics, photoelectrochemical cells, and photocatalysts.[132,133] TiO_2 has several advantages over other inorganic materials, including earth abundance, low toxicity, chemical and thermal stability and resistance to photocorrosion.[132-134] Three polymorphs of TiO_2 exist naturally: rutile, anatase, and brookite (Figure 5).[135] While rutile is the most thermodynamically stable bulk phase, anatase has been shown by numerous studies to be more photocatalytically active than rutile and is often dominant in nanocrystalline TiO_2, due to having lower surface energy than rutile.[87,132,135] Brookite is a low-temperature stable phase and is usually obtained as a mixture with the other polymorphs of TiO_2, and little is known regarding its photocatalytic activity.[136] High surface area TiO_2 nanomaterials have been synthesized for many years through a variety of techniques, including gas phase, sol-gel, hydrothermal, and chemical vapor deposition (CVD) methods and have immense promise in future nanoengineered materials.[132]

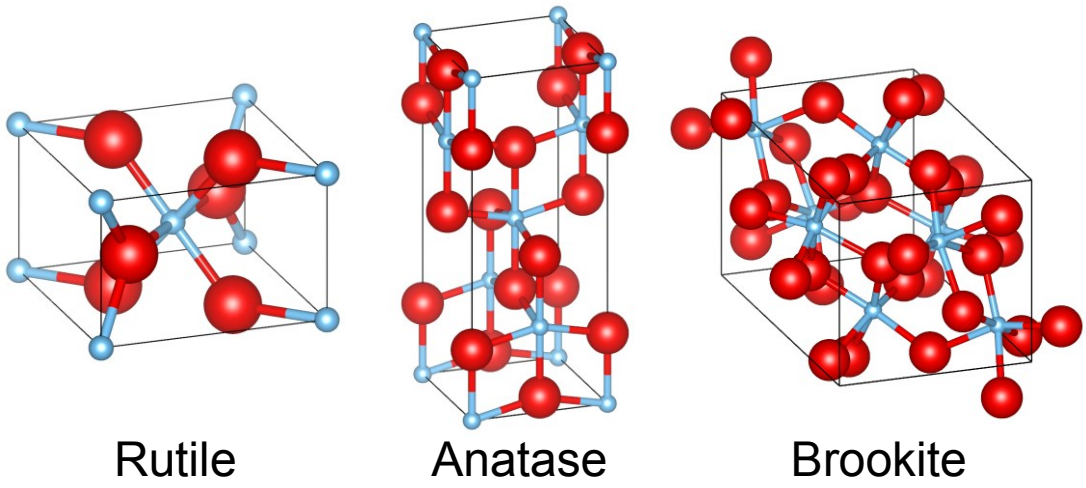

Figure 5: Unit cells of the three polymorphs of TiO_2, rutile, anatase, and brookite.

As described in section 1.1.3, nonaqueous surfactant assisted synthetic methods have revolutionized the production of highly monodisperse and shape-controlled nanocrystals (NCs) composed of a variety of materials, including catalytically relevant metals and metal oxides.[11,26,27,45,137] Through optimization of the synthetic parameters, these techniques provide the most precise and reproducible control over particle size and morphology, enabling the production of model systems for catalysis with near atomic precision in size and control over faceting.[74,92,94-96,138-140] NCs produced through these methods are typically phase pure single crystals, and may be activated through ligand exchange or mild oxidative treatment, requiring no high temperature annealing.[47,74,141,142] In addition, because the NCs are surfactant stabilized, they are highly soluble in nonaqueous solvents. This enables numerous preparation techniques which are not typically available for the production of traditional catalysts, including the

formation of thin films through spin-coating,[143] liquid interfacial assembly,[96] and self-assembly.[138] TiO_2 NCs of rutile, anatase, and brookite phases with various morphologies have been synthesized using these techniques, but the photocatalytic activity of these materials has not been exhaustively explored.[31,40,47,141,144-150] Overall, this nonaqueous approach provides unparalleled ability to tune the shape and size of monodisperse catalytic NCs to precisely tune the surface area and exposed facets in NCs, which enables the derivation of structure-activity relationships. While the coupling of synthetic control of faceting with catalytic activity has been achieved for metallic NCs, very few studies have investigated the influence of faceting on the photocatalytic activity of NCs. In this chapter, techniques will be described which enable control over the size, shape, and phase of TiO_2, allowing for the morphological dependence of photocatalytic activity to be explored in more detail than previously possible.

2.2 Using TiF_4 to Engineer Morphology and Photocatalytic Activity[I]

2.2.1 Introduction

Numerous recent publications have focused on synthetically controlling the facets exposed in the anatase phase of TiO_2.[151-153] Studies of single crystalline surfaces have shown that the particular facets exposed during photocatalytic reactions dramatically influence both reaction rate and selectivity.[87,91,135,154] The most stable form of the anatase polymorph is a tetragonal bipyramidal structure in which primarily {101} facets of anatase are exposed, with a small percentage of {001} facets, as predicted by the Wulff construction.[155] Yang, et al. recently demonstrated that the introduction of hydrofluoric acid (HF) during the hydrothermal synthesis of TiO_2 stabilizes the {001} facet relative to the {101} facet, allowing for the formation of truncated bipyramidal structures, in the micron-size range.[151] The authors also suggest, based on theoretical calculations, that the {001} facet has higher reactivity compared to the {101} facet due to having a higher concentration of low coordination Ti_{5c} centers. This has subsequently created a surge of interest regarding the relative reactivity of the various facets of anatase TiO_2, both theoretically[156,157] and experimentally.[158-164] Currently, reports are mixed

---

[I] A large percentage of this section appears in print as Gordon, T. R.; Cargnello, M.; Paik, T.; Mangolini, F.; Weber, R. T.; Fornasiero, P.; Murray, C. B. *J. Am. Chem. Soc.* **2012**, *134*, 6751–6761. Copyright, 2012, American Chemical Society.

regarding the relative reactivity of the two facets under illumination, possibly due to the multitude of reaction conditions investigated.[158,163,165,166] Moreover, the relative activity of the {001} and {101} facets has primarily been determined for large anatase crystallites (~0.2 – 5 μm in size), with very few examples reporting the photocatalytic activity of high-surface area, nano-sized catalysts which are more relevant for practical applications. Obtaining uniformity in both the morphology and phase composition of TiO_2 at the nanoscale is non-trivial using traditional synthetic methods and preferential exposure of the {001} facet of anatase often necessitates the use of concentrated HF, which is hazardous to handle.[167]

In this section, we report the controlled synthesis of highly uniform TiO_2 NCs in the 10-100 nm size regime which are prepared through a seeded growth technique.[51,147,168] The titanium precursor titanium (IV) fluoride (TiF_4) releases HF *in situ*, which acts as a structure directing agent and allows for better morphological control than previously obtained in hydrothermal syntheses which require the direct handling of HF. We show that the percentage of {001} and {101} facets in the tetragonal bipyramidal anatase TiO_2 NCs can be engineered through choice of the titanium precursor and co-surfactant. X-ray diffraction studies, in conjunction with simulation, allow for the determination of the average NC dimension in a given sample which correlates with results obtained through electron microscopy. In addition to enabling shape control, TiF_4 is observed to

alter the optical properties of the NCs. UV-Vis-NIR-IR optical spectroscopy, low temperature electron paramagnetic resonance (EPR) spectroscopy, and X-ray photoelectron spectroscopy (XPS) suggest that TiO_2 NCs produced in the presence of TiF_4 are oxygen deficient and that the NC surfaces are partially fluorinated. The photocatalytic activity of the platinized TiO_2 NCs is tested for the evolution of hydrogen in the presence of methanol as model sacrificial agent. Within the series of anatase NCs, those with more {101} facets exposed are observed to have the highest activity, which is consistent with recent experimental reports.

2.2.2 Experimental

Chemicals.

The following chemicals are used as received without further purification. Titanium (IV) fluoride (TiF_4, 99%), titanium (IV) chloride ($TiCl_4$, 99%), nitrosonium tetrafluoroborate ($NOBF_4$), 1-octadecene (90%) (1-ODE), 1-octadecanol (1-ODOL, 97%), N,N-dimethylformamide (DMF), toluene, hexanes, acetone, methanol and 2-propanol are purchased from Acros Organics. Oleylamine (OLAM, 70%), oleic acid (OLAC, 90%), acetonitrile (ACN) and potassium tetrachloroplatinate(II) (K_2PtCl_4, ≥99,9%) are purchased from Sigma Aldrich.

Preparation of Stock Solutions.

Stock solutions are prepared in a glovebox under N_2 atmosphere. TiF_4 stock solution consists of 0.2 M TiF_4 and 1.0 M OLAC in 1-ODE. $TiCl_4$ stock

solution consists of 0.2 M $TiCl_4$ and 1.0 M OLAC in 1-ODE. The TiF_4 stock solution is stirred on a hotplate set to 80 °C to promote the dissolution of TiF_4. Once dissolved, the TiF_4 stock solution is orange-brown and the $TiCl_4$ stock solution is dark brown.

Synthesis of TiO_2 NCs.

All syntheses are performed using standard Schlenk line techniques under nitrogen atmosphere. A general procedure proceeds as follows. In a 125 mL flask, 30 mmol of co-surfactant (OLAM or 1-ODOL), 10.2 mL of 1-ODE and 0.48 mL (1.5 mmol) of OLAC are combined and degassed at 120 °C for 1 hour. For 1:1 mixtures, TiF_4 and $TiCl_4$ stock solutions are mixed at equal volume in the glovebox. After degassing the flask, 1.5 mL of the desired stock solution (or mixed stock solution) is added at 60 °C. Then, the solution is quickly heated to 290 °C and held 10 min to allow for the formation of seed crystals. 8 mL of the mixed stock solution are then pumped into the flask kept at 290 °C at 0.3 mL min^{-1} using a New Era Pump Systems NE-1000 syringe pump. Afterwards, the heating mantle is removed and the flask left to cool naturally to ambient temperature. For simplicity, TiO_2 NC samples will be referred to as X–co-surfactant, where X refers to the stock solution used, i.e. F (for TiF_4), Cl (for $TiCl_4$) or M (for 1:1 mixture). Therefore, a sample synthesized with TiF_4 and 1-ODOL will be referred to as F-ODOL.

Synthesis of $TiOF_2$ Nanocubes.

A 50 mL flask is evacuated under heating to remove atmospheric gases. Then, under N_2, 10 mL of stock A are injected into the flask and the solution is further degassed at 120°C for 15 min. The reaction is subsequently heated to 200°C, held for 30 min and cooled to room temperature.

Workup.

Post-synthesis, the reaction contents are first diluted with a small volume of toluene and centrifuged at 6000 rpm to separate the NCs. The NCs are then redispersed through addition of toluene and 100 µL of OLAM with sonication. Insoluble surfactant and agglomerated particles are removed through centrifugation. A mixture of 2-propanol and methanol are added to precipitate the NCs, and centrifugation at 6000 rpm is used to recover the NCs. This washing process was repeated twice. NCs with dimensions less than 30nm are subsequently highly soluble in nonpolar or low-polarity solvents including hexanes, toluene, carbon tetrachloride, tetrachloroethylene, and chloroform. Larger particles are sparingly soluble, forming stable suspensions in the same solvents.

Ligand Exchange with $NOBF_4$.

In a centrifuge tube, 0.1 g of $NOBF_4$ and 10 mL of ACN are combined and sonicated, resulting in the formation of a yellow solution indicating the solublization of $NOBF_4$. 10 mL of the $NOBF_4$ saturated ACN is added to the hexanes solution (10 mL) of NCs (50-150 mg). The NCs quickly become

insoluble and are collected through centrifugation. The solid is then completely solubilized in DMF with sonication. To remove residual organics, DMF solutions are washed through the addition of a mixture of toluene and hexanes until precipitation occurs, followed by centrifugation. This process is repeated three times. After the final centrifugation, the NCs are dried in a vacuum oven at 60 °C overnight to remove residual solvent molecules. Once dry, each sample is ground in an agate mortar and pestle into a fine powder with grain dimensions below 150 μm.

NaOH treatment of TiO_2 NCs.

Removal of fluorine is performed by treating the samples with a NaOH solution according to the work of Minella, et al.[169] Briefly, ~50 mg of the powder are dispersed in 5 mL of NaOH aqueous solution at pH 12 (~0.01 M) and stirred in the dark for 8 h. The powder is recovered by filtration (Millipore 0.45 μm), washed with 1 mM HCl and twice distilled water, and finally dried at 50 °C for 8 h.

Photocatalytic Activity.

The photocatalytic activity of the ligand-exchanged and NaOH-treated NCs is evaluated for hydrogen production using methanol as model sacrificial agent. ~27 mg of the NCs are suspended with sonication in 80 mL of an aqueous solution of methanol (1:1 by volume, final concentration of NCs ca. 0.3 M). K_2PtCl_4 is added to obtain a final loading of platinum of 1 wt. %. The suspension is irradiated using a Solar Simulator (LOT-Oriel) (see Figure 6 for lamp spectrum)

equipped with a 150 W Xe lamp filtered with an atmospheric filter to reduce the fraction of UV photons. An Ar flow (15 mL min^{-1}) ensures the complete removal of air from the reactor and that the reaction products reach the detector. A recirculation bath is used to keep the temperature of the reactor constant at 20 °C.

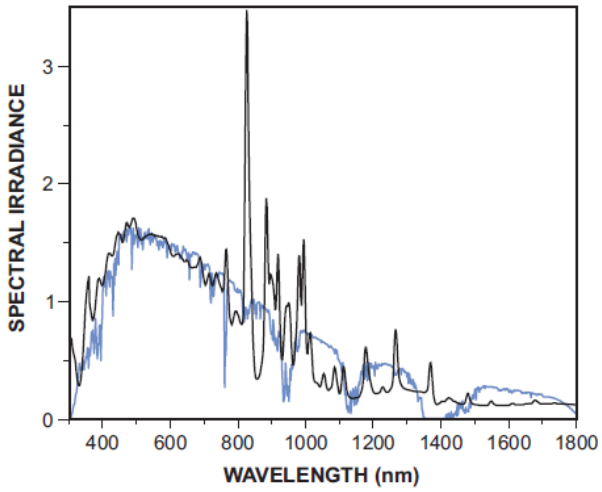

Figure 6: Typical spectral output (black) of a solar simulator (there is negligible output from 250-300 nm) and standard AM1.5G spectrum(blue).

Gaseous products are analyzed by gas chromatography (GC) using a thermal conductivity detector (TCD) for the quantification of H_2 and CO_2 with He as carrier. The liquid phase by-products are analyzed by gas chromatography/mass spectrometry (GC/MS) using a HP 7890 GC equipped with a DB-225ms column (J&W) and a HP 5975C mass spectrometer.

Characterization.

Transmission electron microscopy (TEM) images were recorded using a JEOL JEM1400 TEM equipped with a SC1000 ORIUS CCD camera operating at 120 kV. High-resolution TEM (HRTEM) images were recorded on a JEOL 2010F operating at 200kV. Samples were prepared by drop-casting a dispersion of NCs in toluene or hexanes on a 300 mesh carbon-coated copper TEM grid followed by drying at 50 °C under vacuum. Scanning electron microscopy (SEM) images and energy dispersive X-ray spectroscopy (EDS) spectra were recorded on a JEOL JSM7500F equipped with an Oxford X-stream EDS detector. Samples were prepared on 150 mesh carbon-coated copper TEM grids as described above. All X-ray diffraction (XRD) patterns were recorded on a Rigaku Smartlab diffractometer equipped with a Cu K_α source. For transmission measurements (2θ scan), NCs were placed as highly concentrated toluene solutions into 1.0 mm glass capillaries. For reflection measurements (θ – 2θ scan), NCs were dropcast from concentrated hexanes solutions onto glass slides. UV-Vis-NIR spectra were recorded on a Varian Cary 5000 spectrometer, equipped with a Harrick praying mantis DRS accessory for diffuse reflectance spectra (DRS). For DRS, powdered samples were diluted at 2 wt. % in KBr and pure KBr was used as a background. IR spectra were recorded on a Thermo-Fisher Continuμm FT-IR system in transmission mode using a Harrick demountable liquid cell. EPR spectra were collected for powder samples on a Bruker Elexys E500 spectrometer at frequency 9.391 GHz at the Bruker Biospin Corporation. Samples for XPS

analysis were dropcast from 1:10 solutions of octane:hexanes onto Si wafers and then treated in Ar plasma for 4 minutes using a Gatan Solarus Model 950 plasma cleaner to remove the bound surfactants. N_2 physisorption experiments were carried out on a Micromeritics ASAP 2020C. The samples were first degassed in vacuum at 120 °C for 19 h prior to N_2 adsorption at liquid nitrogen temperature.

XPS Analysis.[II]

XPS analyses were carried out with a customized X-ray photoelectron spectrometer, which has extensively been described previously.[170] Briefly, the XP-spectrometer is equipped with a monochromatic Al Ka source. The electrons emitted from the specimen are collected with an electrostatic lens, whose axis is normal to the sample surface. The acceptance angle of the input lens system is 14°. After passing the hemispherical analyzer, the photoelectrons are detected by a two-dimensional MCP/CCD detector.

In the present work, the X-ray source was run at 30 mA and 12 kV, while the analyzer was operated in constant-analyzer-energy (CAE) mode. Survey spectra were acquired with pass energy and step size equal to 200 eV and 0.3 eV, respectively. In the case of high-resolution (HR) spectra, the pass energy and step size were, respectively, 100 and 0.1 eV (full width at half-maximum (FWHM) of the peak height for the Ag $3d_{5/2}$ = 0.64 eV). The dimension of the slit at the entrance of the hemispherical analyzer was 3.0 mm (straight) for survey

[II] This section courtesy of Dr. Filippo Mangolini, who was responsible for measurement and analysis of XPS data.

spectra and 1.3 mm (straight) for high-resolution spectra. The residual pressure in the analysis chamber was always below 5 x 10^{-6} Pa. The spectrometer was calibrated using a standard silver foil with an accuracy better than ±0.1 eV. The high-resolution spectra were processed using CasaXPS software (v2.3.16, Casa Software Ltd., Wilmslow, Cheshire, U.K.). An iterated Shirley-Sherwood background subtraction was applied before peak fitting using a linear least-squares algorithm. Minor charging was observed (below 0.6 eV) and corrected by referencing to aliphatic carbon at 285.0 eV. Curve synthesis was carried out using model Gauss/Lorentz product functions. The quantitative evaluation of XPS data was performed on the basis of the integrated intensity (i.e., the peak area in Cps x eV obtained from the original spectra after background subtraction and curve synthesis) using a first-principles model and applying the equations of Powell.[171] The apparent atomic concentration was calculated as:

Equation 7:
$$X_j = \frac{I_{ij} / S_{ij}}{\sum_j I_{ij} / S_{ij}}$$

where I_{ij} and S_{ij} are the area and the sensitivity factor of the peak *i* of the element *j*, respectively. The sensitivity factors were calculated from the Scofield photoionization cross-section,[172] the angular asymmetry factor[173] and the inelastic mean free path (*IMFP*) corrected for the emission angle, assuming the sample to be homogeneous. The inelastic mean free path, i.e. the mean distance

travelled by electrons with a given kinetic energy (*KE*) between inelastic collisions in a material *M*, was calculated using the TPP-2M formula.[174]

X-ray Scattering Simulation.

X-ray scattering simulations are performed as described in section 1.4.2. Particle size distribution is incorporated using a probability distribution, where each final pattern is the Gaussian weighted sum of 21 or more patterns from individual NCs.

2.2.3 Results and Discussion

Seeded Growth Synthesis of TiO_2 Nanocrystals

The synthesis of TiO_2 NCs is based on a seeded growth approach.[147] Small TiO_2 nanocrystallites (or "seeds") are first formed by combining a small quantity of titanium (IV) halide (TiX_4) dissolved in oleic acid (OLAC) with a large molar excess of the co-surfactant (oleylamine (OLAM) or 1-octadecanol (1-ODOL)) in solvent 1-octadecene (1-ODE) and quickly heating to 290 °C. After a 10 min induction period in which anatase TiO_2 seeds form (Figure 7), a stock solution of TiX_4 dissolved in OLAC/1-ODE is slowly added to the seed solution via syringe pump, enabling the progressive growth of the nanocrystalline seeds and preventing further nucleation.[51,147,168] The addition of co-surfactant OLAM or 1-ODOL is essential, as these molecules accelerate the formation of TiO_2 under nonaqueous conditions, as discussed in more detail below.

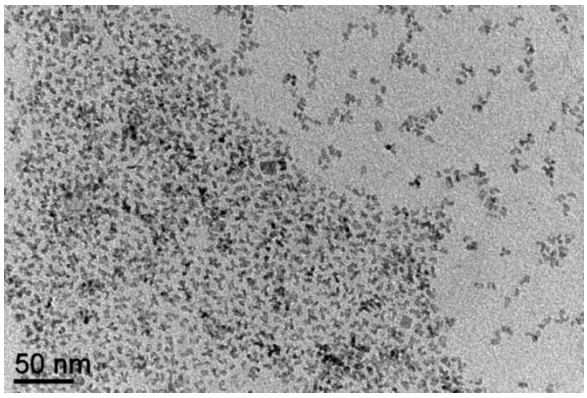

Figure 7: Representative TEM image of anatase TiO_2 seeds formed at 290°C before addition of stock solution.

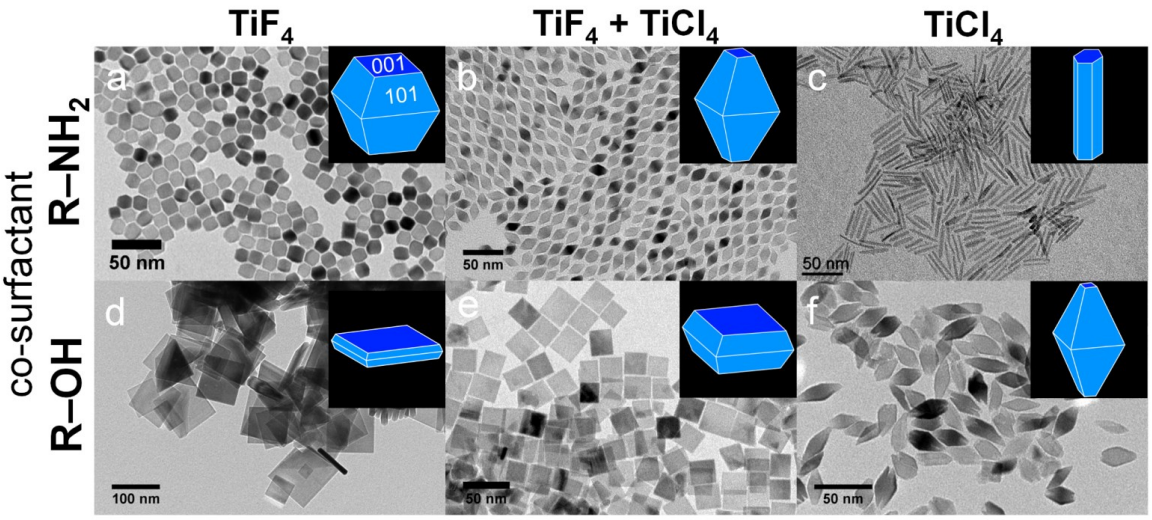

Figure 8. TEM images of TiO_2 nanocrystals synthesized using the precursor TiF_4 (a,d) a mixed precursor of TiF_4 and $TiCl_4$ (b,e) and $TiCl_4$ (c,f). Those depicted in a – c and d – f are synthesized in the presence of OLAM and 1-ODOL, respectively.

Transmission electron microscopy (TEM) images (Figure 8) show the range of morphologies achievable through the present approach, depending on the choice of co-surfactant and titanium (IV) halide (TiX_4) under otherwise

identical reaction conditions. We observe dramatic differences in the morphology of the obtained NCs when using TiF_4 as the titanium precursor compared to using $TiCl_4$. In the presence of co-surfactant OLAM, TiF_4 produces highly uniform tetragonal bipyramidal anatase NCs (sample F-OLAM) which are significantly truncated perpendicular to the [001] direction (Figure 8a). In the case of $TiCl_4$, pure phase brookite nanorods (Cl-OLAM), similar to as reported previously, are produced (Figure 8c).[147] With co-surfactant 1-ODOL, TiF_4 results in anatase nanoplates (F-ODOL) with a high percentage of {001} facets (Figure 8d), while $TiCl_4$ produces tetragonal bipyramidal anatase NCs (Cl-ODOL) with primarily {101} facets (Figure 8f). The NCs are single crystalline as confirmed by HRTEM (Figure 9), and the size is observed to increase with time as more stock solution is added (Figure 10). In accordance with recent syntheses performed under aqueous conditions, we observe that the use of fluorine containing species results in the preferential exposure of the {001} facet of anatase, truncating the bipyramidal base morphology of the NCs.[151,153]

The percentage of {001} and {101} facets in the TiO_2 NCs is further controlled through use of a mixed precursor solution consisting of equimolar TiF_4 and $TiCl_4$ as the precursor for the seeded growth of TiO_2 NCs. Using co-surfactant OLAM, highly monodisperse anatase tetragonal bipyramidal NCs are formed with the mixed precursor (M-OLAM), which have a small percentage of {001} facets. The mixed precursor in combination with 1-ODOL forms nanoplates

(M-ODOL) with large percentages of {001} facets, although not as high a percentage as observed with pure TiF_4 precursor and the particle size is much reduced. Thus, the present synthetic technique provides a means to tune both the size and truncation of anatase tetragonal bipyramidal NCs by modifying the surfactants and precursors in nonaqueous solution.

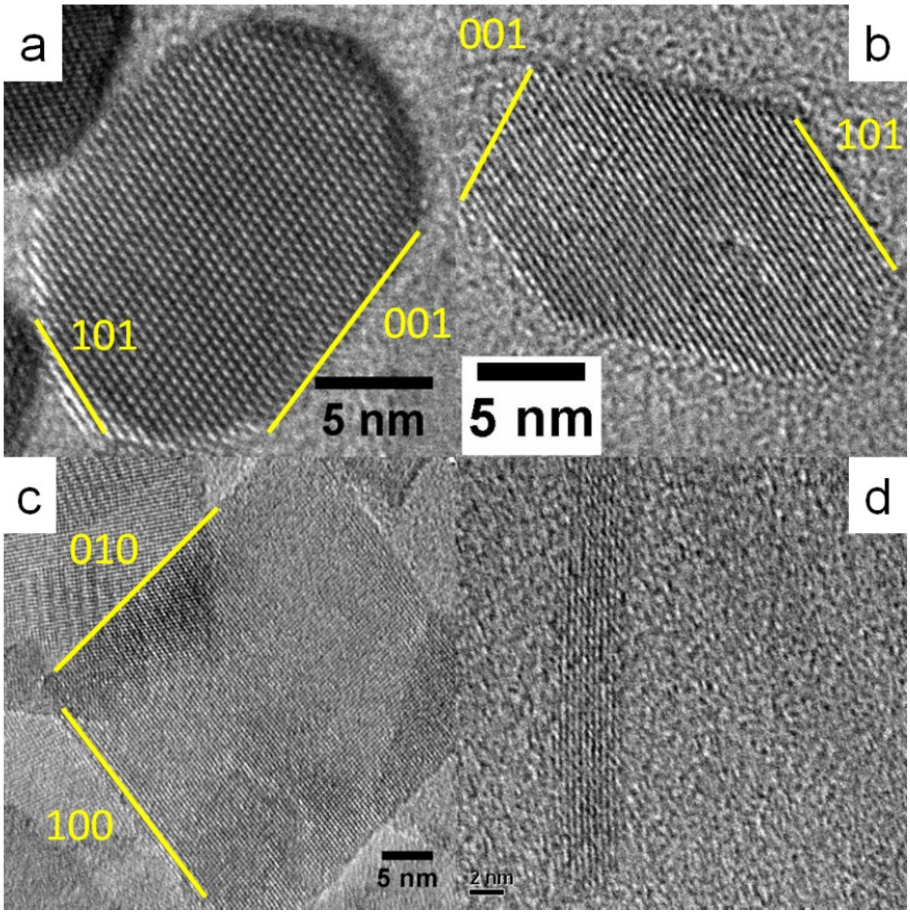

Figure 9: HRTEM images of samples a) F–OLAM, b) F–ODOL, c) M–OLAM, and d) Cl–OLAM.

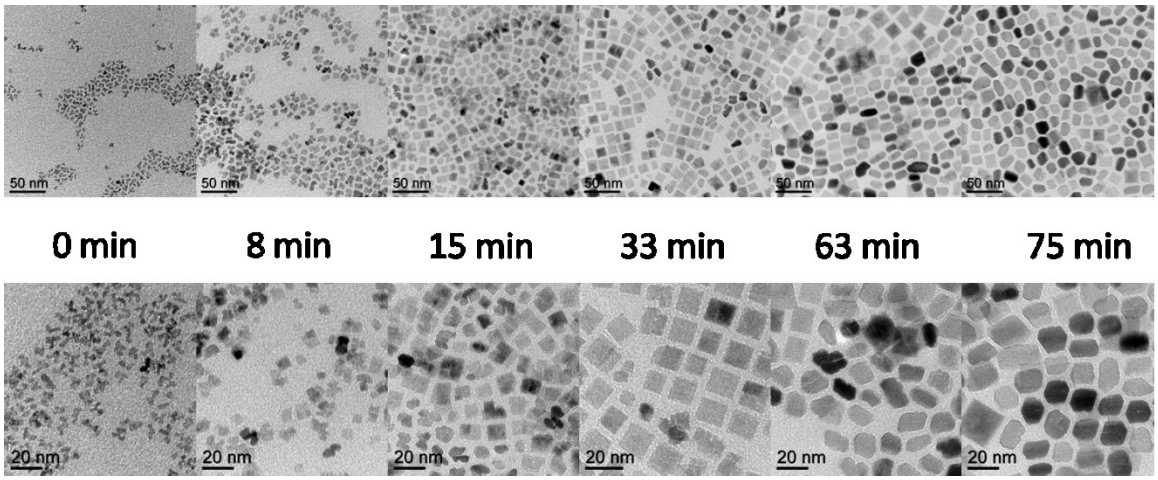

Figure 10: Representative TEM images of particle growth of sample F-OLAM as function of time with addition of F stock solution at 0.3 mL min^{-1}.

Mechanism of Shape Control.

We have demonstrated that the choice of both titanium precursor and co-surfactants dramatically influences the morphology of TiO_2 NCs. Through an investigation of the reaction mechanism under nonaqueous conditions, we can rationalize why these effects are observed. The first step in the synthesis is the dissolution of TiX_4 precursors in the presence of OLAC. Short chain carboxylic acids have been shown to complex with $TiCl_4$ at low temperature in nonaqueous solutions, resulting in the formation of stable mono- and poly-nuclear chlorotitanium carboxylate complexes and the release of HCl.[175-177] Similarly, we expect the coordination of OLAC with titanium centers upon dissolution of titanium (IV) halides (TiX_4) into solutions of OLAC/1-ODE, releasing hydrohalic acids (HX) into the solution. In the case of TiF_4, this translates to the *in situ* release of HF, which acts as a shape directing agent, providing the fluoride ions

which bind selectively to the {001} facet of anatase TiO_2 and manipulate the NC shape.[151]

In the presence of co-surfactant, the halotitanium carboxylate complex decomposes due to chemical reactions with the surfactant molecules. Aminolysis of titanium carboxylate complexes is known to occur at high temperature in solutions of OLAM, OLAC and organometallic titanium precursors, hydroxylating the titanium center (X_3Ti-OH) and producing oleyl amide as a byproduct.[145,147] The mechanism for the decomposition of the titanium complex in the presence of 1-ODOL and OLAC is more difficult to ascertain, due to the fact that multiple reaction pathways are feasible. In the absence of carboxylic acids, alcohols are known to react directly with TiX_4 to form X_3Ti-OH or titanium alkoxides (X_3Ti-OR).[22,23,178,179] In addition, the free alcohol or the formed X_3Ti-OR could react with the titanium carboxylate complex to generate X_3Ti-OH and an ester as a byproduct, as described previously.[22,23,180] We propose that a single mechanism is unlikely in the presence of 1-ODOL and OLAC. In any case, formation of X_3Ti-OH is followed by polymerization to form TiO_2 and, under nonhydrolytic conditions, the release of additional HX.

The species HF formed *in situ* is proposed to be a shape directing agent, binding selectively to the {001} facet of anatase and altering the shape of the resulting NCs. By using a mixed precursor (1:1 F:Cl), the amount of HF released is significantly reduced, and the percentage of {001} facets in the resulting NCs is

decreased. Likewise, we observe significant differences in the percentage of {001} facets depending on the choice of co-surfactant. Under otherwise identical reaction conditions, NCs produced in the presence of 1-ODOL have much higher percentages of {001} facets relative to the NCs synthesized in OLAM, indicating the presence of more HF in solution. This may be rationalized by considering the expected reaction of HF with the excess OLAM in solution to produce a primary ammonium fluoride salt ($RNH_3^+ F^-$). Through this reaction, the amine sequesters the HF generated, reducing the amount of fluorine available to bind to the {001} facet of anatase. In this way, the co-surfactant may be used to influence the particle shape. In addition to preferentially exposing the {001} facet, fluoride precursors have been shown to stabilize the anatase phase, preventing a phase transformation to rutile.[181,182] The stabilizing effect of fluorine on the anatase phase may explain why there is no phase transformation to the brookite phase in F-OLAM, as observed with Cl-OLAM.

Isolation of Transition State.

When heated to 290°C, solutions of $TiCl_4$, OLAC and 1-ODE produce no crystalline material even after hours of heating, although several color changes are observed, which have previously been attributed to the interconversion of various chlorotitanium oleate complexes.[147] In contrast to the apparent stability of the chlorotitanium oleate complexes, we observe that solutions of TiF_4, OLAC and 1-ODE decompose when heated to mild temperatures (150–200°C), forming

hexagonal phase titanium oxyfluoride ($TiOF_2$) (space group $R\bar{3}c$) nanocubes which have edge lengths of 7.3 ± 0.9 nm (Figure 11). The $TiOF_2$ nanocrystals are single crystalline, as shown by HRTEM.

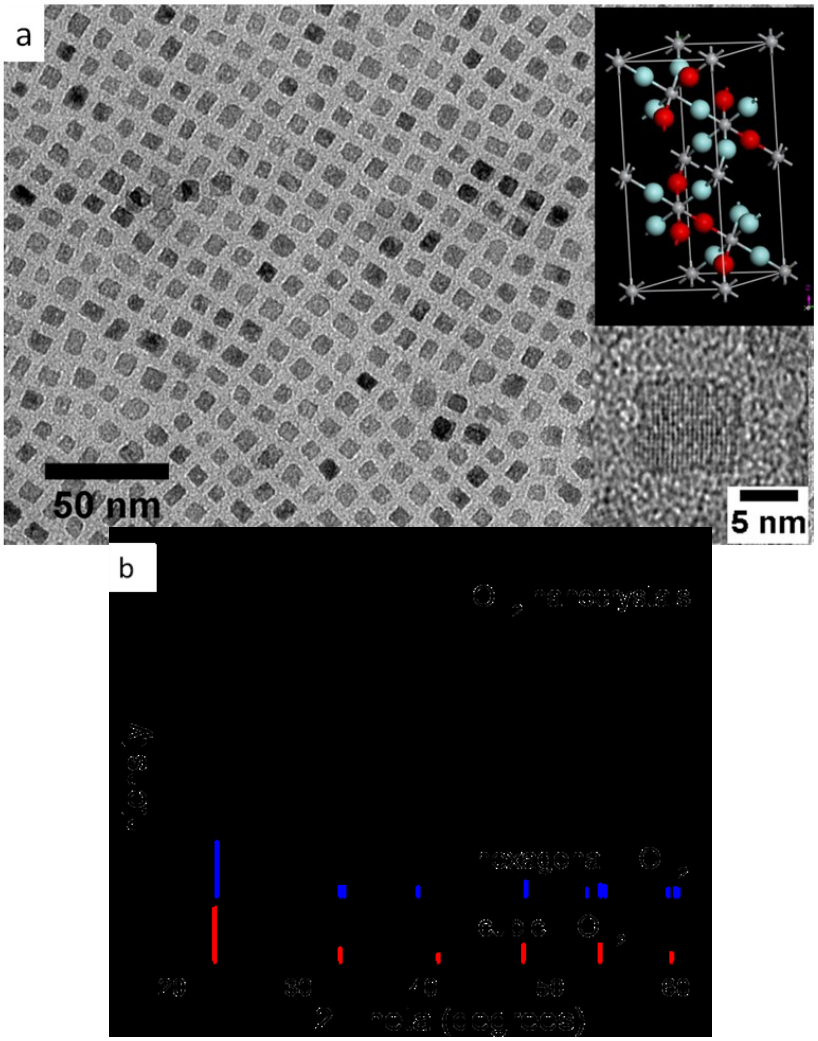

Figure 11: a) TEM image of $TiOF_2$ nanocrystals, inset shows HRTEM image of a single $TiOF_2$ NC and a unit cell of hexagonal $TiOF_2$ (space group R-3c), where grey atoms are Ti, light blue atoms are F and red atoms are O (oxygen and fluorine atoms reside on the same sites in a random configuration). b) XRD pattern of $TiOF_2$ nanocrystals compared with cubic (PDF#77-0132) and hexagonal[183] $TiOF_2$ patterns from the literature.

Bulk $TiOF_2$ has been prepared through the hydrolysis of TiF_4 or the reaction of TiO_2 with HF, but the observed crystal structure is cubic (space group $Pm\bar{3}m$).[184-186] The hexagonal phase $TiOF_2$ has only recently been reported in nanostructured films prepared through the gas/solid metathetic reaction of TiF_4 with SiO_2.[183] Broadening, as a result of the small particle size, prevents the discrimination of many peaks in the XRD of the hexagonal $TiOF_2$ nanocrystals, but the observed peak at $2\theta = 39.5°$ is deterministic of this phase, as it is not present in the cubic crystal structure. A recent publication has reported the synthesis of $TiOF_2$ nanoparticles and nanotubes using a method similar to as described here, but identify the products as being cubic phase.[187] Careful inspection of the XRD patterns reported in that work reveals a small peak at $2\theta = 39.5°$, indicative of hexagonal $TiOF_2$, suggesting that nano-sized $TiOF_2$ may have a tendency towards the hexagonal polymorph.

The formation of $TiOF_2$ in the absence of co-surfactant indicates that $TiOF_2$ may act as a transition state in the formation of TiO_2 from TiF_4 under nonaqueous conditions. Heating the fluorotitanium carboxylate species ($TiF_{4-x}(COOR)_x$) to mild temperatures likely induces thermal pyrolysis, as reported previously for titanium carboxylate species[150], resulting in the formation of $TiOF_2$ and the further release of HF.

Structural Characterization by X-ray Diffraction.

Precise knowledge of the particular facets exposed in a catalytic material is pivotal in formulating structure-activity relationships. In the case of photocatalysis on anatase TiO_2, it is well known that the percentages of {001} and {101} facets have a dramatic influence on the photocatalytic activity.[188] In the literature, the dimensions of the anatase crystals (from which the percentages of the facets are extracted) are determined through the analysis of electron microscopy images. While electron microscopy is an invaluable tool for morphological determination, image analysis to extract statistically significant shape and size information is time-consuming and is inevitably prone to bias and error. In addition, the accurate quantification of the dimension of a crystal becomes increasingly difficult with decreasing particle size. This is especially true when measuring the thickness of nanoplates and nanosheets which necessitates that the long axis of the crystal aligns nearly perpendicular to the substrate. Electron microscopy also requires significant infrastructure and is thus not always routinely achievable.

X-ray diffraction (XRD) has the advantage of being a fairly standard laboratory technique which probes the crystalline structure of a statistically large number of NCs in a single run. While XRD patterns are commonly used to identify the phases present in nanocrystalline materials, in conjunction with simulation, XRD may be used to confirm the morphology of NCs determined from electron microscopy. The Debye equation allows for the simulation of XRD

patterns based on atomistic models of NCs.[27,130] An atomistic model which is consistent with both XRD and TEM results provides an accurate picture of the average NC morphology in a given sample. We have performed simulations of XRD patterns for three samples using atomistic models derived from a statistical analysis of TEM images in which the dimensions of 200 or more individual NCs are measured. Figure 13 shows the experimental powder XRD patterns together with the simulated spectra (insets show atomistic models with accurate percentages of {001} and {101} facets but at smaller scale, for actual atomistic models see Figure 12). TiO_2 NCs are dissolved in toluene, placed in glass capillaries and the X-ray diffraction patterns are measured in transmission mode, eliminating the effects of preferred orientation which are commonly observed in films of anisotropic NCs.[39]

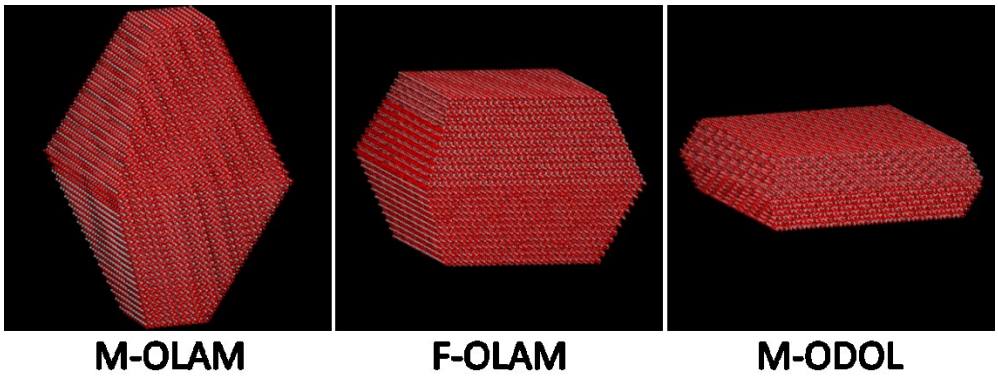

Figure 12: Actual atomistic models used in X-ray simulations, which represent the average NC size in the labeled sample.

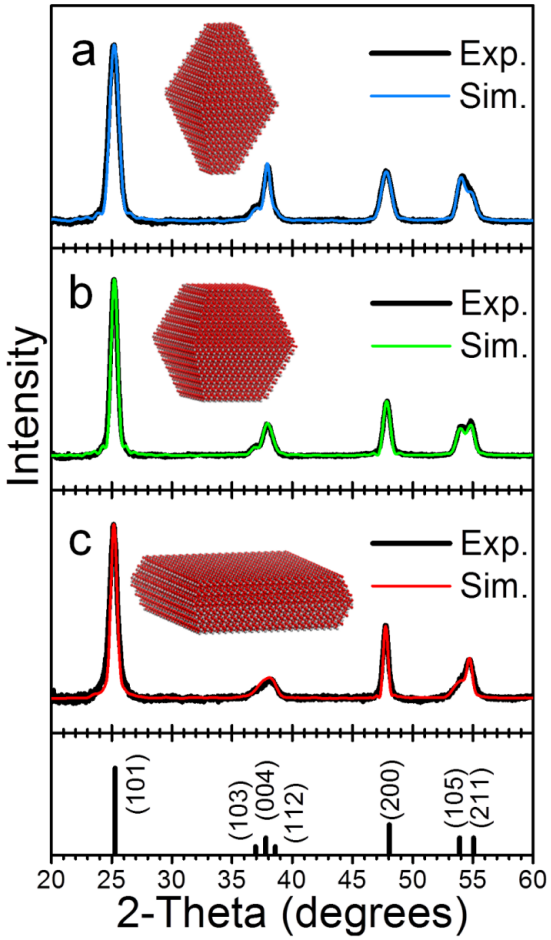

Figure 13. Experimental XRD patterns (thick black lines) plotted with simulation (thin colored lines) for TiO_2 nanocrystals a) M-OLAM, b) F-OLAM and c) M-ODOL.

Interestingly, all three anatase TiO_2 NC samples exhibit substantial deviations from standard lattice parameters. The shifting of the (200) peak at $2\theta \approx 48.0°$ and (004) peak at $2\theta \approx 37.8°$ clearly indicates expansion in the a-axis (0.3 %) and compression in the c-axis (0.39 – 0.55 %), respectively. Similar results have been reported previously for nano-sized anatase TiO_2, but significant changes in the lattice parameters are not typically observed until the

dimension of the crystallites is less than 10 nm.[189,190] Changes in the lattice parameters may be caused by the presence of oxygen vacancies or fluorine on particle surface, as described below. While the origins are beyond the scope of this manuscript, the simultaneous c-axis compression and a-axis expansion are introduced into the XRD simulation by adjusting the lattice parameters in the atomistic model in order to fit the appropriate peak position.

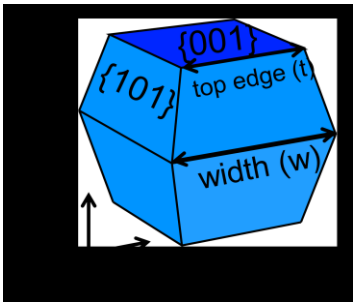

Figure 14: Model of perfect tetragonal bipyramid with labels indicating measured dimensions.

Figure 13 shows the experimental and simulated XRD pattern for three samples with different percentages of {001} and {101} facets. Based on the XRD pattern fitting, sample M-OLAM is found to be 18.0 nm in length (along the c-axis) and 10.8 nm in width (along the a-axis). This is in excellent agreement with results from a statistical analysis of TEM images (Table 1). Similarly, for the more truncated sample F-OLAM, a length of 10.8 nm and a width of 14.5 nm is determined, while for sample M-ODOL, with the highest percentage of {001} facets, is fitted to a 5.8 nm length and 18.2 nm width. Based on the length and width derived from the XRD simulation fitting, we can precisely calculate the percentages of {001} and {101} facets from the atomistic models of NCs through

basic geometric calculations. The ratio of {001} to {101} facets was calculated assuming a model in which the nanocrystals are perfect truncated tetragonal bipyramids, possessing only {101} and {001} facets (see Figure 14). The area of the {001} and {101} facets and the total surface area for a given length along the c-axis (l), width along the a-axis (w), and top edge length (t) with lattice constants c and a are given as follows:

Equation 8:
$$A_{\{001\}} = 2\left(w - l(a/c)\right)^2$$

Equation 9:
$$A_{\{101\}} = 2l^2(2(w/l) - a/c)\sqrt{1 + (a/c)^2}$$

Equation 10:
$$SA = (A_{\{101\}} + A_{\{001\}})/V$$

Equation 11:
$$V = l/3(w^2 + w * t + t^2)$$

, where $A_{\{001\}}$ is the surface area of {001} facets, $A_{\{101\}}$ is the surface area of {101} facets, V is the volume of the tetragonal bipyramid, and SA is total surface area in units of 1/m. SA is then converted to m^2/g after division by the density of TiO_2 in units of g/m^3 (density of TiO_2 = 4.23 g/cm^3). In addition to the three samples measured in transmission mode, XRD patterns for samples Cl-OLAM, Cl-ODOL and F-ODOL are recorded in reflection mode (Figure 15).

Sample	Length (nm) (TEM)	Width (nm) (TEM)	Length (nm) (XRD sim)	Width (nm) (XRD sim)	% {001}	% {101}	SA (m^2/g)
M–OLAM	18.5 ± 2.2	10.8 ± 1.4	18.0	10.8	4.5	95.5	136
F–OLAM	–	16.6 ± 1.7	10.8	14.5	26.6	73.4	111
M–ODOL	–	24.5 ± 3.8	5.8	18.2	54.3	45.7	130

Table 1: Particle size of 3 anatase TiO_2 NC samples based on statistical analysis of TEM images and best fitting XRD pattern and derived percentages of {001} and {101} facets and surface area.

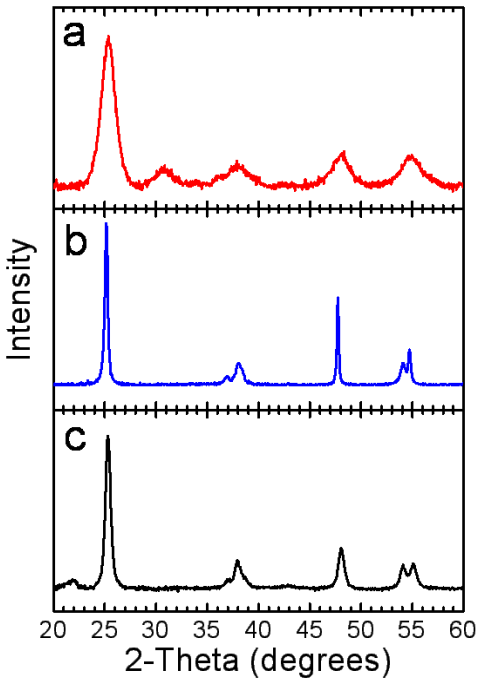

Figure 15: XRD patterns for samples a) Cl-OLAM and b) F-ODOL, and c) Cl-ODOL.

Optical Properties.

All of the samples of TiO_2 synthesized in the presence of fluorine were found to be blue in color (Figure 16a). Blue coloration has been reported previously in reduced TiO_2 (TiO_{2-x})[161,191-194] and in TiO_2 irradiated with UV light under inert atmosphere[195-197] and is characteristic of free conduction band electrons in TiO_2. In the former case, additional electrons are proposed to result from oxygen vacancies or titanium interstitials which are formed during the synthetic process. In the latter case, band gap illumination produces conduction band electrons which localize on surface Ti atoms, but this coloration is quickly quenched upon exposure to oxygen or other oxidizers,[195,196] except under

extremely high photon flux.[197] Figure 16a shows the optical absorption of sample F-OLAM dispersed in CCl_4 from the UV to the IR (300 – 5500 nm). The spectrum shows a sharp absorption edge at 380 nm (3.2 eV) corresponding to band-to-band transitions, and broad absorption throughout the visible region and NIR, which peaks in the IR at around 3400 nm. The sharp oscillations observed near the peak of absorption and in other regions of the IR (2500 – 5500 nm) result from the vibrational transitions of surfactant molecules on the particle surface and residual solvent molecules.

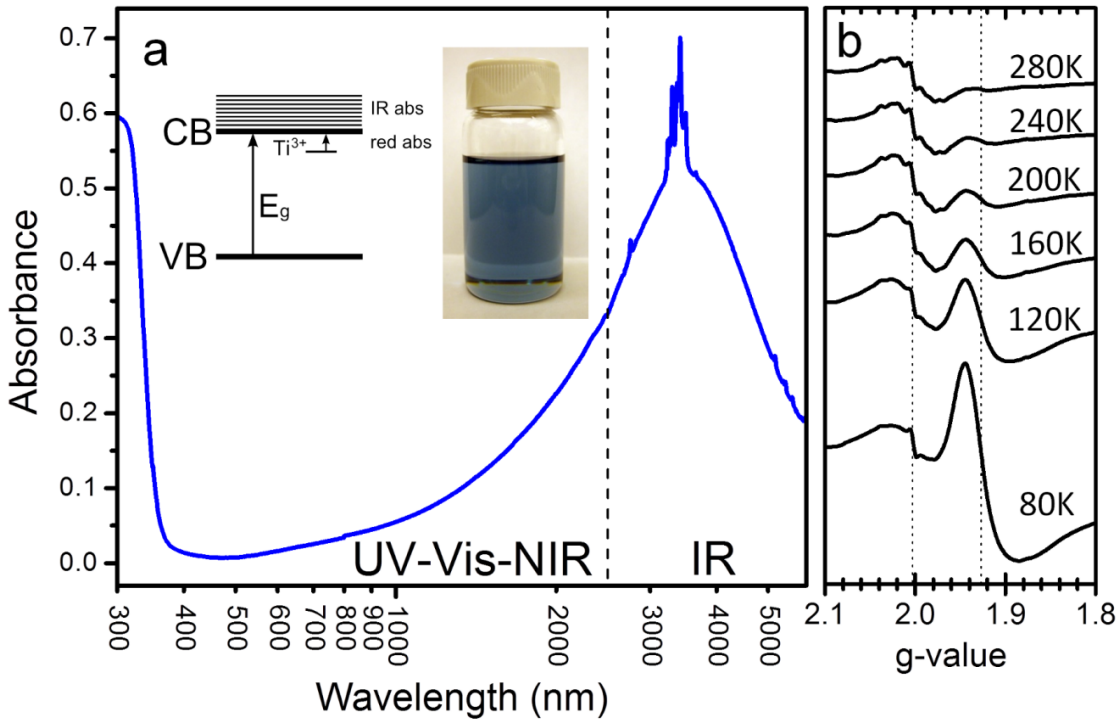

Figure 16. a) Optical absorption of sample F-OLAM dispersed in CCl_4 (dashed line at 2500 nm indicates where data is joined) and b) EPR spectra of sample F-OLAM at several temperatures. Inset of a) shows proposed band diagram of blue TiO_2 nanocrystals and an optical image of TiO_2 nanocrystals dispersed in toluene.

The diffuse reflectance spectra from 300 – 2500 nm is shown in Figure 17 for all of the synthesized TiO_2 NCs. The absorption at 380 nm is observed in all of the samples, whereas only the NCs synthesized in the presence of fluorine have a broad Vis/NIR absorption. The blue coloration is stable in air for months without noticeable changes in the absorbance and persists after annealing under a nitrogen atmosphere at 300 °C. On the other hand, the sample turns white after annealing at 300 °C in air, providing strong evidence for the presence of oxygen vacancies as described above.

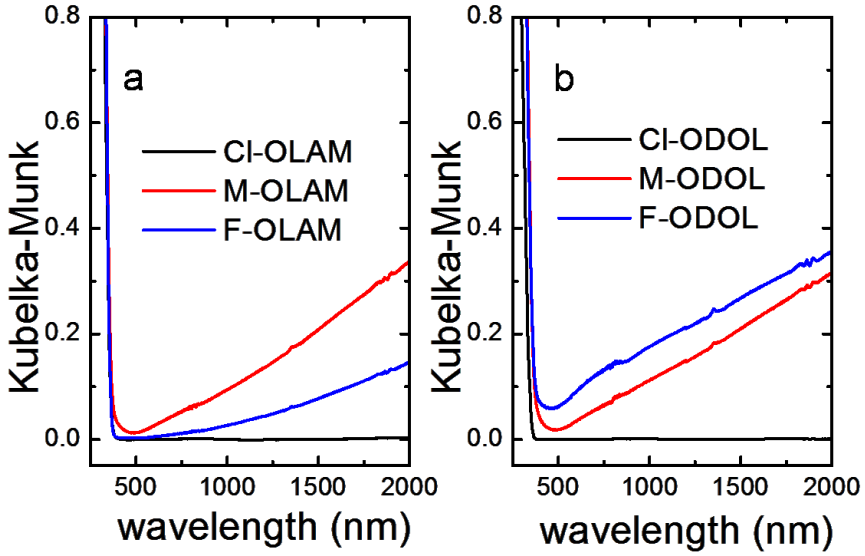

Figure 17: Diffuse reflectance spectra covering the UV-Vis-NIR (300 – 2000 nm) of TiO_2 NCs synthesized in a) OLAM and b) 1-ODOL.

We have performed electron paramagnetic resonance (EPR) studies on sample F-OLAM to determine the chemical environment of unpaired electrons in the NCs (Figure 16b). A gradual increase in signal intensity is observed with

decreasing temperature at g = 1.927, which has previously been attributed to surface and subsurface paramagnetic Ti^{3+} centers.[195,198,199] This resonance is damped at high temperatures due to fast spin relaxation times.[200] At all temperatures, a broad peak is observed at g = 2.003, which has previously been attributed to electrons localized on oxygen vacancies in TiO_2.[201-203] These results are in agreement with the optical data presented above, strongly suggesting the formation of oxygen vacancies in the synthesized NCs and the presence of free electrons which localize to form Ti^{3+} centers near the NC surface at low temperature. The absence of EPR signals at g = 1.99 and g = 1.96, which are usually observed for Ti^{3+} ions in anatase crystallites, indicates that free electrons do not occupy bulk-like Ti positions in the NCs. A proposed energy level diagram for the blue TiO_2 NCs is shown as an inset in Figure 16a, which depicts band-to-band absorption in the UV, as well as red/NIR and IR absorption which results from the absorption of electrons localized on Ti^{3+} sites and free electrons residing in the conduction band, respectively.

A broad absorption Vis-NIR-IR band is commonly attributed to the excitation of conduction band electrons in blue TiO_2 and therefore reflects the density of states of the conduction band.[191,200] On the other hand, the fairly narrow linewidth of the absorption feature in the IR region (Figure 16a) suggests that the absorption may result from a localized surface plasmon resonance (LSPR). While routinely observed in metallic nanostructures, surface plasmon

resonances, which result from the collective oscillation of electrons on the surface of a crystal, have also been recently reported in doped oxides with sufficient free carriers.[204] For highly conductive oxides (ITO, AZO, etc.), the frequency typically lies within the NIR – terahertz (THz) region of the electromagnetic spectrum, depending on dopant concentration.[108] The peak centered at 3400 nm for sample M-OLAM resembles the absorption features of doped oxide NCs recently reported in which a LSPR was identified.[108,111,116] A plasmonic resonance in TiO_2 should be considered feasible, as oxygen-deficient TiO_2 supports many free carriers and is known to produce highly conductive thin films.[191,205,206]

Microanalysis of Fluorine Environment.[III]

While the blue coloration and EPR spectra are both readily explained by the presence of oxygen vacancies, an alternative explanation for the Ti^{3+} EPR signal observed in our NCs is the substitutional doping of fluorine into the TiO_2 lattice. In this scenario, each fluorine atom that substitutes for an oxygen atom contributes an electron to the conduction band, similarly producing EPR signatures for Ti^{3+} at low temperature.[207] At first glance, this fluorine doping mechanism appears to be more probable, considering that using $TiCl_4$ (or $TiBr_4$) as the titanium precursor under identical reaction conditions results in TiO_2 NCs without blue coloration, and because no additional reductive gases are expected

[III] XPS measurements and analysis are courtesy of Dr. Filippo Mangolini

to form in the presence of TiF_4. On the other hand, the only optical changes observed for fluorine doped TiO_2 in the literature have been minor band-gap shifts, with no significant red/NIR absorption.[207-209]

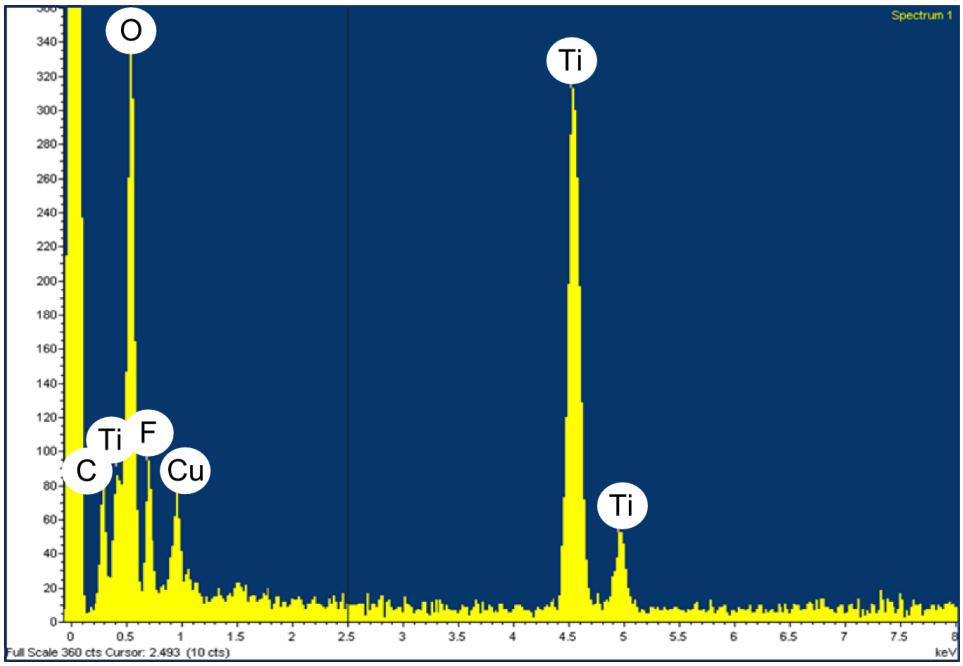

Figure 18: EDS spectrum of sample F–ODOL.

To clarify this issue, the nature of the interaction between fluorine and TiO_2 was further investigated using microanalysis techniques. Fluorine is detectable in sample F-ODOL using energy dispersive X-ray spectroscopy (EDS), despite the fact that the technique is rather insensitive to light elements such as fluorine (Figure 18). However, the relatively low concentrations make quantitative analysis using EDS prohibitive. Consequently, X-ray photoelectron spectroscopy (XPS) studies were undertaken, which not only allow for the quantification of the fluorine content, but also provide information regarding the

chemical environment of fluorine atoms in the NC samples. Figure 19 shows a survey and high resolution F1s XPS spectrum for sample F-OLAM and Figure 20 shows the F1s XPS spectra for all three samples. The centroid of the F1s peak at 684.8 ± 0.2 eV in all samples is consistent with fluorine bound to the surface of TiO_2, and does not indicate the presence of $TiO_{2-x}F_x$ species.[151,161,207,210] Based on this evidence, we propose that while fluorine is not substitutionally doped into the TiO_2 lattice, fluorine species play an important role in the formation of oxygen vacancies under the reported synthetic conditions. It is possible that the very strong bond between Ti and F (the only bond to titanium stronger than Ti-O)[211] facilitates oxygen vacancy formation.

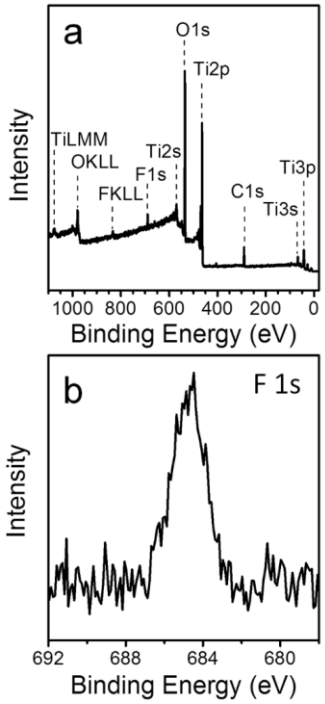

Figure 19: a) XPS survey spectrum and b) high resolution XPS spectrum of the F 1s peak for sample F-OLAM.

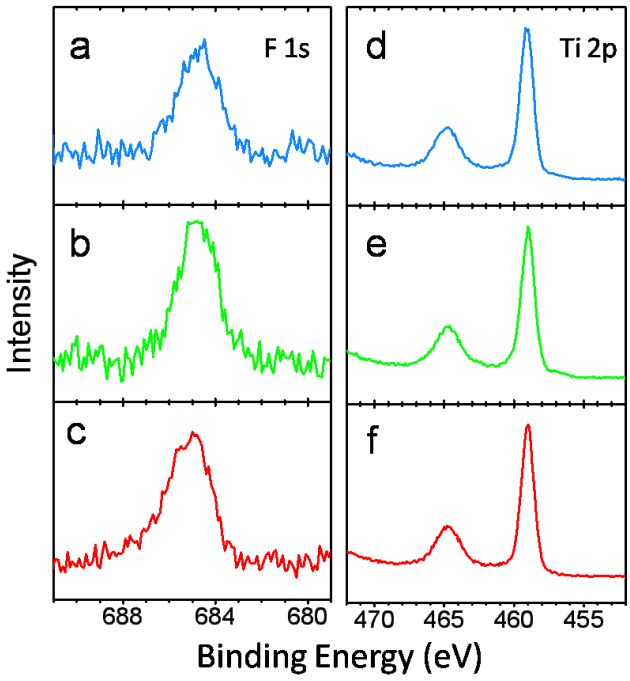

Figure 20: HR XPS spectra of the (a-c) F 1s and (d-f) Ti 2p peaks for samples (a,d) M-OLAM, (b,e) F-OLAM, and (c,f) F-ODOL.

Sample	**[F]/[Ti]**	**$[Ti^{3+}]/[Ti^{4+}]$**
M-OLAM	0.26 ± 0.05	0.023 ± 0.007
F-OLAM	0.21 ± 0.01	0.033 ± 0.005
F-ODOL	0.64 ± 0.02	0.014 ± 0.001

Table 2: Tabulated XPS results for three samples of blue TiO_2 NCs deposited on Si wafers and subjected to 4 min of Ar ion plasma.

Table 2 shows the total [F]/[Ti] ratio derived from the XPS results for samples M-OLAM, F-OLAM and F-ODOL. The NC sample with the largest percentage of {001} facets (F-ODOL) also has the highest fluorine content. This is in agreement with previous studies which indicate that fluoride bound to the {001} facet remains even after multiple washing steps and is only removed after

annealing at high temperature or treatment with concentrated sodium hydroxide (NaOH).[151,152] Figure 20 and Table 2 also display the HR Ti 2p spectra and the $[Ti^{3+}]/[Ti^{4+}]$ ratios for the three analyzed samples, respectively. This data confirms the presence of Ti^{3+} in the blue TiO_2 NCs and indicates that the $[Ti^{3+}]/[Ti^{4+}]$ ratio lies between 0.014 and 0.033.

Photocatalytic Hydrogen Evolution.[IV]

The high uniformity of the synthesized samples enables us to determine the influence of the {001} and {101} facets on the photocatalytic activity of oxygen deficient anatase TiO_2 NCs. It must be underlined that the term photocatalysis encompasses a wide variety of reactions performed under different reaction conditions, making this field quite fragmented. In the present work, we investigate the evolution of hydrogen in the presence of methanol as a sacrificial agent under simulated solar light for three samples of oxygen deficient anatase NCs. This model reaction, known also as photoreforming, is gaining increasing interest in view of sustainable production of hydrogen.[82,212]

The NCs synthesized using our method are highly hydrophobic due to the surfactants bound to the particle surface, and are not dispersible in aqueous solutions.[147] Therefore, a recently developed ligand-exchange technique utilizing $NOBF_4$ is used to disperse the photocatalyst in aqueous solution.[142] After this simple procedure, the resulting NCs are dispersible in water and aqueous

[IV] Photocatalytic activities and textural properties of TiO_2 nanocrystals were measured in collaboration with Dr. Matteo Cargnello and Dr. Paolo Fornasiero at the University of Trieste.

mixtures and standard methanol photoreforming tests can then be carried out.[142] This procedure accounts for a further advantage of the present method, which couples the extremely precise morphological control obtained through nonaqueous synthetic techniques with the subsequent water-dispersibility post ligand-exchange, which could be further exploited for biological applications. After $NOBF_4$ treatment, the water-dispersible NCs are still fluorine terminated on the surface. Recent publications indicate that the presence of surface fluorine results in similar H_2 evolution rates for the {101} and {001} facets of micron-sized anatase TiO_2 crystals.[163] In the present work, we remove fluorine from the samples with a published procedure using NaOH treatment and compare the activity before and after the treatment.[160,169]

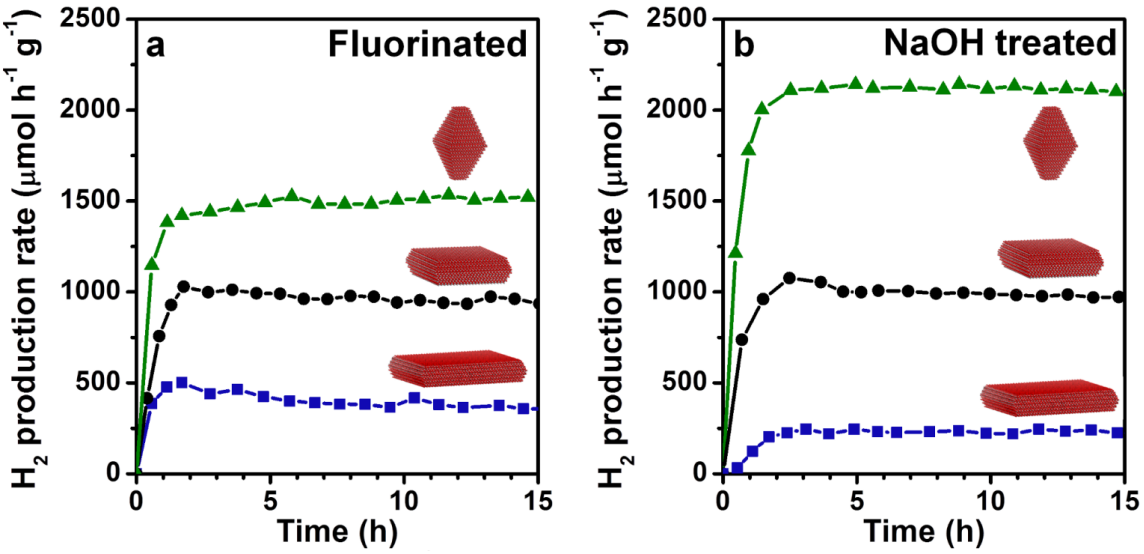

Figure 21. Hydrogen production rate from 1 wt. % Pt loaded samples of ligand exchanged, a) fluorinated and b) NaOH-treated TiO_2 NCs under solar illumination in 1:1 mixtures of MeOH:H_2O. Samples are M-OLAM (green triangles), M-ODOL (black circles) and F-ODOL (blue squares).

Figure 21 shows the rate of photocatalytic hydrogen production as a function of time under simulated solar irradiation for three selected samples of Pt/TiO_2 with different percentages of {001} and {101} facets prepared as described above, both fluorinated and NaOH treated (data for all of the fluorinated samples is shown in Figure 22). Platinum is photodeposited on the NCs to obtain a final metal loading of 1 wt. % in all the cases. The metal is necessary to ensure that photogenerated electrons are capable of reducing protons to molecular hydrogen.[81,213] No hydrogen is evolved in the absence of Pt or photocatalyst or when samples are illuminated with only visible light ($\lambda > 430$ nm). Very low, more sustainable Pt loadings (0.1 wt. %) show similar or even better overall performances (Figure 23), but a 1 wt. % Pt loading is necessary to simplify TEM characterization of the materials. An induction period of ~ 1 h is observed before the samples reach a maximum and stable H_2 evolution rate as complete photodeposition of Pt occurs. All the samples exhibit good performances, with up to ~2.1 mmol H_2 h^{-1} g^{-1} evolved under solar illumination. Although this value is lower than that obtained under similar conditions with platinized TiO_2 produced using advanced engineering[214], it is a remarkable result especially for the fluorinated samples (Figure 21a). In fact, both theoretical and experimental studies suggest that the presence of F on the {001} facet of anatase TiO_2 can result in unfavorable water dissociation[96] and reduced H_2 evolution rates.[215] It must be noted that different mechanisms can be active for

methanol photoreforming. In particular, there exists a direct pathway in which methanol adsorbs on the surface and is subsequently oxidized by photogenerated holes, and an indirect one in which water adsorbs and the hydroxyl radicals that form act as the true oxidative species.[216] In the present work, a high concentration of methanol (50 % by volume) is used, which results in the concomitant high production of formaldehyde (determined by GC-MS) and scarcity of CO_2 in the outflow. These observations suggest the predominance of the direct oxidation pathway, in which methanol interacts directly with the surface, truly acting as hole scavenger and that very little water oxidation occurs.

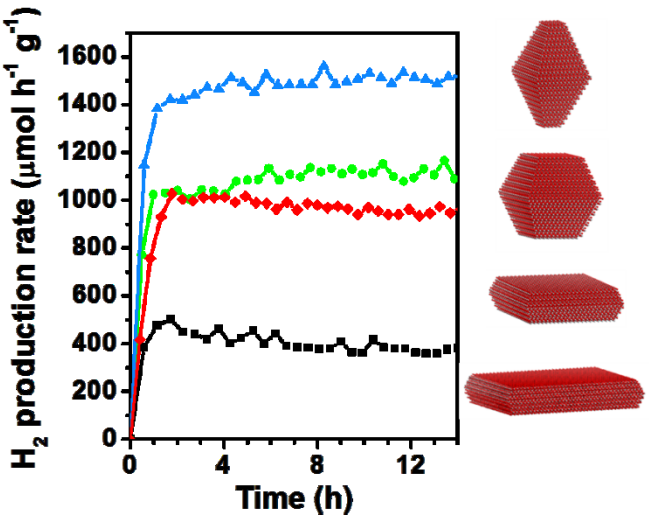

Figure 22: Hydrogen production rate from 1 wt. % Pt loaded samples of ligand exchanged TiO_2 nanocrystals under simulated solar illumination in 1:1 mixtures of MeOH:H_2O. Samples are M-OLAM (blue triangles), F-OLAM (green circles), M-ODOL (red diamonds) and F-ODOL (black squares).

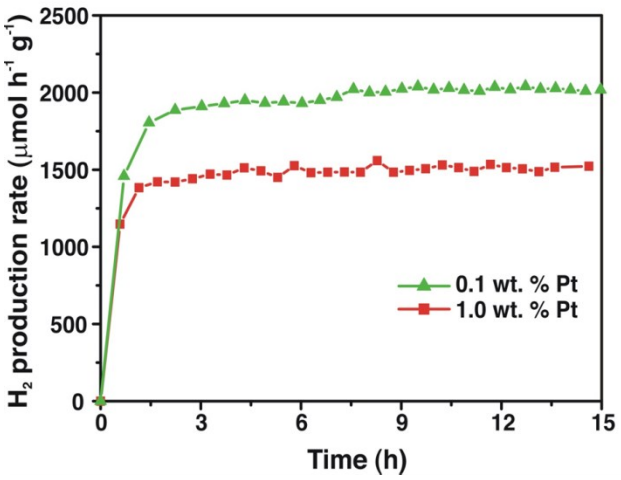

Figure 23: H_2 production rate for methanol photoreforming under simulated solar irradiation over fluorinated M-OLAM with 0.1 wt. % Pt (green triangles) or 1.0 wt. % Pt (red squares) loadings.

We observe that higher percentages of {101} facets correlate with higher photocatalytic activity for both treated and untreated samples, indicating that the {101} is more active for the production of hydrogen from methanolic solutions under the employed experimental conditions. TEM images of the samples indicate minor differences in the Pt size distributions (Figure 24), excluding a major contribution of different Pt dispersions to the reactivity of the various photocatalysts. Our results conflict with studies which indicate that the {001} facet is more reactive than {101} for photocatalytic applications due to having a more open structure with exposed undercoordinated Ti moieties.[157,217,218] On the other hand, it is in line with a recent report which suggests that the {101} surface may, in fact, be more active than the {001} for hydrogen evolution under similar reaction conditions using micron-sized anatase cyrstals.[163]

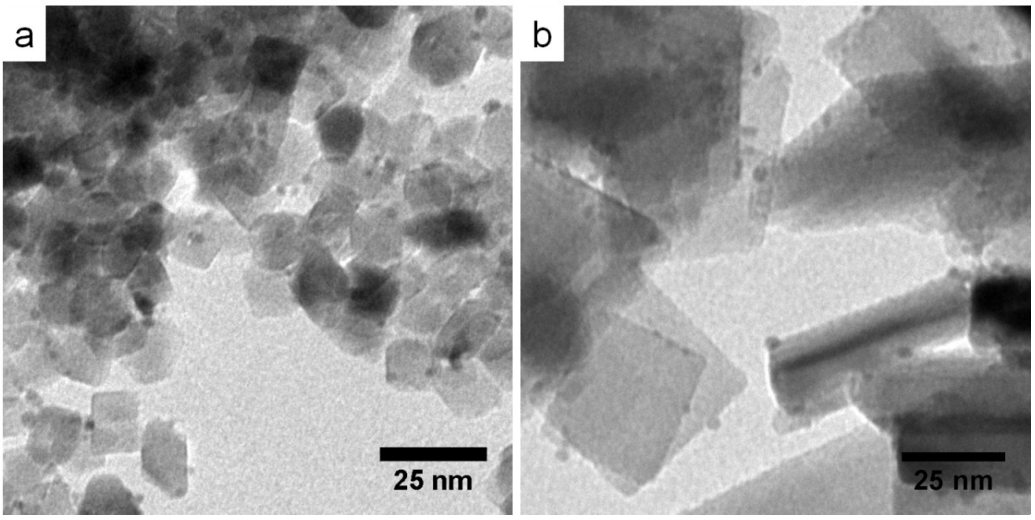

Figure 24: TEM images of samples a) M-OLAM and b) F-ODOL loaded with 1 wt. % Pt after 15 hours of photoreforming reaction in the presence of methanol.

Analysis of the samples before and after the NaOH treatment reveals intriguing changes in photocatalytic activity. The sample F-ODOL, with the largest percentage of exposed {001} facets, shows a *decrease* in photocatalytic activity after NaOH treatment. On the contrary, the sample M-OLAM, with the largest percentage of exposed {101} facets, shows an *increase* of the photocatalytic activity. To complete the picture, the activity of the sample M-ODOL, where the percentages of {101} and {001} facets are almost equal, has very similar activity after treatment. This observation implies that the activity of {101} facets is increased by NaOH treatment and that of {001} is decreased, and that these two effects are near perfectly balanced in the M-ODOL sample, where the two facets coexist equally. Although a definitive explanation for the observed trend is beyond the scope of the present work, it is reasonable to infer that the

differences in the activity can be related both to structural and electronic factors. The presence of fluorine may increase the electron and hole lifetimes in the sample F-ODOL, where many undercoordinated Ti moieties are present on the {001} facet, the benefits of which are is lost upon fluorine removal.[219] Furthermore, the increased hydroxylation of the surface following the NaOH treatment might saturate the Ti moieties on the {001} facet leading to a loss of the special reactivity demonstrated by the Ti_{5c} centers. Likewise, in the case of the sample M-OLAM with exposed {101} facets, the residual fluorine could hinder the adsorption of methanol on the octahedral Ti_{6c} sites, thus contributing to the relatively low activity when fluorinated. In this case, the removal of fluorine improves adsorption and decomposition of methanol following hydroxylation of the surface.

Sample	**Surface area ($m^2\ g^{-1}$)[a]**	**Calculated surface area ($m^2\ g^{-1}$) [b]**	**Total pore volume ($mL\ g^{-1}$)**	**D_{MAX} (nm)[c]**
M-OLAM	134	136	0.16	3.5
M-ODOL	99	130	0.17	3.6
F-ODOL	25	49	0.23	60
M-OLAM-NaOH	140	-	0.17	3.7
M-ODOL-NaOH	107	-	0.28	8.4
F-ODOL-NaOH	60	-	0.49	57

Table 3: Textural properties of the fluorinated and NaOH-treated samples. [a]According to BET method. [b]The surface area calculated as described in figure S4. For F-ODOL, size parameters are estimated from TEM analysis to be L = 12.4 nm, W = 80.1 nm. [c]According to BJH method, maximum of the pore size distribution taken from the desorption branch.

Table 3 shows the surface area of the three samples for which the photocatalytic activity is measured before and after NaOH treatment. The trend in

activity observed cannot be simply related to a difference in specific surface area of the samples. In fact, in the case of porous heterogeneous photocatalysts, the actual operating surface is unknown since portions of the sample are not illuminated as a consequence of internal shading. This element accounts for the intrinsic difficulties in obtaining reliable areal parameters in photocatalysis.[220] Furthermore, routine BET measurements can underestimate the surface area of powders composed of assembled nanocrystals, particularly in the case of the nanoplates synthesized in this work where face-to-face packing can dramatically reduce the accessible surface area. During a photoreforming reaction in which the NCs are in the dispersed state, less association between particles would cause more surface area to be exposed. In addition, when the reaction is performed in liquid phase, mass transfer effects may limit the observed activity. Supporting this argument, we observe that NaOH treatment increases the surface area of the sample F-ODOL by almost three times (Table 3), while the photocatalytic activity drops, excluding a major effect of surface area on the presented trends. In addition, the surface area of the NCs may be estimated accurately using the atomistic models derived from XRD analysis (Table 1). For sample M-OLAM, the calculated surface area is 136 $m^2 g^{-1}$ compared to a measured value of 134 $m^2 g^{-1}$, again indicating the accuracy of the XRD fitting. In contrast, the measured surface area of the two nanoplate samples, M-ODOL and

F-ODOL, deviate significantly from the calculated values, demonstrating the effect of nanoplate stacking.

Although further experiments are necessary to understand the observed differences in photocatalytic activity for the production of hydrogen over the {101} and {001} facets of anatase, our experiments utilizing well-defined nanosized TiO_2 crystals suggest that {101} facets are the more photocatalytically active than the {001} facets for the evolution of H_2 by methanol photoreforming in the presence of Pt.

2.2.4 Conclusions

We have shown that the morphology of TiO_2 NCs 10-100 nm in size may be controlled through a nonaqueous seeded growth method. The precursor TiF_4 enables the exposure of the {001} facet of anatase TiO_2 through the *in situ* release of HF. The fluoride ion from HF binds preferentially to the {001} facet and the HF concentration is controlled through dilution of TiF_4 with $TiCl_4$ and choice of co-surfactant, allowing the percentage of {001} and {101} facets to be engineered. XRD experiments, in conjunction with simulation, are introduced as a method to precisely determine the morphology of the produced NCs and quantify the percentage of {001} and {101} facets. In addition to the control provided over the NC shape, particles synthesized in the presence of TiF_4 are found to have blue coloration. The broad Vis/NIR absorption is the result of free electrons supplied by oxygen vacancies in the TiO_2 lattice. The photocatalytic

activity of three oxygen deficient anatase TiO_2 NC samples after Pt photodeposition indicate that the {101} facet is more active for the production of hydrogen from methanolic solutions under solar illumination.

2.3 Ultrathin Anatase Nanorods[V]

2.3.1 Introduction

Precise control of the shape and size of materials at the nanoscale is a central focus in the field of nanotechnology, as it allows for the optical and electronic properties of materials to be precisely correlated with structure. Through advancing colloidal synthesis methods, control over the shape and size of nano-sized crystallites or nanocrystals (NCs) has been achieved in numerous materials systems, including metals, semiconductors, and oxides.[11] Modification of synthetic parameters, such as reaction temperature and surfactant concentration allows for both shape and size to be precisely tuned using these methods.

Ultrathin metal oxide nanorods have been reported through high temperature surfactant assisted syntheses.[221,222] An interesting phenomenon, observed by many groups, is that while the nanorod length is variable, the width of the nanorods is highly uniform and very thin, often less than 2 nm.[145] At this width, a high percentage of the atoms in the nanocrystals are surface atoms, potentially leading to high photocatalytic activities, if electron-hole recombination can be suppressed. In addition, the nanocrystals are observed to self-assemble into liquid crystalline structures under appropriate deposition conditions, which

---

[V] I would like to thank Dr. Matteo Cargnello and Yupeng Lu for assistance materials synthesis and in the collection of photocatalytic activities and Ben Diroll for collecting the SAXS pattern.

could allow for the production of photocatalytically active thin films with tunable orientation and packing arrangements.[221,223-225]

In this work, we present the synthesis and selective purification of anatase TiO_2 nanorods. The single crystalline nanorods produced in solution are transferred from nonpolar to purely aqueous phase through a newly developed ligand-exchange procedure, allowing for the photocatalytic activity for methylene blue degradation to be measured.

2.3.2 Experimental

Chemicals.

The following chemicals are used as received without further purification. Titanium (IV) isopropoxide (TTIP, 99%), nitrosonium tetrafluoroborate ($NOBF_4$), 1-octadecene (90%) (1-ODE), methylene blue, N,N-dimethylformamide (DMF), toluene, hexanes, acetone, methanol and 2-propanol are purchased from Acros Organics. Oleylamine (OLAM, 70%), oleic acid (OLAC, 90%), and acetonitrile (ACN) are purchased from Sigma Aldrich.

Synthesis of TiO_2 nanorods:

All syntheses are performed using standard Schlenk line techniques under nitrogen atmosphere. In a 250 mL flask, 60 mL of 1-ODE and 15 mL of OLAC are degassed at 120 °C for 1 hour under vigorous stirring. After placing the reaction under nitrogen environment, 3.4 mL of TTIP are added to the solution and the reaction is heated to 260 °C. Once stable, 5 mL of OLAM are injected quickly

into the flask and the reaction is heated at 260 °C for 1 hour. Then, the heating mantle is removed and the reaction is allowed to cool to RT.

Purification and Size-Selective Precipitation:

The resulting reaction is diluted to 90 mL with hexanes, forming a transparent yellow solution, and is divided into 15 mL aliquots. Then, acetone is slowly added to each aliquot. Once roughly 10 mL of acetone is added, the solution becomes slightly turbid. Centrifugation at 6000 rpm for 3 min is used to separate the longest nanorods. Then, an additional 2.5 mL of acetone are added to precipitate more material, followed by centrifugation at 6000 rpm for 3 min to separate. This procedure is repeated to isolated material of progressively smaller particle size.

Ligand Exchange with $NOBF_4$.

In a centrifuge tube, 0.1 g of $NOBF_4$ and 10 mL of ACN are combined and sonicated, resulting in the formation of a yellow solution indicating the solublization of $NOBF_4$. 10 mL of the $NOBF_4$ saturated ACN is added to the hexanes solution (10 mL) of NCs (50-150 mg). The NCs quickly become insoluble and are collected through centrifugation. The solid is then completely solubilized in DMF with sonication. To remove residual organics, DMF solutions are washed through the addition of a mixture of toluene and hexanes until precipitation occurs, followed by centrifugation. This process is repeated three times. The sample is then dried in an oven, and ground in an agate mortar.

Photocatalytic Activity.

Photocatalytic degradation of methylene blue is performed to test the photocatalytic activity of anatase nanorods. 20 mg of the ligand exchanged powder is combined with 40 mL of 5 x 10^{-5} M methylene blue in water in a glass cup. The cup is then placed in a stainless steel container with Teflon insert, a sapphire window and stainless steel tubes which allow air to enter. The resulting transparent solution is stirred for 30 minutes to allow for the adsorption of dye to occur, and is then illuminated starting at time 0 through the quartz window with a 200 W Hg(Xe) lamp without any optical filter. 0.5 mL samples are removed every 5 min, the TiO_2 is separated by filtration through a 0.2 μm PTFE filter, and the UV-vis spectrum of the dye is measured.

Characterization.

Transmission electron microscopy (TEM) images were recorded using a JEOL JEM1400 TEM equipped with a SC1000 ORIUS CCD camera operating at 120 kV. High-resolution TEM (HRTEM) images were recorded on a JEOL 2010F operating at 200kV. Samples were prepared by drop-casting a dispersion of NCs in toluene or hexanes on a 300 mesh carbon-coated copper TEM grid followed by drying at 50 °C under vacuum. All X-ray diffraction (XRD) patterns were recorded on a Rigaku Smartlab diffractometer equipped with a Cu K_α source.

2.3.3 Results and Discussion

Ultrathin anatase TiO_2 nanorods are produced using a scaled up and slightly modified version of a previously described hot-injection procedure based on aminolysis of a titanium carboxylate complex.[145] The reaction begins with the formation of a titanium carboxylate complex at low temperature through addition of TTIP to a solution of OLAC and 1-ODE. The solution is then heated to 260°C, where the complex is stable, with no crystallites being observed even after extended heating.[150] When the temperature is stabilized, OLAM is injected into the reaction, causing the decomposition of the carboxylate through aminolysis to form oleyl amide as a byproduct, as depicted in Figure 25.

(1) $Ti(OR)_4 + R\text{-}COOH \longrightarrow Ti(OR)_{4-x}(RCOO)_x + ROH$

(2) $Ti(OR)_{4-x}(RCOO)_x + R\text{-}NH_2 \longrightarrow Ti(OR)_{4-x}(OH)_x + R\text{-}NHC(=O)\text{-}R$

Figure 25: Reaction mechanism describing the (1) formation of carboxylate from TTIP and oleic acid and (2) aminolysis of the carboxylate to form hydroxylated Ti centers and an oleyl amide byproduct.

The decomposition of the titanium carboxylate results in the formation of anatase TiO_2 nanorods which are very thin in diameter and variable in length from 10 to 40 nm (Figure 26). The nanorods of differing length can be effectively separated through size selective precipitation (SSP) of the reaction mixture. SSP is a purification method which relies on the fact that the magnitude of the Van der Waals attraction between particles increases with increasing particle size, and is a common method to improve the monodispersity of a sample of nanocrystals.[27]

A non-solvent in which the particles are insoluble due to their hydrophobic exterior (in this case, acetone) is added to a solution of nanocrystals in which the particles are highly soluble. The largest particles begin to aggregate when a critical amount of non-solvent is added, and can be separated through centrifugation. Addition of more non-solvent will cause the precipitation of the next largest set of particles, which can be separated, and the process is continued.

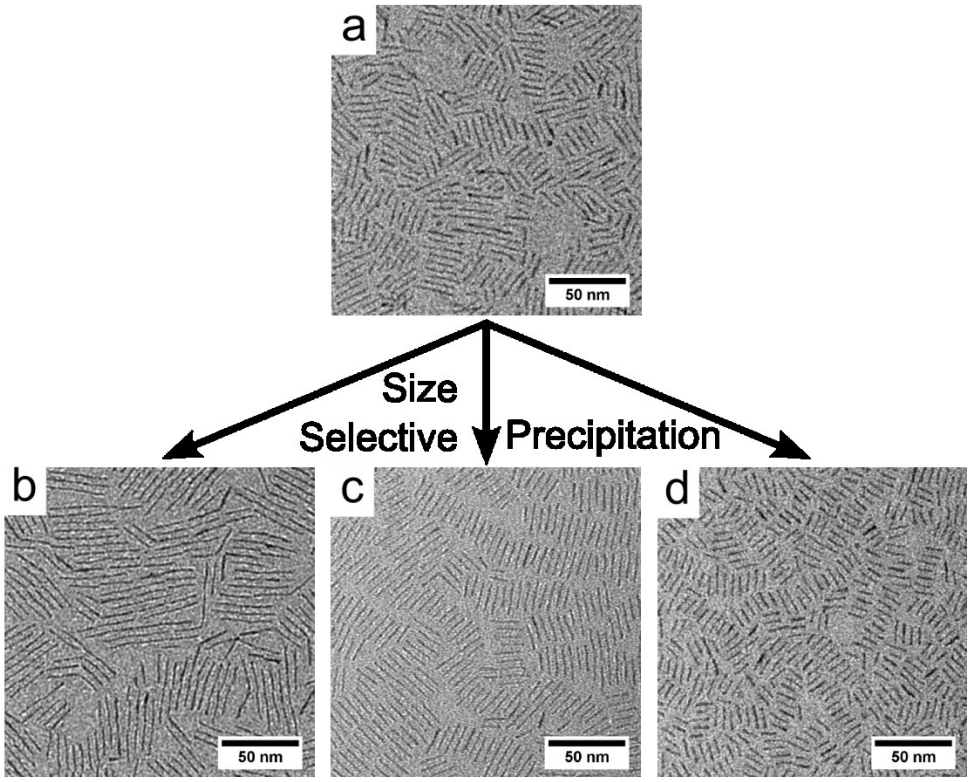

Figure 26: TEM images of anatase TiO_2 nanorods (a) before and (b-d) after size selective precipitation, where b is the first fraction separated, and d is the last fraction.

The unique aspect for the TiO_2 nanorods described in this work is that separation of the nanorods by length is highly efficient and results in isolation of quite monodisperse rods with different lengths. It is also important to note that the SSP is only effective when a large excess of oleic acid is present in the nanocrystal solution. In fact, if all of the nanorods are first collected through addition of excess antisolvent and then SSP is performed, very poor separation results. This observation suggests the influence of depletion attraction on the SSP process.

Depletion attraction is a phenomenon known for many years to explain the interactions of polymers in colloidal solution,[226] but recently was utilized to rationalize the self-assembly of nanocrystals.[227-230] Essentially, depletion attraction is explained as follows: In a solution of particles, two particles will inevitably approach each other in solution. If there is a sufficiently large concentration of macromolecules (i.e. surfactants) in solution and the distance between the two particles becomes smaller than the size of the macromolecule, then only solvent molecules can occupy this space and an osmotic force will develop, forcing the particles together. In the case of the purification of TiO_2 nanorods, this attractive force is proposed to enable size sorting, by favoring the interactions between nanorods with similar length to maximize particle-particle contact.

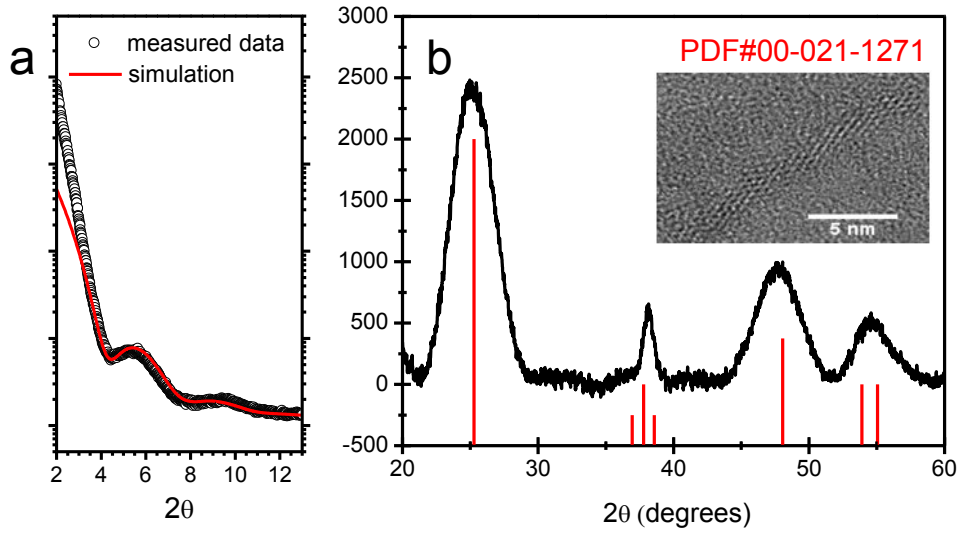

Figure 27: A) SAXS data with Debye simulation plotted and B) WAXS pattern of anatase TiO_2 nanorods with HRTEM as inset.

In the previous report upon which this synthesis is based, the authors report that injection of different volumes of OLAM was found to modulate the length of the nanorods.[145] This result was not replicated in our studies. In fact, modulating the OLAM injection volume from 1 mL to 10 mL was found to have little influence on the resulting particle morphology. Instead, different lengths of nanorods are simply separated by size selection. HRTEM and WAXS studies confirm the anatase polymorph as described previously (Figure 25). The SAXS pattern of the nanorods is shown in Figure 27a and is fitted using the Debye equation, as described in 2.2.2. For nanorods of this aspect ratio, the SAXS pattern is primarily sensitive to the width of the nanorods, with little change in the simulation observed with changing nanorods length. Nevertheless, the simulation

gives an accurate value for the nanorods width of 2.5 ± 0.2 nm, which is in line with what is observed by TEM analysis.

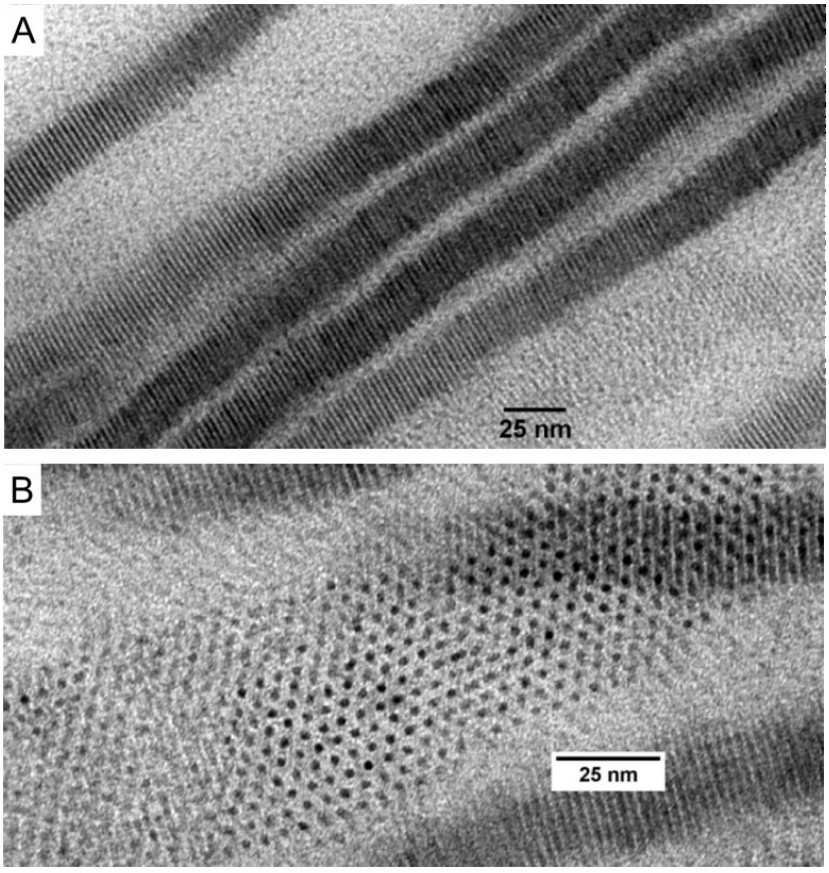

Figure 28: Self-assembled structures of TiO_2 nanorods, indicating A) lamellar type assembly and B) hexagonally close-packed vertical alignment.

Upon dropcasting or slow drying of nanocrystal solutions onto TEM grids, self-assembly of the nanorods is observed (figure 2). Two modes of self-assembly occur, lamellar side-by-side assembly in which the nanorods form chained 1-dimensional structures, and vertical assembly in which nanorods assemble 2-dimensionally perpendicular to the substrate in hexagonally close-

packed lattices. Similar self assembly behavior has been reported for nanorods of various materials and is enabled by the favorable interaction between surfactant chains on the particle surface and the driving force to achieve the highest packing densities.

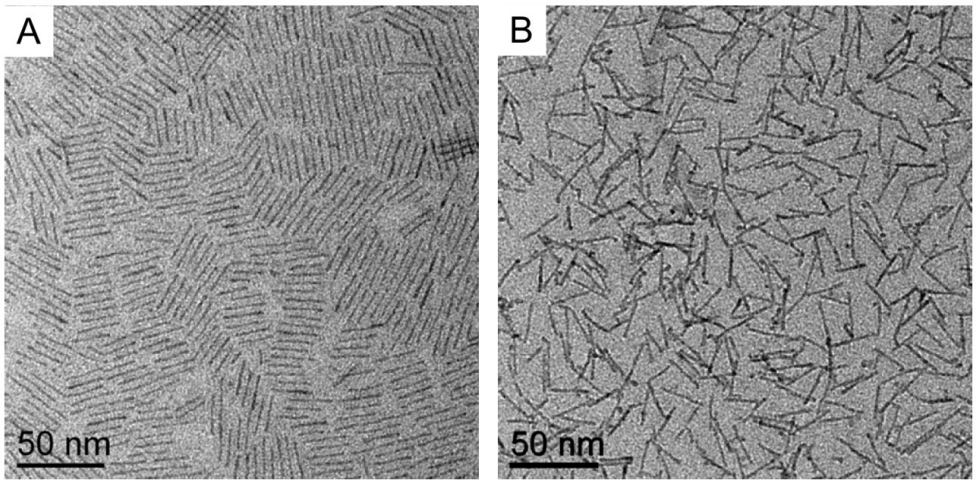

Figure 29: TEM images of TiO_2 nanorods A) as synthesized and B) after $NOBF_4$ treatment.

Anatase TiO_2 nanorods can be transferred from non-polar solvents to polar solvents using a ligand exchange procedure involving the small molecule $NOBF_4$.[142] First, a saturated solution $NOBF_4$ is produced in acetonitrile with sonication. Then, this solution is added to a solution of nanocrystals in hexane in equal volume. The nanorods precipitate and may be redissolved in N,N-dimethylformamide or dimethyl sulfoxide and are washed with toluene and hexanes to remove excess ligand. Post-treatment, the particles are found to possess a positive charge by zeta potential measurements.[142] The positive charge is proposed to result from cationic sites on the particle surface which

once were bound to ligands. The BF_4^- acts as a counter ion for this charge, but is loosely bound to the particle surface.[142]

Figure 30 shows the results of the photocatalytic degradation of methylene blue in the presence of ligand-exchanged anatase nanorods under UV-vis illumination. The degradation (or decolorization) of methylene blue follows Lanmuir–Hinshelwood kinetics, with an approximate first order rate constant of 0.01024 s^{-1}, which is of the same order of magnitude as other TiO_2 photocatalysts.[231,232] Within 90 minutes, the anatase nanorods completely degrade the methylene blue, making it a promising material for photooxidation reactions which is prepared and activated without any high temperature annealing.

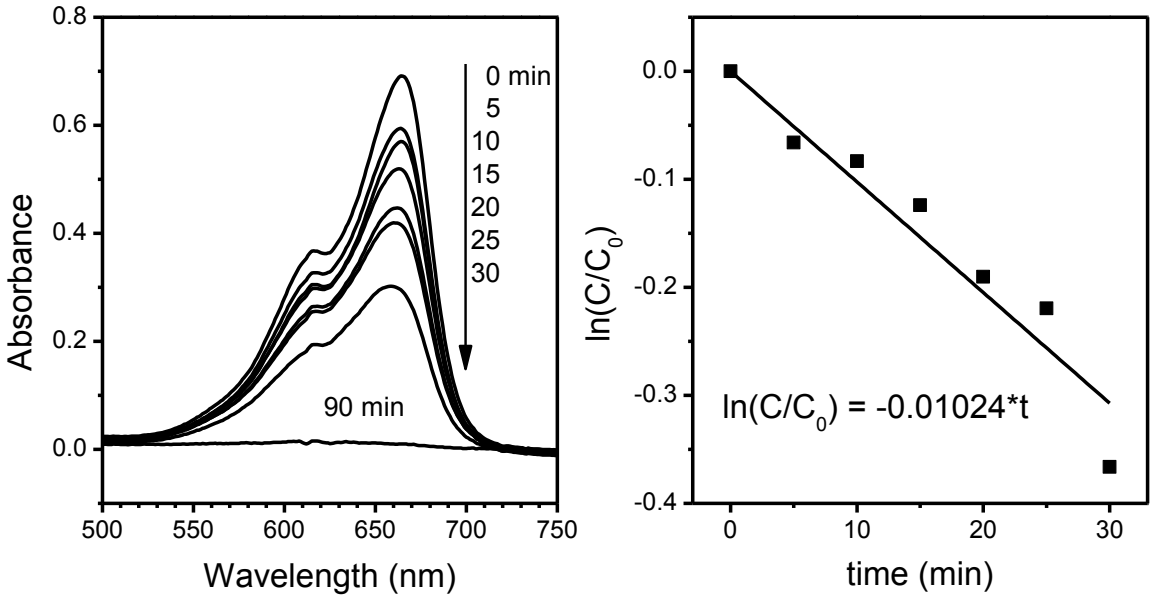

Figure 30: Temporal progression of methylene blue absorbance during photocatalysis in the presence of ultrathin anatase nanorods.

2.3.4 Conclusions

In this section, we report the synthesis of ultrathin anatase TiO_2 nanorods through a hot-injection method. The nanorods are observed to be highly uniform in width, but variable in length. Using SSP, the nanorods are very efficiently separated from each other based on length. The efficiency of this SSP procedure is attributed to depletion attraction forces in the presence of oleic acid, which enables improved size sorting. The nanorods may be self-assembled into liquid crystalline superlattices, including hexagonally close-packed vertical assemblies and lamellar side-by-side assemblies. The anatase nanorods can be transferred to polar solvents through ligand exchange procedure and are found to be active for the photocatalytic degradation of methylene blue. Future work should focus on the influence of nanorods length on photocatalytic activity.

2.4 Highly Photocatalytically Active Brookite TiO_2 Nanorods[VI]

2.4.1 Introduction

As stated in section 2.1, three polymorphs of TiO_2 exist under natural conditions: rutile, anatase, and brookite. Structurally, anatase and rutile are very similar; both having tetragonal unit cells, while brookite has an orthorhombic crystal structure.[132] Among these polymorphs, anatase is commonly considered to be the most photocatalytically active, and is the standard choice for photocatalytic studies.[132] On the other hand, studies on the photocatalytic activity of brookite TiO_2 are limited due the difficulty of isolating it in pure form.[136] Brookite is primarily observed as an impurity during the synthesis of the other polymorphs. Determining the photocatalytic activity of brookite is important to understand how the unique crystal structure, band structure, and surface faceting of this polymorph influence its reactivity.

Preparation of pure-phase nanocrystalline brookite has been accomplished through hydrothermal methods, primarily under highly basic conditions and in the presence of liquid ammonia or amines.[136,233-237] Recently, Buonsanti, et al. demonstrated a major advance in the synthesis of pure-phase brookite TiO_2 nanomaterials through a nonaqueous surfactant-assisted approach.[147,238] A seeded growth approach was utilized, wherein anatase seeds

---

[VI] I would like to thank Dr. Matteo Cargnello, Prof. Paolo Fornasiero, and Yupeng Lu for assistance materials synthesis and in the collection of photocatalytic activities.

are first produced at high temperature and then additional precursor is slowly added via syringe pump (see section 1.1.6). The added solution causes the seeds to slowly grow into large brookite nanorods, in which a solid phase transition is proposed through a dissolution-crystallization process.[147]

In our work, we study the shape dependent photocatalytic activity of brookite TiO_2 rods prepared through nonaqueous synthesis that are shown to be highly active for the evolution of hydrogen from methanolic solutions. We demonstrate that brookite phase nanorods can be produced through a heating-up method, not only seeded growth, generating smaller diameter brookite nanorods. Also, a review of the literature suggests that the brookite phase of TiO_2 selectively formed in the presence of amines. Results suggest that brookite nanorods should be explored further as a class of anisotropic photocatalysts.

2.4.2 Experimental

All syntheses are performed using standard Schlenk line techniques under nitrogen atmosphere. A general procedure proceeds as follows.

Chemicals.

The following chemicals are used as received without further purification. Titanium (IV) chloride ($TiCl_4$, 99%), nitrosonium tetrafluoroborate ($NOBF_4$), 1-octadecene (90%) (1-ODE), 1-octadecanol (1-ODOL, 97%), N,N-dimethylformamide (DMF), toluene, hexanes, acetone, methanol and 2-propanol are purchased from Acros Organics. Oleylamine (OLAM, 70%), oleic acid

(OLAC, 90%), acetonitrile (ACN) and potassium tetrachloroplatinate(II) (K_2PtCl_4, ≥99,9%) are purchased from Sigma Aldrich.

Preparation of Stock Solutions.

Stock solutions are prepared in a glovebox under N_2 atmosphere. Stock solution #1 consists of 0.2 M $TiCl_4$ and 1.0 M OLAC in 1-ODE, stock solution #2 consists of 0.5 M $TiCl_4$ and 1.0 M OLAC in 1-ODE. Once dissolved, the $TiCl_4$ stock solutions are dark brown.

Seeded growth synthesis of brookite NRs.

In a 125 mL flask, 30 mmol of co-surfactant (OLAM or 1-ODOL), 10.2 mL of 1-ODE and 0.48 mL (1.5 mmol) of OLAC are combined and degassed at 120 °C for 1 hour. After degassing the flask, 1.5 mL of the desired stock solution is added at 60 °C. Then, the solution is quickly heated to 290 °C and held 10 min to allow for the formation of seed crystals. 8 mL of the stock solution are then pumped into the flask kept at 290 °C at 0.3 mL min^{-1} using a New Era Pump Systems NE-1000 syringe pump. Afterwards, the heating mantle is removed and the flask left to cool naturally to ambient temperature.

Heating-up synthesis of brookite NRs.

In a 125 mL flask, 15 mL of OLAM is degassed at 120 °C for 1 hour. Then 15 mL of the desired stock solution is injected slowly and the reaction is quickly heated to 290°C and is held for 30 min. Then, the heating mantle is removed and the flask left to cool naturally to ambient temperature.

Workup.

Post-synthesis, the reaction contents are first diluted with a small volume of toluene and are centrifuged at 6000 rpm to separate the nanorods. The nanorods are then redispersed through addition of toluene and 100 µL of OLAM with sonication. Insoluble surfactant and agglomerated particles are removed through centrifugation. A mixture of 2-propanol and methanol are added to precipitate the NCs, and centrifugation at 6000 rpm is used to recover the NCs. This washing process was repeated twice.

Ligand Exchange with $NOBF_4$.

In a centrifuge tube, 0.1 g of $NOBF_4$ and 10 mL of ACN are combined and sonicated, resulting in the formation of a yellow solution, indicating the solublization of $NOBF_4$. 10 mL of the $NOBF_4$ saturated ACN is added to the hexanes solution (10 mL) of brookite nanorods (50-150 mg). The brookite nanorods quickly become insoluble and are collected through centrifugation. The solid is then completely solubilized in DMF with sonication. To remove residual organics, DMF solutions are washed through the addition of a mixture of toluene and hexanes until precipitation occurs, followed by centrifugation. This process is repeated three times. After the final centrifugation, the NCs are dried in a vacuum oven at 60 °C overnight to remove residual solvent molecules. Once dry, each sample is ground in an agate mortar and pestle into a fine powder with grain dimensions below 150 μm.

Photocatalytic Activity.

The photocatalytic activity of the ligand-exchanged nanorods is evaluated for hydrogen production using methanol as model sacrificial agent. ~27 mg of the NCs are suspended with sonication in 80 mL of an aqueous solution of methanol (1:1 by volume, final concentration of nanorods ca. 0.3 M). H_2PtCl_4 is added to obtain a final loading of platinum of 1 wt. %. The suspension is irradiated using a Hg lamp. An Ar flow (10 mL min^{-1}) ensures the complete removal of air from the reactor and that the reaction products reach the detector. Gaseous products are analyzed by gas chromatography (GC) using a thermal conductivity detector (TCD) for the quantification of H_2 and CO_2 with He as carrier.

Characterization.

Transmission electron microscopy (TEM) images were recorded using a JEOL JEM1400 TEM equipped with a SC1000 ORIUS CCD camera operating at 120 kV. High-resolution TEM (HRTEM) images were recorded on a JEOL 2010F operating at 200kV. Samples were prepared by drop-casting a dispersion of NCs in toluene or hexanes on a 300 mesh carbon-coated copper TEM grid followed by drying at 50 °C under vacuum. All X-ray diffraction (XRD) patterns were recorded on a Rigaku Smartlab diffractometer equipped with a Cu K_α source.

2.4.3 Results and Discussion

Brookite nanorods are produced using two methods which rely on a similar reaction mechanism as outlined in section 2.2.3. Aminolysis of a titanium

carboxylate species results in the formation of TiO_2 and an oleyl amide species as a byproduct. The first is a reported method, which was also outlined in section 2.2.3 for the synthesis of anatase nanocrystals, involves a seeded growth approach in which anatase seeds are first produced at high temperature, and then stock solution is added slowly via syringe pump at high temperature. The second method relies on a heating up method, in which all reagents are combined at low temperature and are heated to the high temperature, without any injection. Figure 31 outlines the synthetic scheme for each reaction.

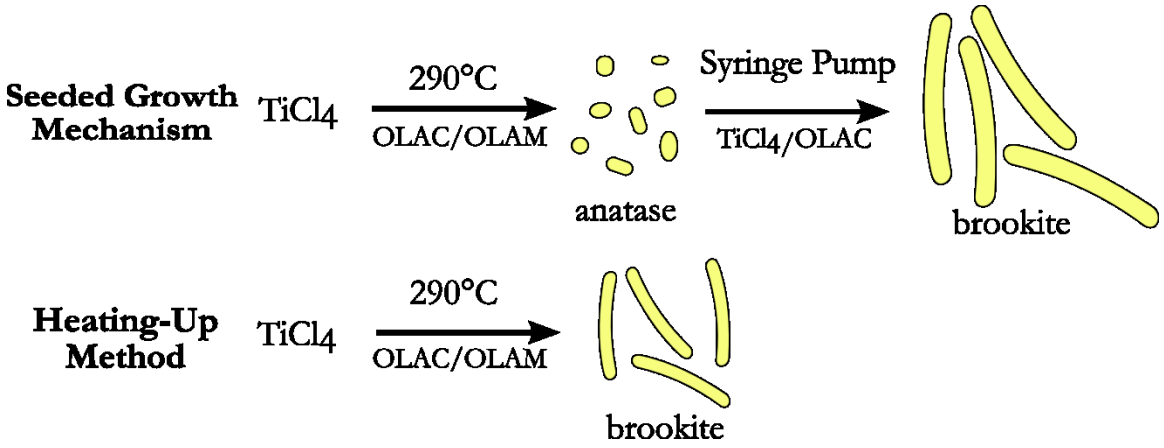

Figure 31: Synthetic schemes for two methods of producing brookite nanorods.

TEM images of brookite nanorod samples prepared using each synthetic scheme are shown in Figure 32. For both methods, the width of the nanorods can be altered through choice of the stock solution concentration of $TiCl_4$. Using stock #1 (with 0.2 M $TiCl_4$), nanorods have a smaller aspect ratio (length/width) than those prepared using stock #2 (0.5 M $TiCl_4$). In the seeded growth method, the nanorods grow larger as more stock solution added, as depicted in Figure 33,

where aliquots are taken out during the course of a single reaction using stock #1. In this way the length of the nanorods can be effectively tuned from 2.5 x 9 nm (anatase seeds) to 5 x 55 nm long (brookite nanorods). This allows for nanorods of different sizes to be recovered.

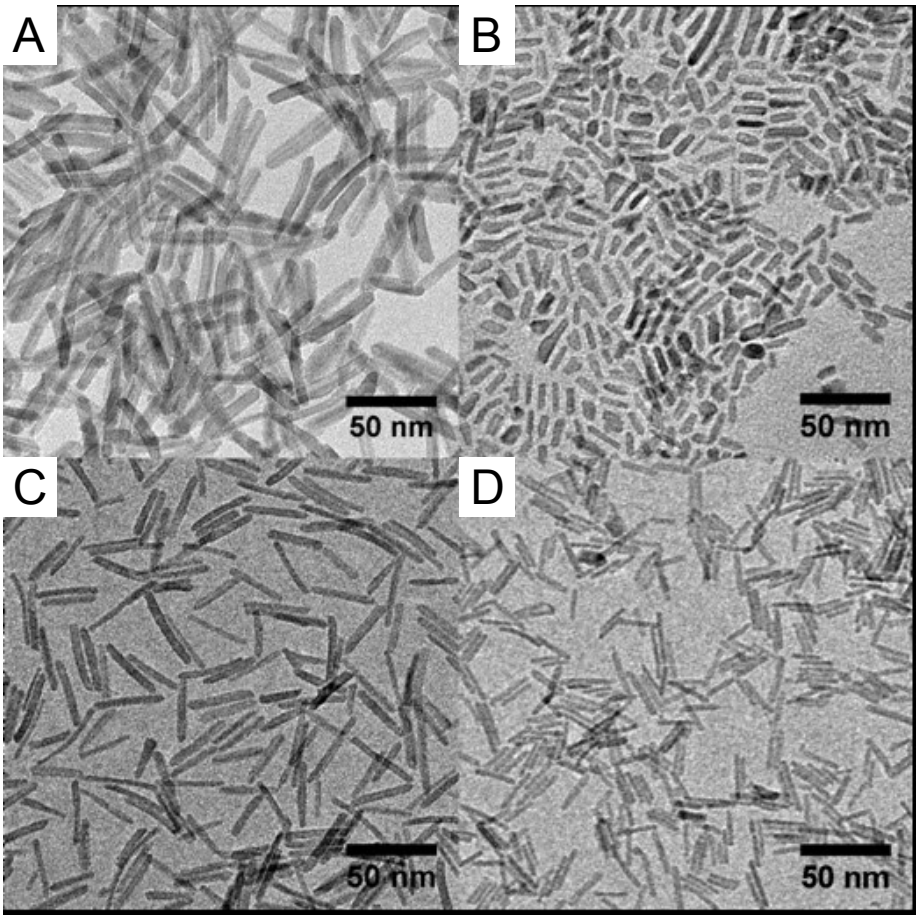

Figure 32: TEM images of brookite nanorods produced by seeded growth after 8 mL of stock addition (a,c) and heating up methods (b,d) using stock #2 (a,b) and stock #1 (c,d).

Interestingly, as briefly mentioned in section 2.2, brookite nanorods are always isolated when a $TiCl_4$ is utilized as the Ti source and oleylamine acts as the cosurfactant. When alcohols are used as cosurfactants, TiO_2 is still formed,

through a number of possible mechanisms, but anatase phase is always observed. Also, even small amounts of TiF_4 precursor (1:9 F:Cl ratio) favors the production of anatase. Interestingly, a literature review of the synthesis of brookite in aqueous conditions reveals that amines (typically liquid ammonia) are almost exclusively present during the production of brookite.[136,234-236] Together with the results obtained under nonaqueous conditions, this suggests that amines stabilize the brookite phase, although the mechanism is not clear.

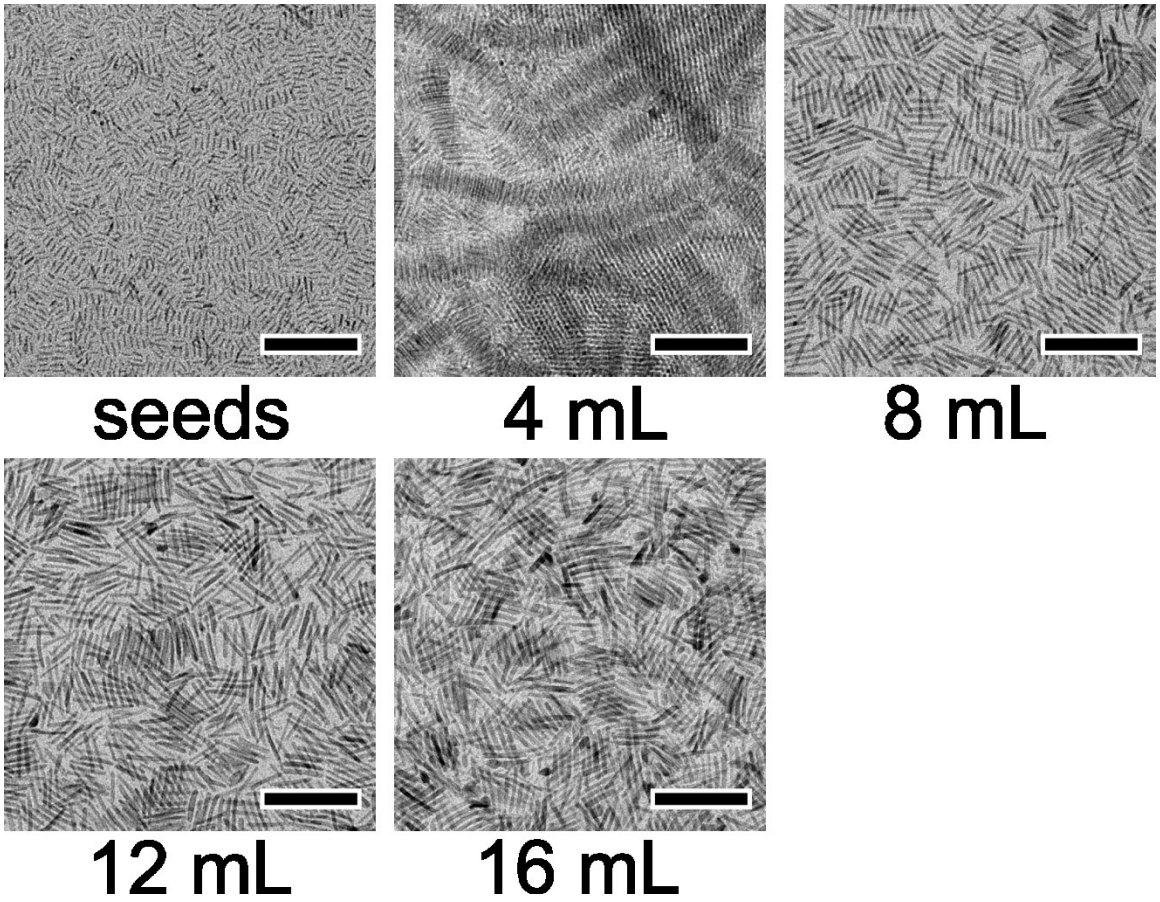

Figure 33: TEM images of aliquots taken from a seeded growth reaction using stock #1 (scale bars = 100nm)

Experimental XRD patterns are shown in Figure 34 for brookite nanorods formed using the seeded growth approach. The peak at θ = 30.9 observed in both experimental results is characteristic of brookite, and is not seen in either rutile or anatase. On the other hand, a simulation of the XRD pattern of brookite nanorods of similar widths and lengths calculated using the Debye equation is in poor agreement with the experimental result. This suggests two possibilities: 1) the nanorods are largely composed of anatase phase TiO_2 which has a fairly similar XRD pattern or 2) distortions such as strain or stress in the crystal structure modify the resulting pattern. The nanorods in this work and in the original report can be made highly mondisperse with several widths and lengths, all of which show similar XRD patterns.[147] HRTEM images of these nanorods are inconsistent with the symmetry requirements of the anatase phase, but rather suggest the brookite polymorph (see Figure 9).[147] Although the authors observed some nanorods which were composed of both anatase and brookite phases, pure phase brookite rods were only observed by HRTEM after a signficant volume of stock solution was added. Furthermore, HRTEM images revealed symmetry forbidden {1,0,0} reflections as a result of lattice plane bending in the nanorods, caused by lattice strain.[238,239] This result is confirmed by the clear bending of the nanorods along the long axis, as visible in Figure 32. In this case, the Debye function simulation confirms a more complex atomic arrangment is present at the nanoscale than observed in the bulk.

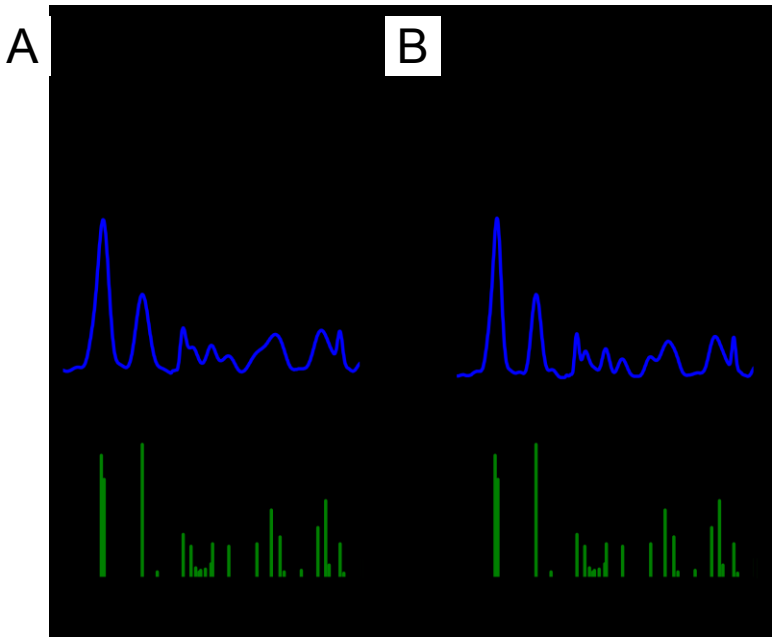

Figure 34: Experimental XRD patterns, simulation prepared using the Debye equation, and standard PDF patterns for brookite nanorods produced using seeded growth and A) stock solution #1 and B) stock solution #2.

Given the ability to prepare brookite nanorods with tunable morphology, there is an opportunity to probe the morphological dependence of the photocatalytic activity. To date, only the photoinduced electron transfer to electron receptors has been used to probe the photocatalytic activity of brookite nanorods, and in that case only a single sample of pure phase brookite was investigated.[238] In this report, we monitor the evolution of hydrogen from methanolic solutions in the presence of Pt under UV illumination. The nanocrystals are first treated with $NOBF_4$ in order to remove the surface ligands, which results in particles which are highly soluble in DMF and DMSO. The particles are then dried and ground to prepare for photocatalysis.

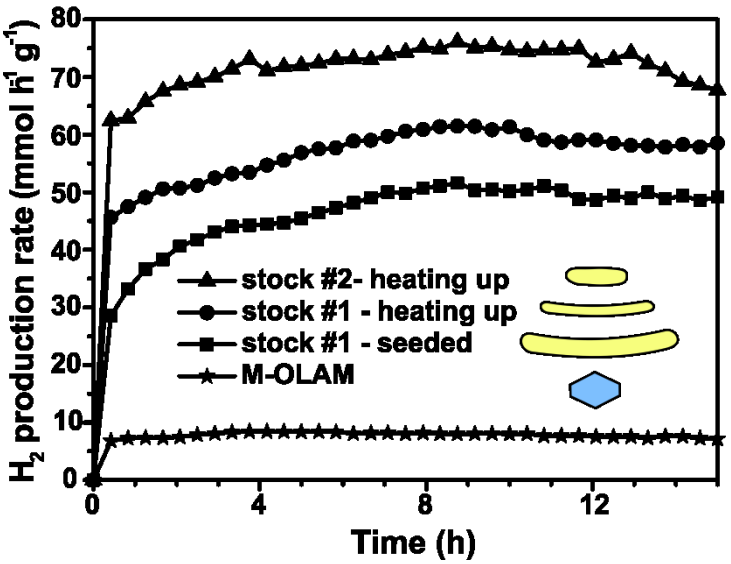

Figure 35: Hydrogen production rates from 1 wt. % Pt loaded samples of ligand-exchanged brookite nanorods and one sample of anatase under UV illumination in 1:1 mixtures of MeOH:H_2O. Triangle and circle are heating-up method with stock #2 and #1, respectively. Square is seeded growth, stock #1 and the star is M-OLAM from section 2.2.3.

Results of the photocatalytic reactions are shown in Figure 35. The first notable result is that all of the brookite nanorods have much higher activity than the most active sample of blue TiO_2 nanocrystals from section 2.2.3 (M-OLAM). This is an impressive result considering that the nanocrystals are treated identically and initially are coated with the same surfactants, although it does not rule out possible deleterious effects of oxygen vacancies or fluorine on the photocatalytic activity of M-OLAM. On the other hand, recent results indicate that oxygen vacancies and blue coloration may actually enhance photocatalytic activity under visible irradiation.[194] There is also a clear trend in the activity of the brookite nanorods, with smaller particle size leading to higher activity. This type

of behavior is often observed simply due to smaller particles having higher surface area, which leads to more reactions between photogenerated electrons and holes and substrate molecules on the surface.[79] In addition, interesting dynamics are observed in the photocatalytic reaction rate for brookite nanorods, with the rate gradually increasing over time and then leveling off over the course of many hours. Such variability is not expected, and may indicate unusual behavior in the metal deposition or other structural changes in the catalyst under illumination, and should be explored in more detail.

2.4.4 Conclusions

In this section, the synthesis of brookite nanorods is described through a literature method and a new heating up approach. The nanorods are shown to be highly photocatalytically active for the evolution of hydrogen from methanolic solutions in the presence of platinum. To further explore the photocatalytic activity, samples with a larger range of sizes and aspect ratios should be studied to properly understand the influence of particle size and shape on reactivity.

2.5 Future Work

The TiO_2 nanocrystals described in this work may act as model systems for a variety of additional studies. In photocatalysis, the influence of faceting on other reactions should be investigated, particularly energy related reactions such as CO_2 reduction and photoreforming in the presence of higher alcohols. The relative reactivity of the facets is certain to vary depending on the interactions of target substrates with the particle surface. Similarly, these materials may act as model systems for catalytic reactions, in which TiO_2 is known as an active support, participating in the reaction mechanism. This relates to studies currently underway on the surface science of nanocrystalline materials. Typically, single crystalline surface are utilized for surface science studies, but through precise control of faceting, nanocrystals could potentially act as substrates which can be directly linked to measurements performed under realistic operating conditions.

3. ZINC OXIDE NANOCRYSTALS[VII]

3.1 Synthesis of Uniform Zinc Oxide Building Blocks

3.1.1 Introduction

Zinc oxide (ZnO) is an ubiquitous material in scientific research, finding applications in light emitting diodes,[240] piezoelectrics,[241] field effect transistors,[242] transparent conducting electrodes,[243] heterogeneous catalysis,[244] and photocatalysis.[245] It belongs to the II-VI class of direct band gap semiconductors, along with materials such as HgTe, CdS, CdSe, CdTe, and ZnSe, which exhibit quantum confinement at small particle size and are commonly referred to as quantum dots. While many recent studies have focused on the properties of these other II-VI materials, particularly cadmium chalcogenides, size quantization effects were reported years earlier for aqueous colloids of ZnO by Koch, et al. in 1985, although only at very small particle size.[246]

Nevertheless, methods to synthesize ZnO building blocks with monodispersities comparable to typical quantum dots are currently lacking. Traditional methods, which rely on controlled hydrolysis of zinc sols, form ZnO nanocrystals which are excellent precursors for the production of field effect transistors and n-type layers in solar cells, but lack the uniformity in the individual ZnO units necessary for self-assembly.[247] Nonaqueous synthetic techniques

---

[VII] I would like to acknowledge the contributions of Abdul-Rahman Rajii, for assisting with the synthesis of ZnO nanocrystals during his time at Penn.

have produced materials with comparably higher monodispersity, primarily anisotropic in morphology, including rods, pyramids, cones and plates.[46,248-252] Peng, et al. demonstrated the first synthesis of highly monodisperse spherical ZnO nanocrystals, but their self assembly has not been described.[253]

There are several areas of intense study concerning ZnO nanomaterials. One is in the field of dilute magnetic semiconductors, which are semiconductors doped with magnetic atoms, which has been shown to induce room temperature ferromagnetism in certain systems, including ZnO.[254,255] While these results are often controversial, such materials may be the building blocks of future devices based on spintronics.[254,255] Another is in the production of UV lasing media. ZnO has a large exciton binding energy (60 meV), which causes an enhancement of the radiative transition rate in the UV.[256] There is a great demand for efficient UV lasers for optoelectronic devices.

In this work is described the synthesis of near-spherical ZnO building blocks. The synthetic procedure is amenable to doping, allowing for incorporation of Co into the wurtzite matrix of ZnO. In addition, we observe that the optical properties of the materials can vary depending on the reaction conditions.

3.1.2 Experimental

Chemicals. All chemicals are used as received. Zinc acetate dihydrate is purchased from Ricca Chemical. Zinc acetylacetonate, trioctylamine (TOA) and oleic acid (OLAC) are purchased from Aldrich. 1,2-dodecanediol (1,2-DDIOL) is

purchased from TCI America. Zinc stearate, cobalt(II) acetate, 1-octadecene (1-ODE), 1-octadecanol, toluene, 2-propanol, and hexanes are purchased from Acros Organics.

Synthesis I. All reactions are performed using standard Schlenk line techniques. In a 125 mL flask, 2 mmol of metal precursor (if doped, a mixture of zinc and cobalt acetate), 4 mmol of OLAC, 10 mmol of 1,2-DDIOL (or 1-ODOL), 10 mL TOA and 10 mL of 1-ODE are combined and heated to 120°C under vacuum, creating a colorless, transparent solution. After 1 hour of degassing, the flask is filled with nitrogen atmosphere and heated to 280°C. At 280°C, the reaction turns yellow in color and gas is evolved violently, indicating the nucleation of ZnO nanocrystals. After 1 hour at 280°C, the reaction is cooled to room temperature. Reaction is washed with acetone and dispersed in hexanes.

Synthesis II. All reactions are performed using standard Schlenk line techniques. In a 125 mL flask, 2 mmol of zinc precursor, 4 mmol of OLAC (OLAC excluded when using zinc stearate), 10 mmol of 1,2-DDIOL, and 25 mL of 1-ODE are combined and heated to 120°C under vacuum, creating a colorless, transparent solution. After 1 hour of degassing, the flask is filled with nitrogen atmosphere and heated to 300°C. At 280°C, the reaction turns yellow in color and gas is evolved violently, indicating the nucleation of ZnO nanocrystals. After 1 hour at 300°C, the reaction is cooled to room temperature. Reaction is washed with 2-propanol and dispersed in hexanes.

Characterization.

Transmission electron microscopy (TEM) images were recorded using a JEOL JEM1400 TEM equipped with a SC1000 ORIUS CCD camera operating at 120 kV. High-resolution TEM (HRTEM) images were recorded on a JEOL 2010F operating at 200kV. Samples were prepared by drop-casting a dispersion of NCs in toluene or hexanes on a 300 mesh carbon-coated copper TEM grid followed by drying at 50 °C under vacuum. All X-ray diffraction (XRD) patterns were recorded on a Rigaku Smartlab diffractometer equipped with a Cu K_α source. UV-Vis-NIR spectra were recorded on a Varian Cary 5000 spectrometer. Photoluminescence spectra were recorded on a Jobin Yvon Fluorolog 3.

3.1.3 Results and Discussion

Zinc oxide nanocrystals are produced using original nonaqueous surfactant assisted syntheses. Both described synthetic methods proceeds through a heating-up method which begins by dissolving a metal-organic zinc precursor (zinc acetate dihydrate or zinc acetylacetonate) in the presence of a stoichiometric amount of OLAC (1:2 Zn:OLAC) and excess 1,2-DDIOL. Then the reaction is degassed to remove water and other volatile species and is quickly heated to either 280 or 300°C. The degassed solution is completely transparent, indicating dissolution of the zinc precursor. Upon heating, a clear color change from transparent to yellow is observed at approximately 280°C, along with violent bumping of the reaction solution, indicating the onset of nucleation.

The reaction is presumed to occur through a alcoholysis type reaction as demonstrated previously in the synthesis of ZnO using monoalcohols.[180] Interestingly, the reaction rate is observed to be much faster in the presence of a monoalcohol, relative to the diol species. As shown in figure 1, under identical reaction conditions, nanocrystals produced using 1-ODOL are significantly larger and non-spherical post-synthesis and nucleate at much lower temperature (200°C) than in the presence of 1,2-DDIOL. This may indicate that the diol helps to direct the particle shape and size, by acting as a bidentate ligand, and is not as reactive with the zinc carboxylate species.

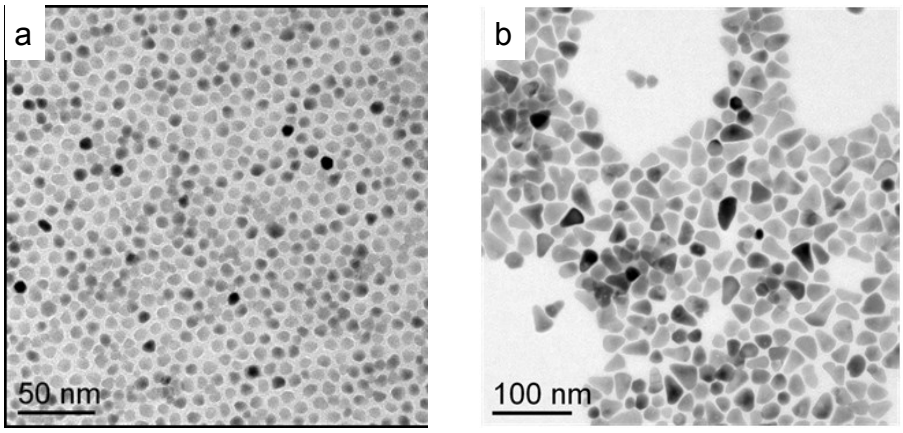

Figure 36: ZnO nanocrystals produced using synthesis I, using a) 1,2-DDIOL and b) using 1-octadecanol.

The resulting nanocrystals are 9 nm with a roughly 14% dispersion in size and crystallize in the hexagonal wurtzite crystal structure (Figure 37). Addition of cobalt acetate to the reaction mixture (10% Co) results in cobalt doped ZnO nanocrystals, as depicted in Figure 37. Incorporation of Co results in green

coloration due to the d-d transitions of tetrahedrally coordinated Co in the ZnO wurtzite lattice. The three characteristic peaks of the $^4T_1(P) \rightarrow {}^4A_2(F)$ transition of tetrahedrally coordinated cobalt(II) are observed in the absorbance spectrum (Figure 37c) of the Co doped nanocrystals, indicating successful substitutional doping of ZnO with Co(II).[257,258] Addition of Co(II) has minimal change in the morphology of the ZnO nanocrystals, as seen in the TEM images and X-ray diffraction patterns (Figure 37 a,b,e). This is most likely a result of the two atoms being isovalent and having nearly identical ionic radii under tetrahedral coordination.[255]

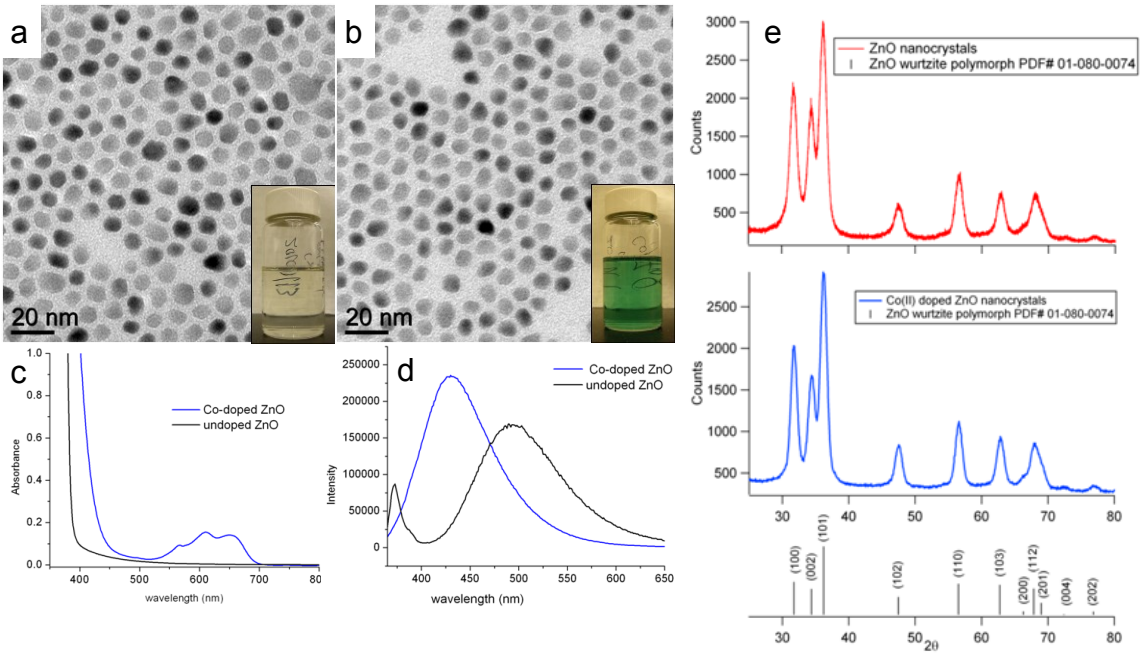

Figure 37: TEM images of a) undoped and b) Co-doped ZnO nanocrystals with insets showing photographs of the particle solutions. c) Absorbance and d) photoluminesence from ZnO nanocrystal solutions and e) WAXS patterns of undoped and doped ZnO nanocrystals.

Addition of Co also affects the photoluminescence spectrum of the ZnO nanocrystals. Using synthesis method I, undoped nanocrystals have two emission bands, one from bandgap emission in the UV (λ_{max} = 373 nm), and one in the green region of the spectrum (λ_{max} = 498 nm) referred to as "trap emission," which is commonly seen in nanocrystalline ZnO and is due to the presence of oxygen vacancies.[259,260] After cobalt doping, only a single photoluminescence peak was observed upon bandgap excitation, which is intermediate between the two emissions (λ_{max} = 430 nm). Previous studies have indicated quenching upon doping with Co(II), due to the presence of deep traps.[258] The observation of photoluminescence in our samples is not currently understood, but may indicate higher crystallinity in the samples described here relative to previous materials.

A second similar synthetic approach was developed which only utilizes 1-ODE as a solvent and slightly higher temperature (300°C). The resulting nanocrystals are much smaller, 5 nm in diameter with a 10% size dispersion. Despite the marginal difference in reaction conditions, the optical properties of these nanocrystals are different than as described above. While, the bandgap of the nanocrystals is roughly the same, only UV emission (λ_{max} = 365 nm) is observed from these ZnO nanocrystals. Pure UV emission is observed in larger ZnO nanostructures, such as wires, and "trap emission" is typically found to decrease in intensity with larger particle size.[261,262] "Trap emission" is commonly

thought to result from the recombination of singly ionized oxygen vacancies with photoexcited holes, and studies have correlated oxygen vacancy concentration to visible light emission.[260] On the other hand, the role of the surface is extremely important, with ligands such as oleic acid being found to affect the photoluminescence.[260,263] In one case, addition of oleic acid during the synthesis of ZnO in water was found to allow promote blue emission with high quantum yield in small particles, where the blue emission was attributed to the interface states of ZnO and the carboxylate.[264]

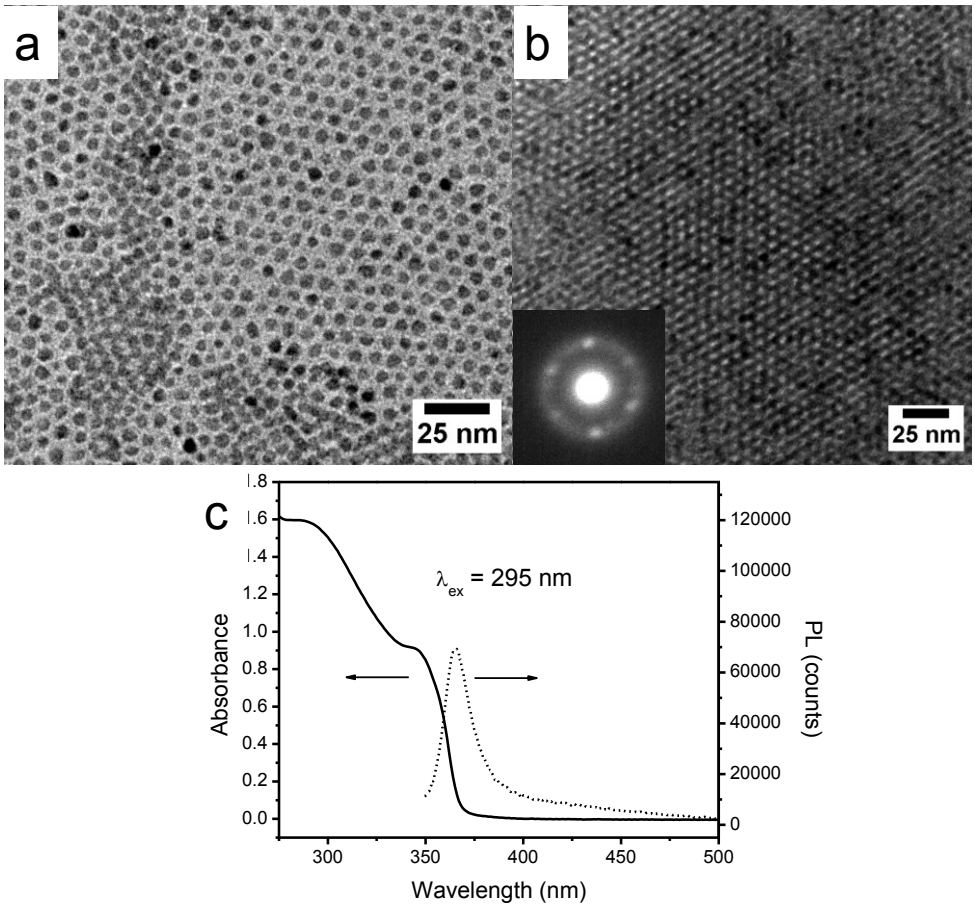

Figure 38: TEM images of ZnO nanocrystals produced using synthetic method II a) as a monolayer and b) assembled into a hexagonally close packed superlattice, inset shows electron diffraction pattern indicating hexagonal packing. c) Absorbance and photoluminescence spectra of ZnO nanocrystals synthesized using synthetic method II dispersed in hexanes.

In the current work, the differences observed between synthetic method I and II are possibly attributable to the reaction temperature. At higher temperature, oxygen vacancies may be "annealed out" of the nanocrystals, which may not be possible at lower temperature. Many authors have argued that recrystallization of nanocrystals occurs in solution, which acts as a mechanism to mend and fill defect sites.[265,266] Better control reactions should be conducted to confirm this hypothesis, such as varying the reaction temperature under a single set of reaction conditions. Also, the effect of excess surfactant should be further explored, as the interaction of ligands with ZnO have been shown to influence the photoluminescence.

3.1.4 Conclusions and Future Work

In this work, two unique methods to synthesize ZnO nanocrystals are described. The resulting nanocrystals are fairly monodisperse and could act as transparent n-type building blocks for self-assembled structures. The synthetic strategy is shown to be amenable to doping with Co(II) into the wurtzite ZnO lattice. Doping is also shown to influence the emission properties of the nanocrystals. Nanocrystals synthesized at high temperature are shown to emit

only UV light, while at those synthesized at lower temperature are shown to emit both UV and green light, indicating the presence of oxygen vacancies. Further work is needed to confirm the source of the differences in optical properties.

4. DOPED CADMIUM OXIDE NANOCRYSTALS

4.1 Shape Directed Plasmonic Response in Cadmium Based TCOs[VIII]

4.1.1 Introduction

The influence of particle shape on the plasmonic response and local field strength is well documented in metallic nanoparticles.[267] Morphologies such as rods, plates, and octahedra are readily synthesized and exhibit drastically different extinction spectra than spherical particles.[268] Despite this fact, the influence of shape on the optical properties of plasmonic semiconductor nanocrystals, in which free electrons result from heavy doping, has not been demonstrated. Here, we report the first observation of plasmonic resonance in indium doped cadmium oxide (ICO) nanocrystals, which exhibit the highest quality factors reported for semiconductor nanocrystals. Furthermore, we are able to independently control the shape and free electron concentration in ICO nanocrystals, demonstrating for the first time the influence of shape on the optical response of a plasmonic semiconductor. The highly uniform particles may be self-assembled into ordered single component and binary superlattices,

[VIII] This work would not have been possible without help from Taejong Paik, for collecting X-ray scattering and electron microscopy data, and performing self-assembly, Dahlia R. Klein, for assistance with synthesis and optical measurements, Gururaj Naik and Prof. Alexandra Boltasseva for analysis of spectroscopic ellipsometry and extraction of optical constants, and Humeyra Caglayan for completing FDTD simulations of particle scattering.

demonstrating a new class of tunable low-loss plasmonic building blocks for 3D-metamaterials.

Strong resonances which appear at optical frequencies for metal nanoparticles result from the resonant oscillation of free electrons on the surface of the particles, and are referred to as localized surface plasmon resonances (LSPRs). By altering the shape of the metallic particles, one can sensitively manipulate the observed resonant frequencies throughout the UV and visible and even into the NIR.[267-269] Highly anisotropic shapes, such as rods or plates, display multiple modes, while sharply faceted shapes are highly desirable due to the large field enhancements observed at tips and edges.[268,270,271] The focusing properties of plasmonic particles have been harnessed to enable a number of new technologies and sensitive measurement tools, such as surface enhanced Raman spectroscopy (SERS),[272] LSPR/SPR sensing,[273,274] photothermal therapy (PTT),[275,276] and plasmon-enhanced fluorescence.[277-279]

A series of recent papers have reported tunable LSPR at NIR and mid-IR frequencies resulting from semiconductor nanocrystals.[108,111,116,280,281] A plasmonic resonance is observed upon introduction of sufficient free carriers into the nanocrystals, either as a result of atomic vacancies or through doping with aliovalent cations. The LSPR frequency is dependent on the plasma frequency (ω_p) of the material, which is determined by materials properties such as carrier concentration and carrier mobility.[282] Unlike in the case of metals in which ω_p is

typically considered an intrinsic property of the material, through adjustment of dopant concentrations, ω_p can be readily tuned in semiconductors.[282] This opens the possibility of producing low-loss plasmonic nanocrystals with tunable LSPR frequency to substitute for metals, which typically have high losses in the NIR and mid-IR.[283] Copper based chalcogenides and indium tin oxide (ITO) have arguably been the most heavily studied systems,[108,280] and $Cu_{2-x}Se$ have already been proven effective for applications such as photothermal therapy.[284] On the other hand, poor particle uniformity and the inability to manipulate both particle shape and doping concentration independently has prohibited the correlation of particle morphology with the optical response, although some researchers have made strides towards this goal.[285,286]

As expected, all of the semiconducting nanocrystals recently found to support LSPR in the NIR are known to form highly conductive thin films. Two of these systems, ITO and aluminum doped zinc oxide (AZO), belong to the well-known family of d^{10} metal based transparent conducting oxides (TCOs), which are technologically important for applications in photovoltaics and displays.[108,111] There has been a resurgence of interest in cadmium oxide (also d^{10}) based TCO films, which were previously highlighted as having excellent TCO characteristics.[98,99,287,288] Highly transparent indium doped cadmium oxide (ICO) thin films may be produced with conductivities 2 to 5 times higher than that of commercial ITO films and near metallic n-type carrier densities (10^{21} cm^{-3}).[288] In

addition, tin doped cadmium oxide (SCO) films were recently prepared with the highest electrical conductivities and carrier mobilities of any TCO.[99] Together with the cubic rock salt crystal lattice, CdO has served as an excellent platform with which to sensitively test and model the influence of dopants, also including Sn, Ga, Y, and Sc, on the functional properties of high performing TCOs.[289,290] Highly transparent and electrically conductive TCOs have been introduced as a category of low-loss plasmonic building blocks, making CdO-based materials a promising, yet unexplored, system.[291]

In this work, we report the first observation of tunable LSPR in monodisperse doped cadmium oxide nanocrystals with both spherical and octahedral geometry, prepared through high temperature surfactant-assisted synthesis. The plasmonic resonance is tunable from 1.8 μm to 3.5 μm with increasing indium or tin concentration and the morphology of the nanocrystals is shown to influence the optical response. We report the highest quality factors for plasmonic semiconductor nanocrystals of spherical morphology reported to date. Furthermore, the ability to independently control the particle shape and doping concentration in highly uniform nanocrystals allows for the optical response to be correlated with the particle morphology. The high uniformity also enables self assembly of the particles, forming single component and binary superlattices in which the interparticle distance between plasmonic resonators is prescribed by the assembly.

4.1.2 Experimental

All syntheses are performed using standard Schlenk line techniques under nitrogen atmosphere.

Chemicals.

The following chemicals are used as received without further purification. Cadmium(II) acetylacetonate, cadmium(II) acetate, cadmium(II) oxide, indium(III) acetate, tin(IV) acetate, and 1-octadecene (90%) (1-ODE) are purchased from Acros Organics. Oleic acid (OLAC, 90%) is purchased from Sigma Aldrich. Anhydrous solvents were purchased from Sigma Aldrich or dried using standard methods.

Synthesis of spherical ICO NCs.

In a 125 mL flask, 1 mmol of total metal content (e.g. for 5% ICO, 0.95 mmol cadmium(II) acetylacetonate and 0.05 mmol indium(III) acetate), 3-5 mmol OLAC, and 30 mL of 1-ODE are combined and evacuated at 120°C for 1 hour. The reaction is heated then heated quickly to reflux (~320°C). Within 30 min, the reaction turns brown or dark green in color, indicating the nucleation of doped CdO nanocrystals. 30 min after the initial color change, the reaction is removed from heat and quickly cooled to room temperature with an air gun.

Synthesis of octahedral ICO NCs.

In a 125 mL flask, 1 mmol of total metal content, 3 mmol OLAC, and 30 mL of 1-ODE are combined and evacuated at 120°C for 1 hour. The reaction is

then placed under nitrogen atmosphere and quickly heated to 300°C. Within 40 min, the reaction turns yellowish brown in color, indicating particle nucleation. 30 min after the initial color change, the reaction is removed from heat and quickly cooled to room temperature with an air gun.

Workup.

All nanocrystal solutions are transferred air-free to a glovebox and washed under inert atmosphere. The solutions are initially washed with 2-propanol, recovered with centrifugation at 8000 rpm, resuspended in toluene and then washed again with 2-propanol and centrifuged. For smaller particles (<15 nm), the solids are suspended in hexanes and centrifugation at 3000 rpm for 2 minutes is used to remove any large aggregates. For nanocrystals with larger particle size (>15 nm), the material is only dispersible in hexanes or toluene solutions, and will settle over time.

Characterization.

Transmission electron microscopy (TEM) images were recorded using a JEOL JEM1400 TEM equipped with a SC1000 ORIUS CCD camera operating at 120 kV. High-resolution TEM (HRTEM) images were recorded on a JEOL 2010F operating at 200kV. Samples were prepared by drop-casting a dispersion of NCs in toluene or hexanes on a 300 mesh carbon-coated copper TEM grid followed by drying at 50 °C under vacuum. Scanning electron microscopy (SEM) images were recorded on a JEOL JSM7500F. Wide-angle X-ray scattering (WAXS)

patterns were recorded on a Rigaku Smartlab diffractometer equipped with a Cu K_α source. Small-angle X-ray scattering (SAXS) patterns were recorded at the Multi-Angle X-ray Scattering Facility at the University of Pennsylvania. All X-ray scattering patterns were recorded in transmission mode. For solution measurements, NCs were placed as highly concentrated toluene solutions into 1.0 mm glass capillaries. For samples measured in polymer films, 0.5 mL of 100 mg/mL polyvinyl butyral (Butvar-98) was mixed with a chloroform solution of NCs (0.5 mL) solution to arrive at 10 wt. % NCs in polymer. This solution was dropcast onto a glass slide and slowly dried until solid, at which point a thin polymer film can be removed from the slide surface in one piece. UV-Vis-NIR spectra were recorded on a Varian Cary 5000 spectrometer. Infrared (IR) spectra were recorded on a Thermo-Fisher Continuμm FT-IR system in transmission mode using a Harrick demountable liquid cell. Solutions for ICP-OES were prepared by drying 20 μL of hexanes solutions into a glass tube, dissolving with concentrated nitric acid, and diluting with ultrapure water.

X-ray Scattering Simulation.

The q-dependent powder X-ray diffraction intensity, I(q), is calculated using the Debye equation as described previously and detailed in section 2.2.2.[27]

4.1.3 Results and Discussion

ICO nanocrystals are produced through a high temperature surfactant assisted approach.[292] Briefly, a mixture of cadmium(II) acetylacetonate and the

dopant metal acetate salt (indium(III) acetate or tin(IV) acetate) which totals to 1 mmol of metal content are mixed with 3-5 mmol of oleic acid (OLAC) and 30 mL of 1-octadecene (1-ODE). After degassing at 120 °C for 1 hour, the reaction is quickly heated to 300 – 315 °C. Within 10 – 30 min at high temperature, thermal decomposition of the formed cadmium and indium oleate complexes occurs. After 30 min – 1 hour of growth at high temperature, the nanocrystals are quickly cooled to RT. It is worth noting that other cadmium sources, including cadmium(II) oxide and acetate may be substituted for the acetylacetonate, yielding similar results. This synthesis has implications for the synthesis of cadmium chalcogenide quantum dots, in which Cd precursors, particularly CdO, are often heated in the presence of OLAC at high temperature to form cadmium oleate prior to the introduction of chalcogenide precursor.[293] Any color change resulting from prolonged heating of such solutions at sufficient temperature signals the production of CdO nanocrystals, although Cd metal may act as an intermediary, as reported previously.[294]

In Figure 39, transmission electron microscopy (TEM) images of ICO nanocrystals are shown, illustrating the control of shape and high level of monodispersity achievable with the given system. The morphology of the nanocrystals is readily tuned through modification of the reaction temperature and oleic acid (OLAC) concentration. Large octahedral nanocrystals are formed at 300°C, and by adjusting the oleic acid concentration from 2 mmol to 4 mmol,

the size may be tuned (Figure 39 a, b, c). Refluxing the reaction solution at roughly 315 °C results in much smaller, spherical nanocrystals, the size of which is also tunable depending on oleic acid concentration (Figure 39 d, e). These results can easily be interpreted based on previous mechanistic studies, wherein higher reaction temperatures results in faster thermal decomposition, yielding more initial nuclei and thus a larger number of smaller sized crystallites.[295] Tin doped cadmium oxide NCs may also be produced using this method, demonstrating the generality of the method (Figure 40).

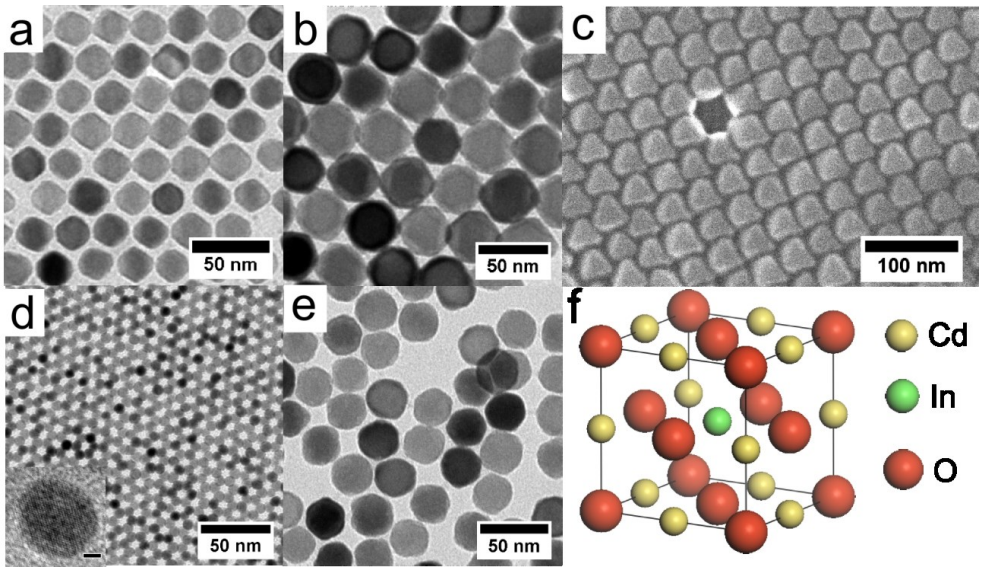

Figure 39: TEM images of octahedral ICO nanocrystals produced at 300 °C using a) 4 mmol and b) 3 mmol OLAC and SEM image of sample shown in b). TEM image of spherical nanocrystals produced at reflux using d) 5 mmol and e) 3 mmol OLAC. f) The unit cell of rock-salt type indium doped cadmium oxide (ICO).

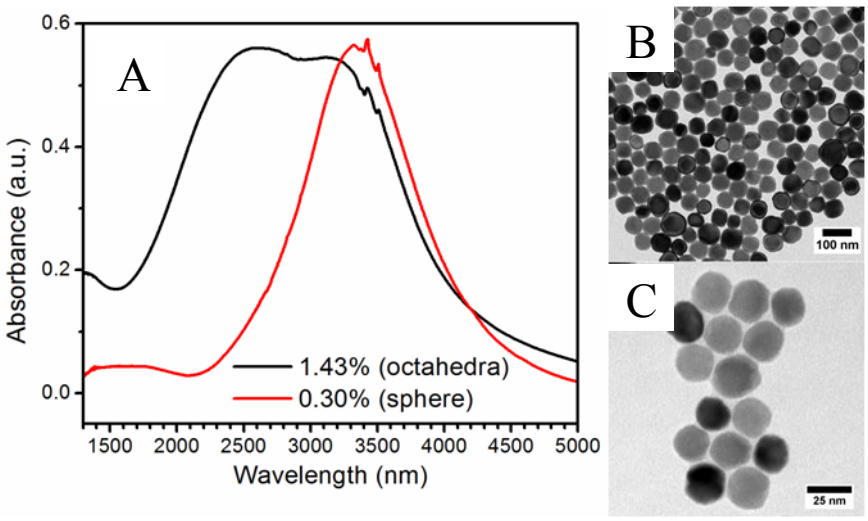

Figure 40: Plasmonic optical response (A), and TEM images (B, C) of tin doped cadmium oxide nanocrystals with octahedral and spherical morphology.

The hexagonal cross section of the ICO octahedra could easily be interpreted as resulting from hexagonal plate or prism. To confirm the octahedral morphology, TEM tilt experiments were undertaken. Figure 41 shows a collection of octahedra lying on their face, displaying a hexagonal cross section and the effect of tilting the sample. Upon tilting in the upwards, the nanocrystals take on a diamond-like projection clearly indicating the octahedral geometry. In contrast, tilting downwards results in a square projection, in which the nanocrystals are being viewed directly down the point of the octahedra. Together with SEM imaging (Figure 39 c), the octahedral structure with sharp tips is confirmed.

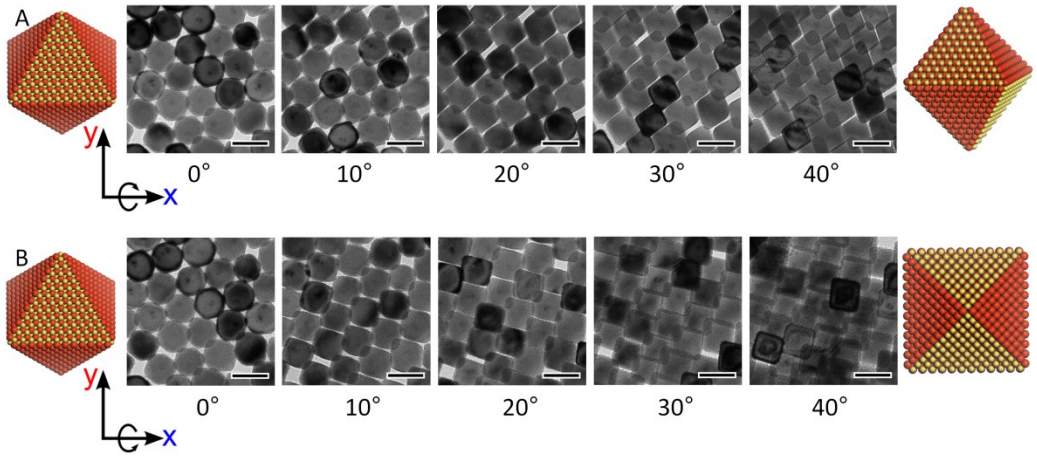

Figure 41: TEM tilt series confirming the octahedral geometry of the ICO nanocrystals, shown for A) tilting in the positive x direction and B) tilting in the negative x direction.

HRTEM data indicate the NCs are single-crystalline, and adopt the $Fm\bar{3}m$ rock salt crystal structure typical of cadmium oxide crystallites (Figure 39 d inset). The crystal structure and monodispersity observed by TEM is confirmed through X-ray scattering studies, both small angle (SAXS) and wide angle (WAXS) in conjunction with a Debye function simulations (Figure 42). While TEM is an invaluable tool for the determination of sample morphology, statistically significant information is tedious to extract. X-ray scattering, in contrast, is a bulk measurement of nanocrystal structure, which is sensitive to particle morphology. In particular, SAXS is highly sensitive particle size distribution, WAXS is sensitive to interatomic spacings and crystal structure, while both are sensitive to particle morphology.[27] In combination with Debye function simulations which are calculated based on atomisitic models, the morphology determined by TEM can be confirmed through a bulk measurement of WAXS and SAXS for a uniformly

dispersed sample.[39,296] The X-ray fittings indicate that the octahedral nanocrystals are roughly 51.0 ± 3.6 nm in length (tip-to-tip), while the spherical nanocrystals are 8.0 ± 0.1 nm, in excellent agreement with measurements from TEM. Thus, we have produced highly uniform plasmonic NCs which may act as model systems to test the influence of particle shape on optical response.

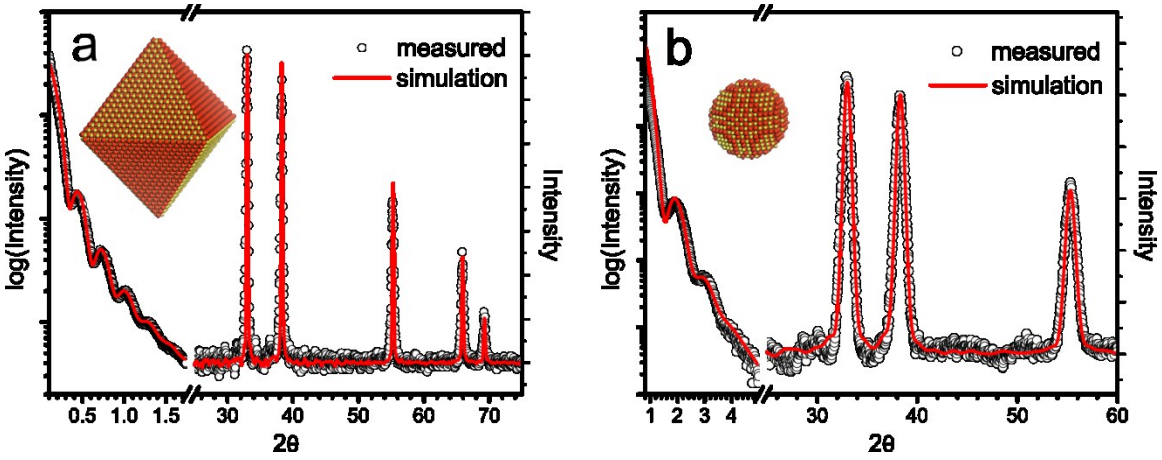

Figure 42: SAXS and WAXS patterns for a) 51 nm (tip-to-tip) octahedral ICO nanocrystals dispersed at 10 wt. % in polyvinyl butyral and b) 8 nm spherical ICO nanocrystals dispersed in CCl_4 and loaded into a glass capillary.

A strong plasmonic resonance is observed in the highly uniform ICO nanocrystals in the NIR range and the wavelength maximum of the plasmonic resonance (λ_{max}) is tunable from 1.8 μm to 3.5 μm depending on the indium concentration (Figure 43a, Figure 44). Cadmium and indium concentrations are determined by inductively coupled plasma-optical emission spectroscopy (ICP-OES) and are observed to correlate with the starting metal concentrations (

Table 4), although indium concentrations are always observed to be significantly higher than the starting concentration. The enrichment of indium in the nanocrystals may result from the formation of metallic cadmium aggregates or unreacted cadmium precursors residing in solution.

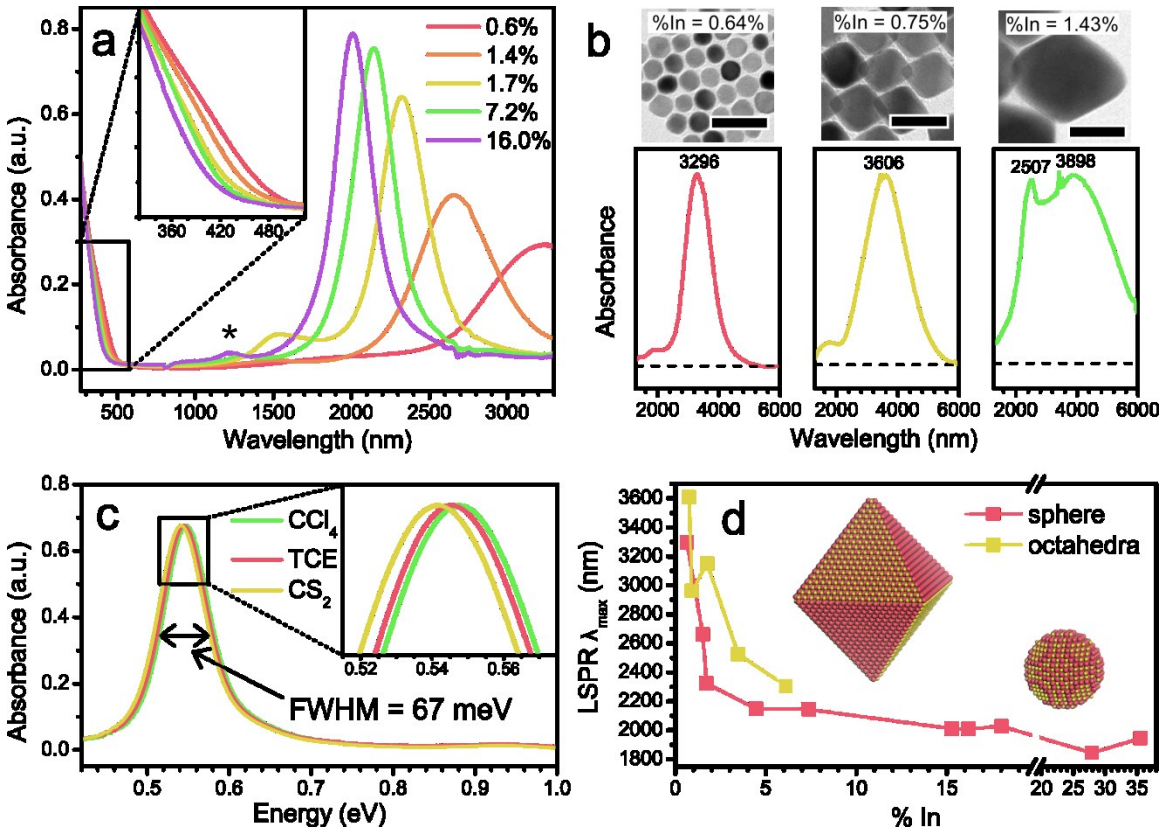

Figure 43: a) Solution phase spectra of ICO nanocrystals dispersed in CCl_4 for 5 levels of % atomic doping of In (inset shows the blue shift of the bandgap with increasing In content). b) Solution phase spectra of three shapes/sizes (spherical, small octahedral and large octahedral) of nanocrystals with similar levels of In doping, where the TEM image above each image corresponds to the sample measured optically (scale bar = 50 nm). c) Solution phase spectra of ICO nanocrystal sample dispersed in CCl_4, TCE, and CS_2, with inset indicating the wavelength shift. d) Plot of LSPR wavelength with increasing In content for octahedral and spherical nanocrystals.

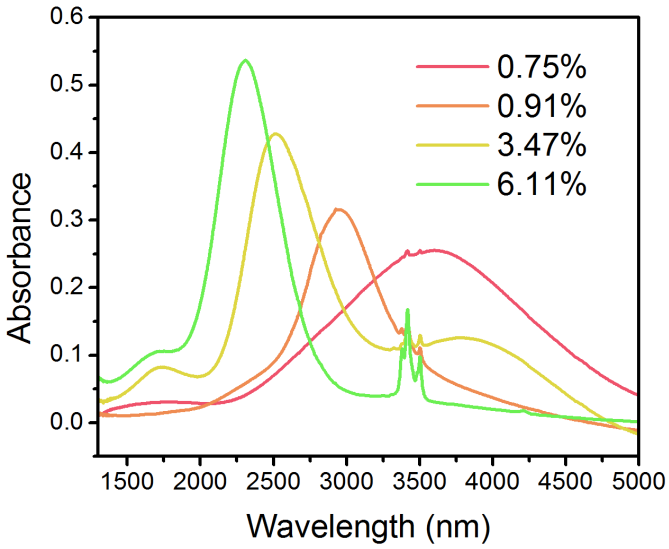

Figure 44: Optical absorbance of four samples of ICO octahedra with different concentrations of indium.

Shape	**Initial % In**	**Meas. % In**	**Dia. / tip-to-tip length (nm)**	**MW of ICO NC* (g/mol)**	**Conc. ICO NCs[l] (M)**	**λ_{max} (nm)**	**Abs at λ_{max}**	**ε at λ_{max} (M^{-1} cm^{-1})**
sphere	0.5	0.64	17.2	1.30×10^{7}	5.81×10^{-9}	3296	0.750	1.29×10^{8}
sphere	0.8	1.51	8.0	1.32×10^{6}	4.55×10^{-8}	2663	1.000	2.20×10^{7}
sphere	1	1.73	8.7	1.70×10^{6}	1.61×10^{-8}	2323	0.757	4.69×10^{7}
sphere	3	4.47	9.0	1.88×10^{6}	4.92×10^{-8}	2148	0.678	1.38×10^{7}
sphere	5	7.37	8.9	1.84×10^{6}	1.24×10^{-8}	2144	0.622	5.00×10^{7}
sphere	8	15.29	7.5	1.10×10^{6}	3.06×10^{-8}	2011	0.736	2.41×10^{7}
sphere	10	16.20	11.3	3.76×10^{6}	4.57×10^{-9}	2009	0.621	1.36×10^{8}
sphere	15	18.04	10.7	3.15×10^{6}	6.24×10^{-9}	2029	0.590	9.45×10^{7}
sphere	20	35.53	11.6	4.03×10^{6}	3.47×10^{-9}	1944	0.393	1.13×10^{8}
octah.	0.5	0.75	67.9	1.55×10^{8}	3.55×10^{-9}	3623•	0.254	1.43×10^{9}
octah.	0.8	0.91	50.9	6.53×10^{7}	9.35×10^{-10}	2929	0.549	5.87×10^{8}
octah.	1	1.75	58.0	9.66×10^{7}	6.30×10^{-10}	2611	0.590	9.36×10^{8}
octah.	3	3.47	57.3	9.32×10^{7}	2.51×10^{-10}	2519	0.164	6.53×10^{8}
octah.	5	6.11	48.2	5.52×10^{7}	6.01×10^{-10}	2407	0.289	4.81×10^{8}
octah.	0.5	1.05	131.8	1.13×10^{9}	--	--	--	--
octah.	1	1.09	136.4	1.25×10^{9}	--	--	--	--

Table 4: Properties of ICO NCs determined by ICP and UV-Vis-NIR spectroscopy.

Measured %In is determined by ICP-OES, ε is the extinction coefficient, calculated as $\varepsilon = A/bc$, where A is the measured absorbance, b is the cuvette pathlength, and c is the conc. of nanocrystals. *MW is determined multiplying volume of the average NC (cm^3) by the density of CdO (8.15 g/cm^3) and Avogadro's number (6.022 x 10^{23}/mol). For sphere, $V = 4/3\,\pi r^3$, for the octahedra $V = \sqrt{2}/3\,a^3$, where a is the edge length and $b = \sqrt{3} * a$, where b is the tip-to-tip length. Edge length is directly measured by TEM. ‖This is the concentration of the nanocrystals when optical absorbance was measured. •Due to resonance wavelength, the optical absorbance of this sample was measured using a liquid cell with 0.05 cm pathlength in an FTIR spectrometer.

High doping concentrations are found to negatively affect the morphology of the nanocrystals, resulting in polydispersity or bimodal distributions of particle size. For octahedral nanocrystals, sharp tips become rounded and small particles are observed above a starting concentration of 5% (initial) In doping. At reflux, retain spherical morphology and high uniformity at initial indium concentrations up to 15%, at which point bimodal distributions are observed. Interestingly, the plasmonic resonance is observed to be much more sensitive to indium concentration at low doping levels in both spherical and octahedral particles (Figure 43d). At very high doping levels, electron trapping may begin to occur at In centers, lowering the free-electron concentration, as suggested in the case of ITO nanocrystals.[108]

Increasing indium concentration also results in an increase in the bandgap (inset of Figure 43a) referred to as a Burstein shift, which was previously noted in thin films, and is responsible for the high transparency of ICO films.[288,297] Intrinsic

CdO has a direct optical bandgap of 2.3 eV, which would make it unsuitable for TCO applications, but In incorporation significantly shifts the bandgap to the near UV. As CdO is a direct bandgap material, a plot of $(\alpha E)^2$ vs. E near the band edge should result in a linear plot for which the x-intercept is the bandgap energy. Figure 45 depicts the $(\alpha E)^2$ vs. E plots for several ICO nanocrystal samples, indicating the shift of bandgap with increasing In concentration. The bandgap widens from 2.97 eV to 3.34 eV with increasing In concentration.

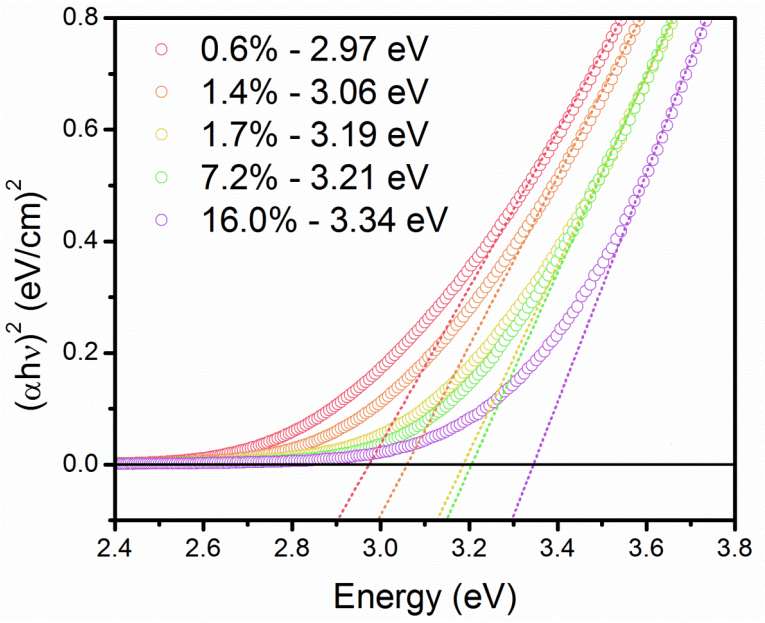

Figure 45: Plots of $(\alpha h\nu)^2$ vs. photon energy (eV) for 5 samples of spherical ICO NCs. Open circles are measured data, dotted lines are linear fits, and the legend shows the extracted direct bandgap energies.

The ability to synthesize ICO nanocrystals of two morphologies with high uniformity over the same concentration range allows for shape dependent optical properties to be unambiguously investigated. A clear shape dependence of the

optical response is apparent in the ICO nanocrystals, as depicted in Figure 43 b,d. Using the synthetic techniques described above, spherical nanocrystals 12 nm in diameter and two samples of octahedral nanocrystals 50 nm and 100 nm in length (tip-to-tip) are prepared with very similar atomic doping concentrations (0.64 – 1.43%). At the frequencies currently under study, even the largest particles are significantly sub-wavelength (< λ/40), meaning they are within the size region of the quasi-static limit and only dipolar coupling is expected to occur in the nanocrystals.[298] As a result, additional peaks and shoulders should not result from multipolar modes.

The resonance for the spherical nanocrystal at 3296 nm is very symmetrical, while the octahedra display a significantly redshifted λ_{max} relative to the sphere at 3606 nm and clear asymmetric broadening. The redshift in λ_{max} and asymmetric peak broadening is consistent for octahedral samples prepared at several wavelengths and doping concentrations, as depicted in Figure 43d and Figure 44. The large octahedra shows a dramatically different spectrum, with two peaks, one at 2507 nm, and one at 3898 nm. This dramatic spectral change is a clear demonstration of a shape effect on the plasmonic resonance.

For metal particles, shape effects on LSPRs are often confirmed through numerical simulations which require the optical constants of the material in question. While bulk values for metals are readily available, the permittivity of degenerately doped semiconductors is not as well studied and is highly

dependent on doping concentration. To circumvent this issue, spectroscopic ellipsometry is performed on spin-cast films of spherical ICO nanocrystals to extract approximate optical constants of bulk ICO using Bruggeman effective medium theory. These extracted constants are utilized to run FDTD simulations of the particle scattering. As shown in Figure 46, the simulation results predict the LSPRs of the 68 and 132 nm octahedra to be redshifted relative to the 12 nm sphere and significantly broader, as observed experimentally. Furthermore, to rule out the effect of size on the response, a 68 nm sphere is simulated to compare with the 68 nm octahedra. The 68 nm sphere is shown to have a similar response to the 12 nm sphere, and no redshifting of the peak occurs. Similarly for Au nanoparticles, the LSPR plasmon resonance is also redshifted in octahedra relative to spheres of similar size and when the size dependence of broadening has been described in spherical Au nanoparticles in the size region of the quasistatic limit, broadening actually increases with decreasing size due to electron surface scattering, contrary to what is observed here.[298,299] In conjunction with the simulation, the experimental demonstration of a plasmonic shape effect in a semiconductor nanocrystal is unequivocal.

One interesting, unexplained feature observed in all spherical samples of ICO is a small peak at significantly higher energy than the main LSPR, as marked by an asterisk in Figure 43a. The origin of this peak is currently unknown, as it should not be multipolar, but would not be expected from an isotropic

geometry. Indirect bandgap or localized atomic states are feasible, although the indirect bandgap is very weak in CdO and localized states are unlikely for d^{10} metals such as Cd and In, and would not be expected to shift with doping concentration, as observed here.

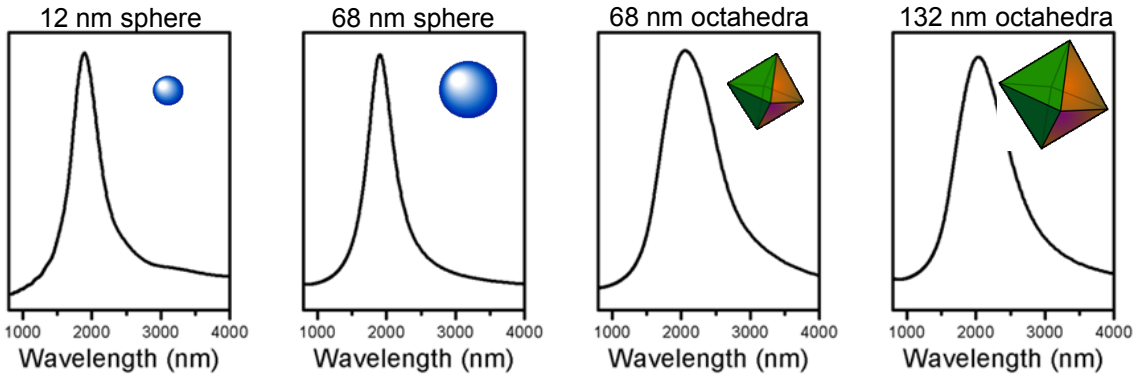

Figure 46: Calculated extinction coefficients simulated with FDTD using values of permittivity for ICO extracted using spectroscopic ellipsometry.

In order to ascertain whether monodisperse ICO nanocrystals could substitute for plasmonic metals in the NIR region, it is important to derive several metrics which are commonly used in the literature. First, is the quality factor, which is defined as the ratio of the plasmonic resonance energy to the peak linewidth.[300] A large quality factor is an indicator of high local field strength. The linewidth of the resonances reported in this work are quite sharp, which suggests that 1) few loss channels or non-radiative decay pathways are present and 2) little inhomogeneous broadening exists, due to the high uniformity of the samples, both in terms of morphology and dopant concentration.[300] The quality factors for the spherical ICO nanocrystals lie in the range of 3.5 to 8.2 (Table 5),

which far exceed the values of 1.6 and 3 previously reported for semiconductor nanocrystals $WO_{2.83}$ and $Cu_{2-x}S$, respectively and rival even the most monodisperse samples of Au and Ag nanocrystals.[116,281] The high quality factors exhibited by ICO nanocrystals make them promising materials as sensors in a unique wavelength range.

Initial % In	Measured % In	λ_{max} (nm)	Energy (eV)	Γ (eV)	Quality Factor
0.5	0.64	3296	0.376	0.106	3.55
0.8	1.51	2663	0.466	0.101	4.61
1	1.73	2323	0.534	0.081	6.62
3	4.47	2148	0.577	0.094	6.16
5	7.37	2144	0.578	0.082	7.02
8	15.29	2011	0.617	0.080	7.70
10	16.20	2009	0.617	0.085	7.26
15	18.04	2029	0.611	0.102	5.99
20	35.53	1944	0.638	0.131	4.88
10*	13.18	2265	0.547	0.067	8.15

Table 5: Table of optical information extracted from several samples of spherical ICO nanocrystals. Γ is the FWHM of the peak at the resonance wavelength. The quality factor is defined as $QF = \omega_{max}/\Gamma$, where ω_{max} is the photon energy at the LSPR maximum.

A second important parameter is the extinction coefficient, which is known to be much larger in plasmonic particles than in typical absorbers, justifying their use in photothermal therapy.[276] After the concentration of the cadmium and indium metal is determined in the nanocrystals by ICP-OES, the concentration of nanocrystals is calculated based on the appropriate atomistic model derived from TEM and X-ray modeling. By dividing the optical absorbance at λ_{max} by the cuvette path length and the concentration the molar extinction coefficient of the

plasmonic resonance is derived, which lies in the range of 0.1 – 1.4 x 10^8 M^{-1} cm^{-1} for spherical ICO and 0.5 – 1.4 x 10^9 M^{-1} cm^{-1} for the larger octahedral ICO. This large value of extinction coefficient is on the same order of magnitude as that of Au nanocrystals of similar particle size.[298,301]

Plasmonic resonances are also sensitive to local dielectric environment, which is exploited in surface plasmon resonance spectroscopy and sensing. In the quasistatic limit, a spherical Drude metal will have a LSPR at:

Equation 12
$$\omega_{LSPR}^2 = \frac{\omega_p^2}{\varepsilon_\infty + 2\varepsilon_a} - \Gamma^2 \quad ,$$

where ω_{LSPR} is the LSPR frequency, ω_p is the plasma frequency, ε_∞ is a constant offset, ε_a is the dielectric constant of the dispersing medium, and Γ is the damping constant.[302] From equation 1, it is apparent that as the dielectric constant of dispersing medium increases, the plasmonic resonance will redshift. This formula also defines the relationship between the LSPR frequency and the plasma frequency, as described previously. Figure 43c and Figure 47 show the shift in the plasmonic resonance with the refractive index (n) of the solvent. At optical frequencies, where the relative permeability (μ) of all materials is equal to 1, the refractive index is related to ε_a by the formula:

Equation 13
$$n = \sqrt{\varepsilon_a \mu_a} = \sqrt{\varepsilon_a} \quad .$$

So, the effect of the change in refractive index is also a change in the relative permittivity of the solvent. The nanocrystals display plasmonic sensitivity of 150 nm per refractive index unit (nm/RIU), similar to other recently reported

plasmonic semiconductors, as well as Au and Ag nanoparticles. When compared with traditional plasmonic materials, in each case ICO nanocrystals represent a sound substitute, with the added advantage of being tunable over a large frequency range.

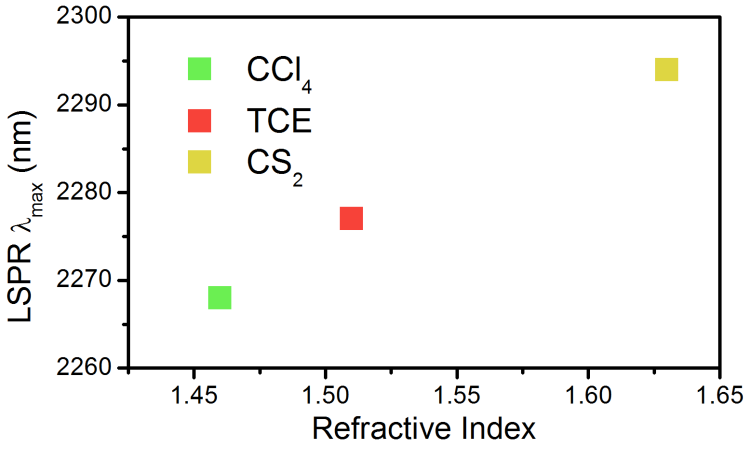

Figure 47: Plot of resonance wavelength vs. refractive index of solvent for a single sample dispersed in 3 different solvents.

The highly uniform ICO nanocrystals can be utilized as building blocks to form ordered self-assembled superlattices (Figure 48). All ordered films are produced using a liquid interfacial assembly technique described previously.[303] Octahedra of 51 nm length from tip-to-tip self assemble into ordered Minkowski-type superlattices, similar to as recently reported for Ag octahedra.[304] These oriented assemblies of octahedra have high packing densities and prescribed interparticle distances. In addition to forming single component assemblies, spherical ICO nanocrystals of 8 nm with a plasmonic resonance at 1975 nm have been self-assembled with 5 nm lead selenide (PbSe) quantum dots to form large

area AlB_2-type binary nanocrystal superlattices (BNSLs). BNSLs offer a platform in which the interaction between plasmonic particles can be readily tuned, depending on the structure of the BNSL and chemical composition of the building blocks. Given the number of known uniform nanocrystal building blocks and distinct BNSL structures, thousands of sub wavelength structures could be self-assembled from these ICO particles, each with its own unique interactions.

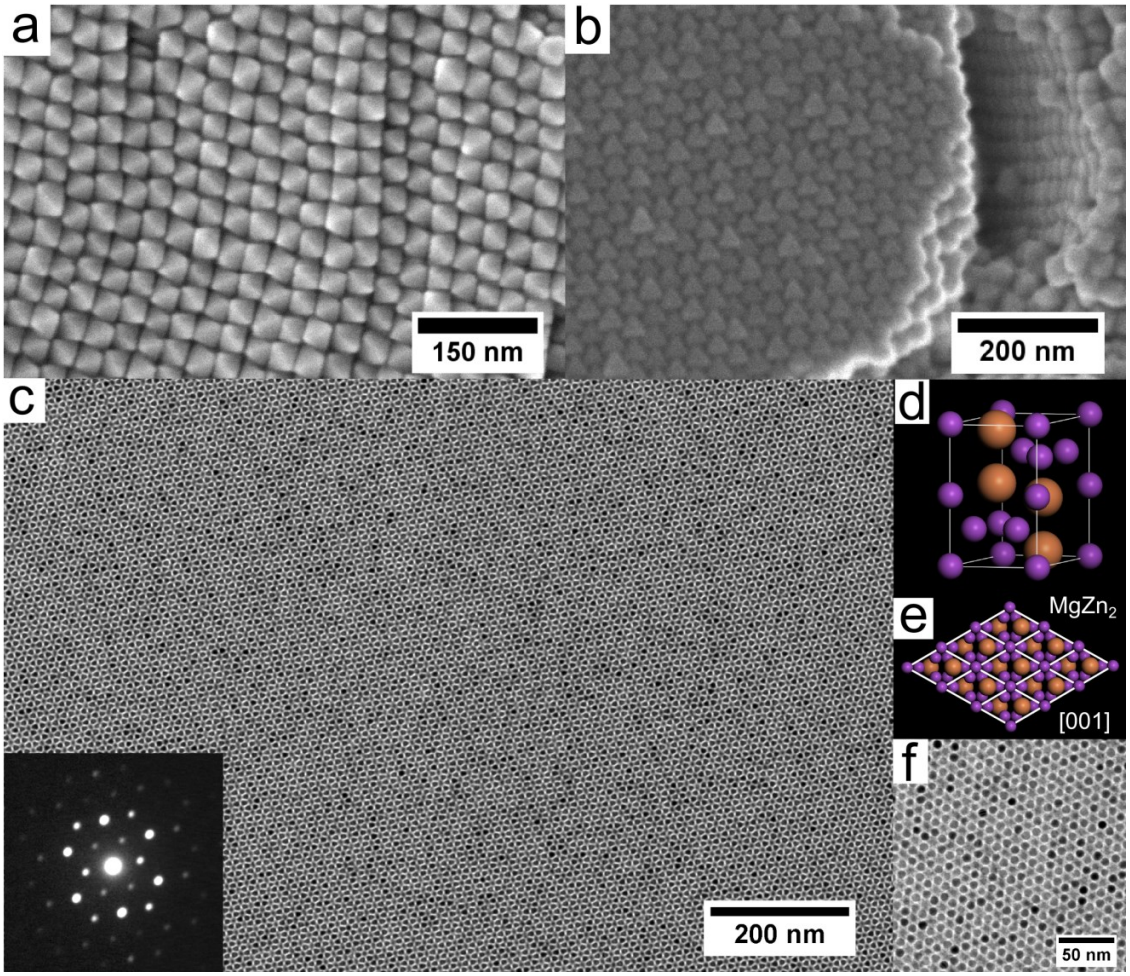

Figure 48: Self assembled structures formed at a liquid-air interface. a, b) SEM images of ICO octahedra, forming 3-D Minkowski-type superlattice structures. c) Long range [001] projection of

an $MgZn_2$-type BNSL of 8 nm ICO nanocrystals and 5 nm PbSe nanocrystals, inset shows electron diffraction pattern of BNSL. Depictions of the d) unit cell and e) [001] projection of the $MgZn_2$-type BNSL. e) Higher magnification TEM image of BNSL.

4.1.4 Conclusions

We have described the synthesis and optical properties of doped cadmium oxide nanocrystals with tunable morphology. The high monodispersity of the materials as confirmed by X-ray scattering allows for the influence of shape on the plasmonic response to be observed unequivocally. ICO nanocrystals possess the highest quality factors reported for plasmonic semiconductors and are comparable to traditional metals such as silver and gold. The high monodispersity of the spherical and octahedral nanocrystals allows for their self-assembly into 3-D superlattice structures with long range order. Spectroscopic ellipsometry of films of ICO nanocrystals reveal negative permittivity in the NIR, indicating strong coupling between the low-loss ICO nanocrystals and demonstrating their utility as a new class of building blocks for plasmonic metamaterials.

4.2 Tunable Metallic Thin Films from TCO Nanocrystal Precursors[IX]

4.2.1 Introduction

The study of metamaterials has led to the theoretical prediction and experimental demonstration of unique physical properties and functionalities such as negative refraction,[117] negative refractive index,[120,305] subdiffraction imaging,[119] and cloaking[117] at infrared and microwave frequencies. In the visible and NIR frequency range, where the impact of such devices is expected to be greatest, the noble metals gold and silver have been targeted as appropriate building blocks, due to having negative permittivity at these frequencies.[122] However, one major problem roadblock to the development of optical metamaterials is the optical losses (interband transitions) present in the noble metals at these frequencies.[122]

Degenerately doped semiconductors, particularly transparent conducting oxides (TCOs), have recently been introduced as low-loss substitutes for Au and Ag in the NIR frequency range for metamaterial applications in the NIR.[283,306] As outlined above in previous sections, the advantages of TCOs include the low-loss, as well as the tunability of the plasma frequency with doping concentration. A range of materials have been investigated as potential materials of interest, including AZO, gallium doped zinc oxide (GZO), and ITO, which have plasma

---

[IX] I would like to thank Gururaj Naik, and Alexandra Boltasseva for help in collecting data and extracting the optical constants of the films using spectroscopic ellipsometry.

frequencies tunable from 0.8 to 2 eV. Remarkably, a hyperbolic metamaterial containing layers of ZnO and AZO films, where AZO is the metallic component, has recently been prepared which shows negative refraction in the NIR and performs better than the same device prepared using gold, demonstrating the utility of such materials in the preparation of optical metamaterials.[122]

The majority of approaches to the preparation of metamaterials rely on a "top-down" approach in which small features are produced through photo- or electron beam-lithography.[123,307] While advances have been made, the requirement for significantly sub-wavelength features makes some designs untenable. "Bottom-up" approaches which rely on self-assembled gold and silver nanoparticles have also been proposed and experimentally demonstrated, potentially representing a more scalable route to metamaterials.[308-311] Similarly, TCO nanocrystals should be considered as potential building blocks with tunable response. In nanocrystalline form, materials targeted for NIR applications, such as ITO and AZO, have been demonstrated to show LSPRs in the NIR, and could act as low loss building blocks for metamaterials.[108,111]

In this work, we show that thin films can be constructed from ICO nanocrystals by simple spincasting procedure, which can be annealed to form conductive films. Spectroscopic ellipsometry performed on the annealed films reveals metallic response in the NIR and tunable plasma frequency depending on dopant concentration. Remarkably, we also observe that even the as-

prepared, non-conducting films, in which LSPRs continue to be observed, posses negative permittivity. The metallic-like optical response of these films is proposed to result from dipolar coupling between nanocrystals in the thin films.

4.2.2 Experimental

Spherical ICO nanocrystals are synthesized as described in section 4.1.3 starting with doping concentrations of 10, 15, and 20 % and are purified and stored under inert atmosphere. After purification, a portion of each solution was dried, and then redissolved in octane at 25 mg ICO/mL (*note this is mass of ICO determined by ICP-OES, not mass of nanocrystals). Films were produced using a Specialty Coating Systems G3P spincoater. Polished quartz windows from G. M. Associates were placed on the holder and a filtered portion of the concentrated ICO nanocrystal solution was dropped onto the surface until fully covered. The substrate was then spun at 800 rpm for 30 seconds, followed by 1000 rpm for 30 seconds.

Film Treatment.

Annealed samples were treated in a ULVAC MILA-5000 rapid thermal annealer in air. The temperature was increased at a rate of 10°C/second from room temperature to 350°C, and then was held for 10 min before cooling.

Characterization.

Infrared (IR) spectra were recorded on a Thermo-Fisher Continuμm FT-IR system. Transmission spectra are collected with a standard holder. Reflectance

spectra were measured on a Harrick variable angle Seagull accessory at 25° relative to normal, using a Thorlabs protected gold mirror as a reflectance standard. Solution phase spectra were recorded using a Harrick demountable liquid cell. Spectroscopic ellipsometry was performed using a J. A. Woollam M-2000 and V-VASE systems.

4.2.3 Results and Discussion

Thin films of ICO nanocrystals were prepared by spin coating concentrated nanocrystal solutions in octane onto quartz windows, resulting in 50-120 nm thick films which are highly transparent and slightly yellow in color. Figure 49a displays the NIR transmission spectra of the sample dispersed in CCl_4 and as deposited on the substrate. Upon deposition, a significant redshift is observed in the samples, which results from the coupling of the plasmonic particles, which is well documented in other plasmonic particle systems.[312,313] Sharp peaks are observed at 3000 cm^{-1} in the solution and as deposited, which result from C-H vibrations of the surfactant (oleic acid) on the particle surface.

Several methods were investigated to remove the surfactant from the surface of the ICO nanocrystals. Removing the surfactants without loss of structure and properties continues to be a hurdle for the application of nanocrystals in practical devices, particularly for electronics, and has received significant attention in recent years.[314] Ironically, it is the surfactants which enable the precise control over size and shape which also cause the particles to

be insulating and unable to interact with their environment. In the case of oxide nanocrystals, several methods have emerged for the effective removal of surfactants. One promising approach, pioneered by our group, has been the use of small reactive molecules, such as nitrosonium tetrafluoroborate ($NOBF_4$) and diazonium tetrafluoroborate salts.[142] While, the exact mechanism by which these molecule reacts is unknown, the oxidizing power of NO likely plays a role in the removal of the organic species, while the BF_4 group is retained on the particle surface, partially balancing the positively charged metal atoms which remain after surfactant removal.[142]

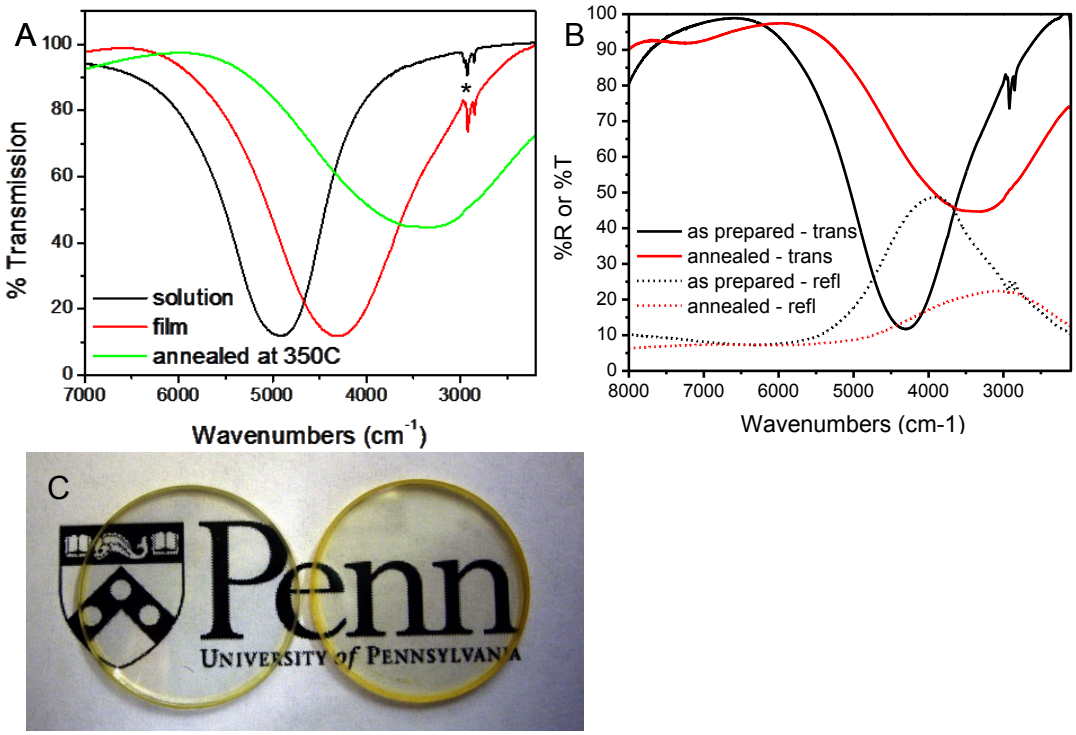

Figure 49: A) NIR/IR transmission spectra of 10% ICO nanocrystals dissolved in CCl_4 solution, as deposited on quartz, and after annealing. *indicates C-H vibrations from surfactants on particle

surfaces. B) NIR/IR transmission spectra and reflectance spectra for 10% ICO nanocrystals as deposited on quartz, and after annealing. C) Photograph of ICO nanocrystal films before (left) and after (right) annealing.

For this work several ligand exchange techniques were attempted which have been used successfully to treat other oxide nanocrystals, including $NOBF_4$,[142] 4-bromobenzenediazonium tetrafluoroborate,[142] tetramethyloxonium tetrafluoroborate (Me_3OBF_4, a Meerwein's salt),[315] formic acid,[313] and ammonium thiocyanate (NH_4SCN).[314] None of these approaches proved effective for ICO nanocrystals, either resulting in dissolution of the particles into the ligand exchange solution or being ineffective in removal of the surface ligands. This result suggest an unusually strong bond between surface cadmium species and surfactant the oleic acid. Instead, annealing of the films was performed to remove the ligand. Annealing above 300°C in air proved effective in removing the oleic acid, resulting in conductive films of ICO nanocrystals, as measured using a standard multimeter. The transmission of the film after annealing indicates a significant redshift of the peak, broadening, and reduction in LSPR intensity. The reduction in LSPR intensity suggests that the redshift of the spectrum results not only from an increase in coupling between nanocrystals, but also oxidation which reduces the number of carriers through filling of oxygen vacancies.[313]

The formed nanocrystal thin films were then studied before and after annealing using spectroscopic ellipsometry to extract the optical constants of the films. This step is crucial towards the implementation of nanocrystal thin films in

metamaterials applications, as a material's optical constants are the starting point for simulations of optical response. This is particularly true in the case of TCOs, where even in bulk films the optical constants of the materials are dependent on the doping concentration, as well as thickness and microstructure.[306]

Unless a material is thick enough to absorb all of the incoming light, a model is required to fit the collected ellipsometry data which incorporates the substrate, from which information such as the film thickness and optical constants can be extracted. Many models can be utilized, but for TCO thin films, the most commonly used model is the Drude-Lorentz.[306] In this model, a Lorentzian line shape is typically used to fit the bandgap of the semiconductor, while a single Drude term is sufficient to model the optical properties in the NIR. In the TCO nanocrystal thin films described here, a Drude-Lorentz model can be used to model the optical response, but a more accurate (lower mean squared error) model utilizes two Lorentzians instead, without a Drude term. In the Lorentz-Lorentz model, there is a Lorentz oscillator in the UV to fit the bandgap, and in the NIR to fit the LSPR mode. This is a more appropriate model for the given system, particularly in the case of the unannealed films, because the LSPR remains in the optical transmission. In a Drude metal, the transmission should drop to a constant value and the reflectance should increase to a constant value, as observed for metals such as gold or silver. Simulated optical constants for the two types of models are shown in Figure 50. From these plots, it is clear that the

two models are quite similar less than a wavelength of 2400 nm, which is the limit of the ellipsometric measurement.

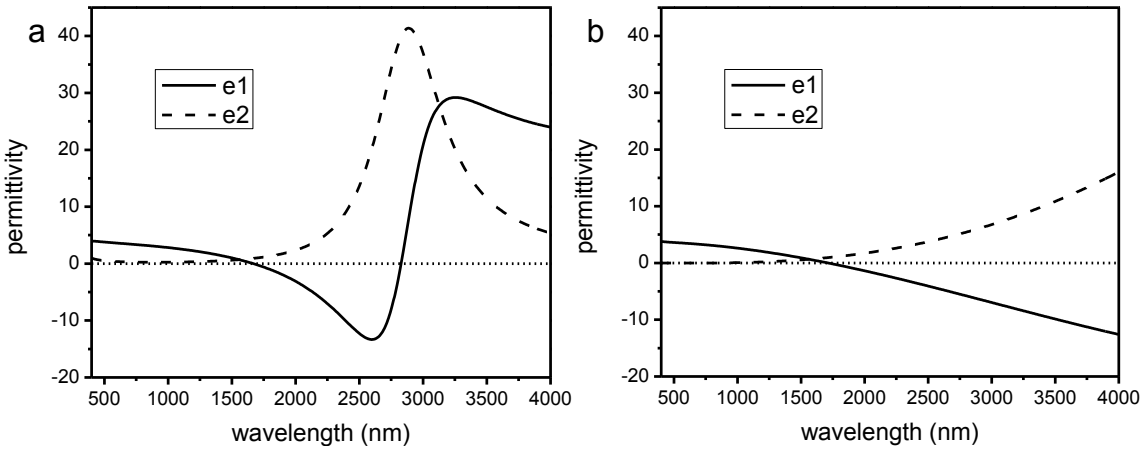

Figure 50: Simulated optical constants for optical models of TCO films, a) Lorentz-Lorentz and b) Drude-Lorentz.

Figure 51 displays the optical constants extracted using the two Lorentz model for films of ICO nanocrystals before and after annealing. For the annealed films which have appreciably DC conductivity, metallic-like behavior is expected, and the value of ε_1 would be expected to become negative at a certain point, which corresponds to the plasma frequency. This is observed experimentally, and the plasma frequency lies between 2200 nm and 2750 nm, although the 10% ICO sample does not cross zero within the experimental window. By changing the doping concentration, it is observed that the value of plasma frequency is tunable in the annealed films.

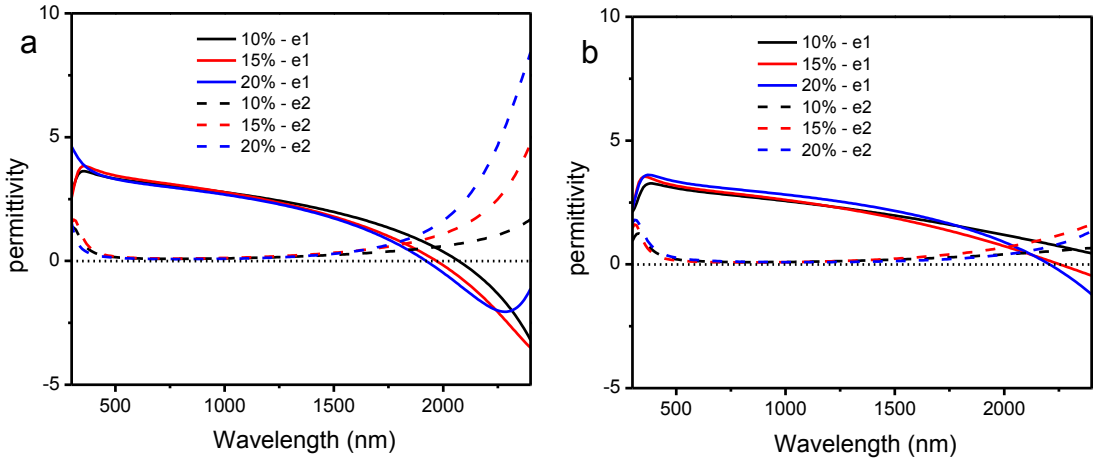

Figure 51: Extracted complex permittivity for films of 10, 15, and 20% ICO a) before and b) after annealing.

Intriguingly, negative values of ε_1 are also extracted for unannealed films of ICO nanocrystals (Figure 51a). This is surprising considering that the surfactants which separate the particles prevent conduction, making the films completely insulating based on DC conductivity. In fact, the plasma frequency of the unannealed films actually significantly exceeds the annealed films, and is tunable from 1930 nm to 2080 nm depending on doping concentration. The physical meaning of negative permittivity is related to electron oscillation in a material. In a Drude metal, when electromagnetic waves which have lower frequency lower than the plasma frequency (ie in the wavelength range where the material has negative permittivity) impinge on a surface, the electrons begin to oscillate collectively at that frequency, resulting in high reflectivity. In the two Lorentz model, negative permittivity is only observed over a narrow wavelength range, which presents an unusual set of optical constants, which must be further

explored. Similar observations have been made on films of silver nanoparticles embedded in polymer.[316] At sufficient fill fractions of Ag (high loading), a small wavelength range of negative permittivity is observed, which is proposed to result from dipolar coupling between particles, resulting in collective modes between separate nanocrystals. Unfortunately, the authors to not indicate whether the Ag/polymer films display DC conductivity, which would indicate whether Ag particles are capable of forming conductive channels at high fill fractions.

Presumably, the negative permittivity observed for the ICO nanocrystal films also results from the mixing of single particle modes into collective modes of electron oscillation. This produces an optically metallic material which has very small DC conductivity. Interestingly, similar results were not observed in films produced by our group using gold nanocrystals coated with a similar surfactant, oleylamine.[311] In that case, thin films of gold particles with surfactant appeared as dielectrics, but could be converted to having a metallic-like response after the ligands were removed. Several factors may explain the differences between ICO and gold. One major difference between the two materials is the loss component of the materials. Gold is known to be quite a lossy material, particularly in the visible, while silver and TCO films have much less loss, which may play a role in the increased plasmonic coupling observed between particles. On the other hand, particle size should also be considered as an important contributor as the smaller (6 nm) gold particles have significantly more organic than 8-12 nm ICO

nanocrystals. In the future, multiple types of plasmonic nanocrystals should be investigated with similar particle sizes to investigate the influence of particle size and loss on the optical constants of composite films.

4.1.4 Conclusions

We have shown that conductive thin films of ICO nanocrystals can be produced through spincoating, followed by annealing in air which removes surface ligands. Thin films were studied by spectroscopic ellipsometry to extract the effective optical constants. Negative permittivity was extracted for both unannealed and annealed films using a two Lorentz model. While negative permittivity was expected in the conductive annealed films, the observation of negative permittivity in unannealed films is explained based on plasmonic coupling between individual ICO particles which results in collective electron oscillations. In the future, the optical constants of these films should be extracted over a larger wavelength range, such that the nature of the localized modes can be better understood.

4.3 Future Work

I have a firm belief that semiconductor plasmonics have a very bright future in many applications. Numerous unusual and remarkable phenomena have already been observed through use of traditional plasmonic metals, including SERS, sensors, photothermal therapies, biological labels, and plasmonic enhanced fluorescence. The added tunability of semiconductors opens the door to active plasmonic structures, which are responsive to light, electrical currents, or temperature and can be sensitively modulated. Furthermore, theoretical and experimental advances in optical metamaterials which incorporate semiconductor plasmonics are sure to expand the range of applications.

5. Protein-Nanocrystal Hybrids[X]

5.1 Soluble Gold-Protein-Cofactor Complexes for Enhanced Fluorescence

5.1.1 Introduction

Small gold crystallites show strong optical absorptions referred to as localized surface plasmonic resonances (LSPRs) which result from the collective oscillations of free electrons. Nanorods of gold have two plasmonic resonance modes, transverse and longitudinal, due to their anisotropic shape. The longitudinal resonance can be tuned from the visible to the NIR depending on the aspect ratio of the rod.[317] The transverse mode typically lies between 500 and 600 nm and the longitudinal mode can be varied from 600 to 1600 nm. The LSPR results in an enhanced electric field in the particle vicinity. If fluorescent materials can be localized nearby the particle surface (specifically the tips of the nanorods) they will experience very large fields, potentially leading to enhanced fluorescence quantum yield, referred to as plasmonic fluorescence enhancement, as reported previously by several groups.[277,278,318] Our group has demonstrated that highly monodisperse colloidal gold nanorods can be synthesized in aqueous solution with a tunable aspect ratio by precisely varying

---

[X] Many thanks to Dahlia R. Klein, an excellent undergraduate researcher who conducted much of this experimental work and Xingchen Ye for providing the gold nanorods. We acknowledge the contributions of Prof. Jeffery Saven, Dr. Christopher Lanci, and Matthew Eibling for providing protein samples and advice on procedures.

the reaction conditions and through addition of aromatic additives.[270] The aspect ratios vary from approximately 2 to 5, which gives a large potential range for the frequency of the longitudinal mode to interact with fluorophores.

Many reports of plasmonic fluorescence enhancement have been demonstrated in the solid state, such as the enhanced fluorescence from thin films of CdSe quantum dots/dyes and Ag nanoprisms or thin films of phosphors and metal nanoparticles separated by an ALD spacer layer.[277,279,318,319] On the other hand, many potential applications, particularly those *in vivo*, necessitate a fluorophore-nanoparticle complex compatible with biological media. In this work, we seek to produce fluorophore-gold nanorod complexes soluble in buffered solution which demonstrate enhanced fluorescence due to plasmonic coupling. Such fluorophores may act as sensitive biomarkers or, depending on the sensitivity, could act as local probes of fluorophore environment.

In order to direct the interaction of a fluorophore with the nanorod's surface, we utilize computationally designed proteins, consisting of four alpha-helical bundles which have been shown to allow for vectorial orientation of a non-biological porphyrin cofactors at a liquid-air interface.[320,321] These proteins have highly selective binding sites that only bind to specific metal porphyrins. In this work, diphenylporphyrin zinc (PZn) acts as the cofactor, but further studies could include a host of other porphyrins which bind in the protein's hydrophobic pocket, including RuPZn. This opens the possibility to design linking chemistries and

binding pockets which provide improved functionality, as well as develop systems in which dynamic exchange processes can be monitored.

5.1.2 Experimental

Layer by Layer Polyelectrolyte Coating:

Gold nanorods were synthesized as described previously.[270] The first step to assembling the nanorod-protein complex is to coat the gold nanorods with organic polyelectrolyte layers. This method provides the proper functionalization to bind to the next molecule in the complex and will ultimately stabilize the complex in a buffer. As synthesized, the gold nanorods are coated in a positively-charged molecule cetyltrimethylammonium bromide (CTAB) and dissolved in water.[270] We adapted a method for layer by layer polymer coating (LbL) of the gold nanorods using negatively-charged poly(sodium 4-styrenesulfonate) (PSS) and positively-charged poly(allylamine hydrochloride) (PAH), with molecular weights of approximately 70,000 g/mol and 15,000 g/mol, respectively.[322] PAH is functionalized with exposed primary amines, which are used to bind to a crosslinker molecule discussed in the next section. The process works by alternating the charge of the polyelectrolyte layers, building up a micelle around the nanorod held together by electrostatic charge.

Stock solutions of PSS and PAH were prepared by dissolving 100 mg of one of the polymers in 10 mL of 1 mM NaCl solution. 3 mL of gold nanorods, as synthesized, were centrifuged for 6 minutes at 8000 rpm. The solid was

resuspended in 1 mL of 50 mM NaCl solution and 200 µL of PSS (-) stock solution. Then, the solution was placed on a shaker at 1000 rpm for 30 minutes. Then, it was centrifuged at 8000 rpm for 6 minutes. For the second layer of polyelectrolyte coating, the particles resuspended in 1 mL of 50 mM NaCl solution and 200 µL of PAH (+) stock solution, followed by being placed on a shaker at 1000 rpm for 30 minutes. This process can be repeated for the desired even number of layers to build a spacer between the gold nanorods and the protein/cofactor complex, leaving PAH (+) as the top layer of the nanorods. To wash, they were resuspended in 1 mL of 50 mM NaCl solution and then centrifuged for 6 minutes at 8000 rpm twice. They were finally resuspended in 1 mL of DMSO.

SMCC Coating:

Succinimidyl 4-(N-maleimidomethyl)cyclohexane-1-carboxylate (SMCC) is a crosslinker molecule soluble in DMSO that binds to primary amines and thiol groups, sold by Thermo Scientific. When added to the polyelectrolyte-coated gold nanorods, it binds to the top PAH (+) layer on the surface of the nanorods. The SMCC stock solution was prepared by dissolving 6.8 mg of SMCC in 2 mL of DMSO and stored at 4°C. 100 µL of this SMCC stock solution was added to 1 mL of the polyelectrolyte-coated gold nanorods in DMSO. The solution was placed on the shaker for 30 minutes at 1000 rpm and was then washed twice using 1 mL

of DMSO and then centrifuged for 6 minutes at 8000 rpm. The particles were then resuspended in 1 mL of DMSO.

Protein Binding:

Designer proteins are prepared on a protein synthesizer as described previously.[323] PZn cofactors were dissolved in DMSO and injected quickly into a buffered solution of protein. After stirring, the excess cofactor was removed through centrifugation. The gold nanorods soluble in DMSO with SMCC coating were added to a buffered solution of protein with cofactor bound and stirred for several hours to allow for binding. Only the soluble portion of this solution was studied optically.

Maleimide Detection:

A maleimide quantification assay kit was purchased from Abcam to determine whether the SMCC crosslinker had bound to the polyelectrolyte-coated gold nanorods. The test was performed according to manufacturer's instructions using serial dilutions of the samples along with maleimide standards included in the kit.

Quantum Yield:

The quantum yield of PZn was measured relative to a fluorescent dye, Lucifer Yellow, purchased through Sigma as Lucifer Yellow CH dilithium salt, which has a published quantum yield of 0.21.[324]

5.1.3 Results and Discussion

The fluorophore PZn has optical properties common to porphryin complexes. When excited at 415 nm into the Soret band, PZn has fluorescence emission peaks between 500 and 700 nm, resulting from S1 → S0 transitions. By coupling the longitudinal plasmon modes of the gold nanorod (Figure 52) with the fluorescence emission of PZn, it may experience plasmonic fluorescence enhancement (PFE).[278] The fluorescence intensity of a molecule is given by:

$$I = \gamma_{ex}\eta_f\varepsilon_{coll}$$

, where γ_{ex} is the excitation rate, η_f is the emission quantum yield, and ε_{coll} is the light collection efficiency of optical measurement.

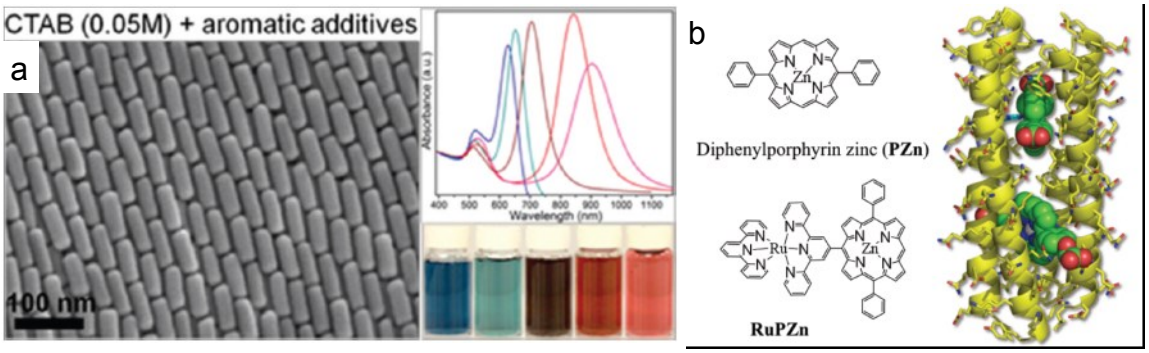

Figure 52: a) TEM image, absorbance spectrum and photographs of highly monodisperse gold nanorods with tunable longitudinal plasmonic resonance peaks, ranging from 600 to 900 nm. b) Chemical structure of diphenylporphyrin zinc (PZn) and RuPZn and an artistic representation of a computationally designed protein with two PZn molecules bound within it.

There are two mechanisms by which a plasmonic resonance can affect the fluorescence intensity. γ_{ex} can increase due to the localized electric field enhancement from the longitudinal plasmon mode if the plasmonic resonance

overlaps with the dye absorbance. In addition, the η_f of the fluorophore can be increased through interactions with the plasmonic resonance, which is more relevant in this work, due to the potential overlap of gold's longitudinal plasmon resonance with the S1 → S0 emission from PZn. In fact, this is also an advantage of using a porphyrin fluorophore, as the absorbance and emission bands are spectrally separated, potentially allowing for each of the enhancement mechanisms to be probed separately. The quantum yield is given by:

$$\eta_f = \frac{\gamma_{f,r}}{\gamma_{f,r} + \gamma_{f,nr}}$$

, where $\gamma_{f,r}$ represents radiative decay rate and $\gamma_{f,\mathrm{n}r}$ represents nonradiative decay rate of the fluorophore. The plasmonic resonance can potentially increase η_f by providing alternate pathways for decay through resonance, which increases the ratio of the radiative decay rate to the total decay rate. Since the longitudinal mode's absorbance peak can be tuned throughout a wide spectrum by altering the aspect ratio of the rods, it can be tuned very closely to the fluorescence emission peak of a fluorophore for maximized enhancement.

The overall process of constructing this nanorod-protein complex begins with gold nanorods with a longitudinal plasmon peak corresponding to the fluorophore's emission peak (Figure 53). Next, a polyelectrolyte coating is added to the nanorods to build a tunable spacer layer between the nanorod and the protein, which is intended to prevent electron transfer between the two systems. The final layer of the positively charged polyelectrolyte contains primary amines

(actually ammonium at low pH), which bind selectively to a common chemical crosslinker called SMCC. The other end of SMCC contains a maleimide, which binds strongly to thiol groups. The designer protein, with the fluorophore bound inside, has two exposed cysteine residues, which readily bind to the SMCC. The entire complex can then be dissolved in a buffered solution necessary to maintain the protein's rigid structure. We excited the Soret band, which has a peak at approximately 416 nm outside the protein and 419 nm inside the protein.

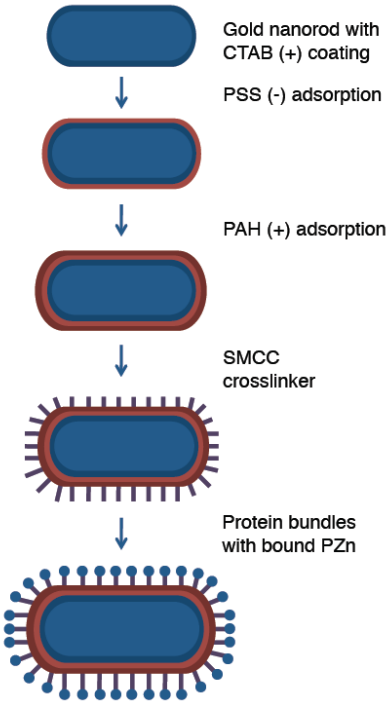

Figure 53: Schematic diagram for assembly of the nanorod-protein complex.

The results of the maleimide test showed that in a sample of polyelectrolyte coated gold nanorods functionalized with SMCC, the maleimide concentration was significantly above the blank control, at roughly 3 μM. This

sample was compared to another sample that had used been polyelectrolyte coated without the presence of NaCl throughout the process, and was found to have no maleimide. These results suggest that the presence of NaCl during the polyelectrolyte coating is necessary to stabilize the ions in the solution during the coating and allow for successive polymer layers to be deposited. Furthermore, it confirmed that the SMCC was indeed bound to primary amines on the micelles encompassing the nanorods.

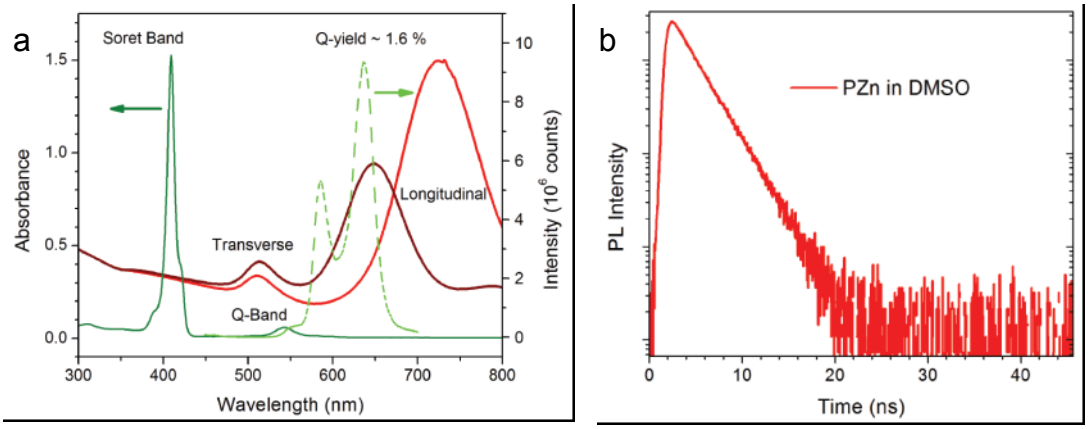

Figure 54: b) Optical absorbance (dark green) and emission spectra at 419 nm excitation (light green) of the PZn cofactor bound to the protein and the extincation spectrum of two different samples of gold nanorods with different aspect ratios. a) Time-resolved photoluminescence of the PZn fluorophore in DMSO.

Before linking the PZn-protein complex to the gold nanorod, the quantum yield of the PZn in and out of the protein must first be determined. The quantum yield of a compound X relative to a standard ST is given by:

$$\Phi_x = \Phi_{ST}\left(\frac{Grad_x}{Grad_{ST}}\right)\left(\frac{{n_x}^2}{{n_{ST}}^2}\right)$$

, where is Φ the quantum yield, *Grad* is the gradient of the plot of fluorescence emission area vs. absorbance intensity, and *n* is the refractive index of the solvent for each fluorophore. The absorbance peak and excitation wavelength of PZn shift upon binding to the protein from 416nm to 419 nm. The calculated quantum yields of the PZn outside of and bound to the protein were 1.62% and 0.91%, respectively. This result suggests that increased electronic coupling between the PZn and the protein causes a reduction in the quantum yield. The lifetime of the fluorescence was also measured, which is about 2.75 ns.

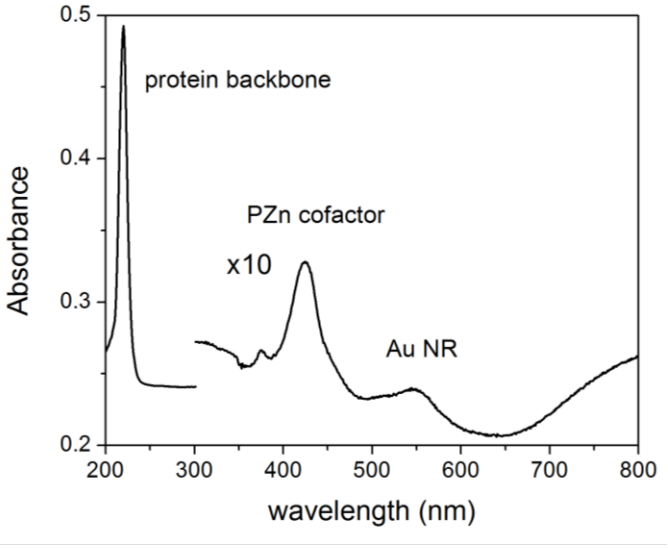

Figure 55: Optical absorbance of buffer-soluble gold-protein-cofactor heterostructure.

The SMCC coated gold nanorods solublized in DMSO were added to a solution of the protein with cofactor and binding was found to occur. After several washes, the optical absorbance confirms the presence of Au nanorods, protein and cofactor all in one soluble conjugate (Figure 55). However, there are some

issues with the resulting complex. Firstly, while the nanorod sample initially was closely overlapped with the emission peaks, the longitudinal mode is severely red-shifted in the final complex, suggesting aggregation. In addition, this complex is found to degrade in several days, releasing the chromophore, which prevented the optical properties from being properly measured. Future studies will start with smaller nanorods with more appropriate optical properties which allow for better overlap.

5.1.4 Conclusions and Future Work

The next step of the project is to study the optical properties of the nanorod-protein complex, including the quantum yield and the TRPL. We expect that the lifetime will be reduced and the quantum yield will increase if PFE is occurring via the interaction of gold nanorods with the fluorophore. Once this result is confirmed, the nanorods' longitudinal plasmon peak can be tuned on and off of the porphyrin's fluorescence emission to ascertain the influence on the PFE effect. In addition, the polyelectrolyte spacing layer can be varied to observe how the distance between the nanorod and the porphyrin change the porphyrin's quantum yield.

6. Conclusions

In this thesis, novel synthetic methods have been described for the directed synthesis of wide bandgap semiconductor nanocrystals with tunable morphology and composition. Through use of the nonaqueous synthesis techniques first developed for the preparation of quantum dots, greater control over the shape, size, and composition of the wide bandgap semiconductors has been demonstrated. This elevated control allows for the materials properties of oxide nanocrystals to be understood in a more precise way than previously possible. Rather than the collective response being attributed to a distribution of morphologies and compositions, it can be correlated with precise structural and chemical properties of a given sample.

In chapter 2, synthetic methods were described for precise tuning of the morphology, phase, and composition of TiO_2 nanocrystals. Fluoride containing precursors were shown to selectively expose the {001} facet of anatase under nonaqueous conditions, allowing for shape control of TiO_2 nanocrystals. These precursors were also shown to promote the formation of oxygen vacancies, which alter the color of the nanocrystals. The morphology was shown to influence photocatalytic activity, allowing for derivation of the relative reactivity of the {001} and {101} facets. Using a separate synthetic method, ultrathin anatase nanorods could be produced which self assemble into ordered superlattices. The nanorods were shown to be easily separable by size using a depletion-attraction enhanced

size-selective precipitation procedure. The ligand is exchanged from the monodisperse nanorods and they are found to be active for photodegradation of methylene blue. A seeded growth approach was utilized for the preparation of larger nanorods of the unusual brookite TiO_2 phase with tunable length. These nanorods are shown to be highly active photocatalysts for hydrogen evolution.

In chapter 3, synthetic procedures are described for synthesizing uniform ZnO nanocrystals. ZnO can be effectively doped with Co with minimal change in morphology, incorporation of which is shown to alter the optical properties of the nanocrystals. Reaction temperature is proposed to alter the photoluminescence of undoped ZnO nanocrystals.

In chapter 4, a new plasmonic semiconductor nanocrystal is described, indium doped cadmium oxide. The high level of control is over the shape and size of this material allows for the influence of shape on plasmonic response to be demonstrated for the first time. Thin films of conductive oxide nanocrystals are produced which display unique optical phenomena. Even when separate by surfactant, nanocrystal films display metallic-like optical constants, as determined by spectroscopic ellipsometry, which are tunable depending on doping concentraiton. Post-annealing, transparent conductive oxide films can be produced with relatively mild annealing temperatures.

The controlled nonaqueous synthesis of wide bandgap semiconductor nanocrystals provides many opportunities for future endeavors. In the 20 years

since the hot injection method was first developed, the synthesis of quantum dots has substantially increased in complexity, allowing for the synthesis of core-shells, heterostructures, and highly anisotropic morphologies. Through modification of synthetic parameters, the morphological control of oxide nanocrystals will surely follow, particularly through a more complete understanding of the mechanisms of particle formation and shape control.

Nanotechnology is a highly interdisciplinary and application-oriented branch of science. Only through the collaboration of individuals from dissimilar backgrounds can the big problems be solved, and one must often be willing to delve into a field which is mysterious to find an answer. While challenging, it comes with great rewards, and it promises to motivate researchers for years to come.

7. APPENDIX A – X-ray scattering simulation code

C++ code (XRD.exe)[XI]

What follows is the C++ code written to simulate the X-ray scattering from a set of atomic coordinates. As inputs, the code requires the following:

1) file xyz, which is a tab-delimited listing of the atomic coordinates (in angstroms) of a nanocrystal followed by an index (0, 1, 2, …) which signifies the type of atom.
2) file p, which contains a tab delimited listing of the Cromer-Mann coefficients (see list below) for each atom (in the order a1, a2, a3, b1, b2, b3, c), preceded by the atomic index.
3) float lambda, which is the desired wavelength of the X-rays (in angstroms).
4) float theta0, which is the starting value of 2-theta (in degrees)
5) float thetaM, which is the ending value of 2-theta (in degrees)
6) float thetas, the step size in 2-theta (in degrees)
7) float DWFACTOR, the Debye-Waller factor (in square angstroms)

This code can be compiled with standard compilers.

```
//Last modified 1/15/2013
//Version 1.0
//Authors: Steve Hershman, Thomas R. Gordon, Vicky Doan-Nguyen
//xrd.exe xyz p lambda theta0 thetaM thetaS DWFACTOR
//input files should have newlines at the end or else the last item won't get read!.
```

[XI] The C++ code was primarily written by Steve G. Hershman, but was debugged and modified by T.R.G. and Vicky Doan-Nguyen.

```
#include <iostream>
#include <sstream>
#include <fstream>
#include <string>
#include <vector>
#include <algorithm>
#include <cmath>

//constants - Many of these are changed by command line parameters
using namespace std;
float res=100.0;
float lambda=1.5406;
float theta0=10;
float thetaM=120;
float thetaS=0.05;
float DWFACTOR=1.0;
const float PI=3.1415926;
vector<vector<float>*> paramd;

//Function Declarations
float calc_s(float theta);
float calc_at_sct_factor(float s, int at);

template <class T> T from_string(const std::string& s)  {
   T t;

   std::istringstream iss(s);
   iss >> std::dec >> t;
   return t;
}

void doub_split(const string& s, char c,
           vector<float>& v) {
   //No error checking
   int i = 0;
   int j = s.find(c);
   float tempnum;

   while (j >= 0) {
      v.push_back(from_string<float>(s.substr(i,j-i)));

      i = ++j;
      j = s.find(c, j);

      if (j < 0) {
        v.push_back(from_string<float>(s.substr(i,s.length())));


      }
   }
}
```

```
void doub_loadCSV(istream& in, vector<vector<float>*>& data) {

   vector<float>* p = NULL;
   string tmp;

   while (!in.eof( )) {
      getline(in, tmp, '\n');                    // Grab the next line

      p = new vector<float>( );
      doub_split(tmp, '\t', *p);

      data.push_back(p);

      tmp.clear( );
   }
}

int main(int argc, char** argv) {
//Checks command line paramters.  Note the lack of error checking.  If you try to wrong
the script, it will wrong your results!
if (argc < 8)
return(EXIT_FAILURE);
ifstream xyz(argv[1]);
ifstream param(argv[2]);
lambda = from_string<float>(argv[3]);
theta0 = from_string<float>(argv[4]);
thetaM = from_string<float>(argv[5]);
thetaS = from_string<float>(argv[6]);
DWFACTOR = from_string<float>(argv[7]);
if (!xyz || !param)
return(EXIT_FAILURE);

//Read in files using doub_loadCSV
//Paramd was declared earlier because its used by the scattering angle function
vector<vector<float>*> xyzd;
doub_loadCSV(xyz, xyzd);
doub_loadCSV(param, paramd);
int num_atom = xyzd.size()-1;
int atom_types=paramd.size()-1 ;
int num_comb = int(pow(2.0, atom_types+1)-2);
//initalize Dist count array of arrays.  The inner arrays will grow dynamically!
vector<vector<int> > dist_count;
for ( int i = 0; i < num_comb; i++ ) {
    dist_count.push_back ( vector<int>() );
}
// This is an array that will let us go back from a bondtype to the 2 atomtypes.
vector<vector<int> > btmem ( num_comb, vector<int> ( 2 ) );
for(int at1=0; at1 < atom_types; at1++) {
    for(int at2=0; at2 < atom_types; at2++) {
        int bt=int(pow(2.0, at1) + pow(2.0, at2)-2);
        btmem[bt][0]=at1;
        btmem[bt][1]=at2;
    }
```

```
}
//This initalizes array that will count number of copies of each type of atom.
vector<int> at_count;
for(int i=0; i<atom_types; i++){
    at_count.push_back(0);
}

int* bt_store=new int[num_atom];
for( int i=0; i < num_atom; ++i){
    bt_store[i]=int(pow(2, (*xyzd[i])[3]));
}

for( int i=0; i < num_atom; ++i){
    //Count atomtype
    at_count[ int((*xyzd[i])[3]) ]+=1;
    //For all other atoms, find distance and put it in memory
    for (int j=i+1; j < num_atom ; ++j){
        float dx = pow( (*xyzd[i])[0] - (*xyzd[j])[0], 2);
        float dy = pow( (*xyzd[i])[1] - (*xyzd[j])[1], 2);
        float dz = pow( (*xyzd[i])[2] - (*xyzd[j])[2], 2);
        int bt = bt_store[i]+bt_store[j]-2;
        unsigned int dist=int(res*sqrt(dx+dy+dz));
//Grow list to appropriate size - this removes need for max dist.
    while(dist > dist_count[bt].size())
        dist_count[bt].push_back(0);
        dist_count[bt][dist]+=1;
        }
}
//This is where the calculation is
for( float theta=theta0; theta<thetaM; theta+=thetaS){ //for each theta
    float s=calc_s(theta/2.0);
    //bigtot is for all bondtypes.  tots are used for each bondtype
    float bigtot=0.0;
    for (int bt=0; bt<num_comb; bt++){ //for each bondtype
        float tot=0.0;
        for(unsigned int d=0; d < dist_count[bt].size(); d++){
            if(dist_count[bt][d]>0){
            float dist_cont=dist_count[bt][d]/(d/res) *
sin(2.0*PI*s*d/res  );
            tot+= dist_cont;
            }
        }
        int at1=btmem[bt][0];
        int at2=btmem[bt][1];
        float ss=calc_at_sct_factor(s, at1)*calc_at_sct_factor(s,
at2)/(PI*s);
        if (ss<0){
            cout << "ss<0" << endl;
        }
        tot*= ss;
        bigtot+=tot;
    }
    for(int at=0; at<atom_types; at++){
```

```
            bigtot+=pow(calc_at_sct_factor(s, at), 2) * at_count[at];
        }
        cout << theta <<"\t" <<bigtot <<"\n";
        }
}

float calc_s(float theta){
/* This function returns the value of S at a given theta. */
        float s=(2*sin(theta*PI/180))/lambda;
        if (s<0){
            cout << "S<0! "<<endl;
        }
       return s;
}

float calc_at_sct_factor(float s, int at){
/* Returns the atomic scattering factor (f) at a given value of S. Equation taken from
Intl. Tables for crystallography. f is then multiplied a Debye-Waller factor to simulate
the effects of thermal vibration. */
        float at_sct_factor=0.0;
        for(int index=0;index<4;index++){
            at_sct_factor+=(*paramd[at])[1+index]*exp(-1 *
(*paramd[at])[5+index] * (pow(s, 2)/4));
        }
        at_sct_factor+=(*paramd[at])[9];
        at_sct_factor*=exp(-DWFACTOR*(s*s)/4);
        return at_sct_factor;
}
```

Perl code (build_collection.pl)[XII]

The following code is used as a front end to XRD.exe. It takes as input a large supercell of atomic coordinates for a given crystal structure, cuts the desired shape(s), inputs the shapes into XRD.exe, and then calculates the Gaussian weighted result. In the current implementation, this source code must be edited prior to running. Editable settings lie between “Begin editable settings” and “End editable settings.” This code prints a log file with most of the relevant input parameters. Needed in the folder along with this file are:

[XII] Perl code was written and debugged by T.R.G. with some prior code from Steve G. Hershman.

1) file XRD.exe, the compiled C++ code written above. Input file name into definition of `$xrd_exe`.
2) .clust file, a tab delimited list of atomic symbol, charge, and x, y, z coordinates for a large supercell (each line is: Symbol Charge x y z), from which the nanocrystals will be cut (typically produced using Accelrys Materials Studio). Input file name into `$input`.
3) file of Cromer-Mann coefficients, tab delimited listing of atomic symbol charge and the 9 Cromer-Mann coefficients (a1, b1, a2, b2, a3, b3, c) (see below). Input file name into `$scattering_params`.

Other than these three files, all the parameters are set by variables defined in the perl file.

```
#!perl

use strict;
use warnings;
use Math::Trig;
use POSIX qw(strftime);

my $datetime1 = localtime();
print "\n$datetime1\n\n";

print "XRD v 1.0 - Welcome to X-ray Scattering Simulation
Software\n\nPlease enter directory name: ";
my $dir = <STDIN>;
chomp($dir);
mkdir($dir);
print "\n";

# Authors: Tom Gordon, Steve Hershman
# Version: 0.5
# Date: 01/17/2013
# Script: build_collection.pl


################################################################################
# Begin User Editable Settings
```

```
#Input File
my $input = "corr24nm.clust";        # Previously generated .clust file

#Shape Parameters
my $shape = "prolate";  # shape of particle (sphere, prolate, cube, oplate, hplate,
rod or bipyramid)
my $l = "60";        # diameter of the sphere or edge length of the cube or length of
orthorhombic/hexagonal plate or c-axis length of bipyramid to be simulated (in angstroms)

     # Parameters needed for prolate, oplate, hplate, rod or bipyramid
     my $pr = "1.3";      # aspect ratio of prolate (c/a)
     my $t = "20";        # thickness of plate (otherwise unused)
     my $w = "40";        # width of tetragonal bipyramid or rod (otherwise unused)

     # lattice constants (necessary for oplate and bipyramid, otherwise unused)
     my $alat = "5.781";     # a lattice constant
     my $clat = "11.6422";   # c lattice constant

     # Settings for adjusting a and c axes
     my $achange = "0";   # % change in the a lattice constant
     my $cchange = "0";   # % change in the c lattice constant

     # Settings for substituting one atom for another
     my $doping = "0";    # % of atom 1 to be doped with atom 2
     my $at1e = "O";      # element symbol of atom 1
     my $at1c = "-2";             # oxidation state of atom 1
     my $at2e = "F";      # element symbol of atom 2
     my $at2c = "-1";             # oxidation state of atom 2

#Distribution Parameters (for a single simulation, set $num to 1 and ignore other
parameters)
my $num = "1";           # number of points on to fit to gaussian (if not odd,
rounded up to next odd)
my $dev = "27";          # standard deviation in the size (in angstroms)
my $numdev = "2";        # number of standard deviations to fit

#XRD Calculation Parameters
my $out_tab=qq(XRD $shape $l $num $dev $numdev .tab);    # Name of tab
delimited output file
my $theta0 = 20;                 # Smallest value of 2theta
my $thetaM = 60;                 # Largest value of 2theta
my $thetaS = 0.05;               # 2theta step size
my $lambda=1.540562;             # Wavelength in Angstroms of source
my $debyewaller = 1.0;           # The debye waller factor

#Advanced/Environment Settings
my $scattering_params='cromer_mann.tab';     # The name of the file with
scattering parameters
my $xyz_out = 'xyz';     # Name of temporary file to hold xyz and atom type for all
atoms
my $p_out = 'p';         # Name of temporary file to store scattering parameters
my $n_out = 'n';         # Name of temporary file to store neutral atoms in case no
ions are present
```

```
my $xrd_exe = 'XRD_2012_new.exe';        # Name of C program that does x-ray
diffraction

#
# End User Editable Settings
################################################################################

open LOG, ">$dir/log.txt" || die "can't make log file!";
print LOG qq{Start:\t$datetime1\n
Input File:\t$input\n
Shape Parameters
Shape:\t$shape
Diameter/Edge Length/Length:\t$l
Plate or Bipyramid only:
\tThickness:\t$t
\tWidth:\t$w
Changes in lattice parameters:
\ta lattice constant:\t$alat
\ta change:\t$achange
\tc lattice constant:\t$clat\n
\tc change:\t$cchange
Distribution Parameters
Number of Crystals Simulated:\t$num
Standard Deviation:\t$dev
Number of Standard Deviations Spanned:\t$numdev\n
XRD parameters
Gaussian Weighted Output File:\t$out_tab
Theta0:\t$theta0
ThetaMax:\t$thetaM
Theta Step Size:\t$thetaS
Wavelength of X-ray:\t$lambda
Debye Waller Factor:\t$debyewaller
};


my @dist;
unless ($num % 2) {      # Tests for an odd
    $num+=1;         # If not odd, gives you next biggest odd
    warn "Number of points not odd, changed to $num.\n";
}

if ($num == 1) {
    push @dist, $l;
} else {
    my $half = int($num/2-.5);
    @dist = -$half..$half;  #Integers that span the origin (-n .. 0 .. n)
    foreach (@dist){
        $_ = $_*$dev*$numdev/($half)+$l;     #This loop changes array of
integers into the desired sizes of nanocrystals
    }
}

print "Will make $num nanocrystals with sizes (angstroms): @dist \n";
```

```
#Output files are made for each of the nanocrystals, file handles stored in a hash with
the nanocrystals sizes as keys. Output files named crystal size (e.g. crystal 46 for a
4.6nm particle).
my %handles;
foreach(@dist) {
    open my $fh, ">$dir/crystal_$_.txt" || die "Cannot open output
file";
    $handles{$_} = $fh;
}

my @at;
open CLUST, "<$input" or die "\nCannot find input file $input\nCheck
file name...\n\n";
my $atom_type_count=0;
my %atom_types;
if ($shape eq "sphere") {
#SPHERE - This routine calculates r (radius) for each point after centering and subtracts
any that are too big for the largest crystal needed.
    print "Go sphere!\n";
    my $maxrad = $dist[$num-1]/2;
    while (my $line = <CLUST>) {
        chomp $line;
        @at = split("\t", $line);
        my $k = $at[0];
        my $v = $at[1];
        if ($k eq $at1e && $v eq $at1c && rand(100) < $doping) {
            $k = $at2e;
            $v = $at2c;
        }
        my $x = $at[2]*(1+$achange/100)-$maxrad;
        my $y = $at[3]*(1+$achange/100)-$maxrad;
        my $z = $at[4]*(1+$cchange/100)-$maxrad;
        my $r = sqrt($x**2 + $y**2 + $z**2); #calculate the radius of each
atom from the translated crystal
        unless (exists $atom_types{$k}{$v}){
            $atom_types{$k}{$v}=$atom_type_count;
            $atom_type_count+=1;
        }
        foreach(@dist) {
            if ($r <= $_/2) {
                print {$handles{$_}} join("\t", $x, $y, $z,
$atom_types{$k}{$v}), "\n";
            }
        }
    }
#PROLATE - prolate spheroid with aspect ratio of $pr.
} elsif ($shape eq "prolate") {
    print "Go prolate!\n";
    my $maxrad = $dist[$num-1]/2;
    while (my $line = <CLUST>) {
        chomp $line;
        @at = split("\t", $line);
```

```
        my $k = $at[0];
        my $v = $at[1];
        if ($k eq $at1e && $v eq $at1c && rand(100) < $doping) {
            $k = $at2e;
            $v = $at2c;
        }
        my $x = $at[2]*(1+$achange/100)-$maxrad;
        my $y = $at[3]*(1+$achange/100)-$maxrad;
        my $z = $at[4]*(1+$cchange/100)-$maxrad*$pr;
        unless (exists $atom_types{$k}{$v}){
            $atom_types{$k}{$v}=$atom_type_count;
            $atom_type_count+=1;
        }
        foreach(@dist) {
            unless ( (($x**2+$y**2)/(($l/2)**2) +
$z**2/(($l/2*$pr)**2)) > 1){
                print {$handles{$_}} join("\t", $x, $y, $z,
$atom_types{$k}{$v}), "\n";
            }
        }
    }
#CUBE - This routine removes atoms larger than the largest cube needed, then prints to
file the other cubes needed.
} elsif ($shape eq "cube") {
    print "Go cube!\n";
    while (my $line = <CLUST>) {
        chomp $line;
        @at = split("\t", $line);
        my $k = $at[0];
        my $v = $at[1];
        if ($k eq $at1e && $v eq $at1c && rand(100) < $doping) {
            $k = $at2e;
            $v = $at2c;
        }
        my $x = $at[2]*(1+$achange/100);
        my $y = $at[3]*(1+$achange/100);
        my $z = $at[4]*(1+$cchange/100);
        unless (exists $atom_types{$k}{$v}){
            $atom_types{$k}{$v}=$atom_type_count;
            $atom_type_count+=1;
        }
        foreach(@dist) {
            unless ($x > $_ || $y > $_ || $z > $_ ){
                print {$handles{$_}} join("\t", $x, $y, $z,
$atom_types{$k}{$v}), "\n";
            }
        }
    }
#ROD - This produces a rod morphology with spherical caps on the ends. There would be an
issue if the rod is made too short relative to the width.  If l is less than 2w, you'd
have problems.   This routine removes atoms larger than the largest rod needed, then
prints to file the other rods needed.
} elsif ($shape eq "rod") {
```

```
    print "Go rod!\n";
    my $asprat = $w/$l;
    my $maxrad = $dist[$num-1]*$asprat/2;
    while (my $line = <CLUST>) {
        chomp $line;
        @at = split("\t", $line);
        my $k = $at[0];
        my $v = $at[1];
        if ($k eq $at1e && $v eq $at1c && rand(100) < $doping) {
            $k = $at2e;
            $v = $at2c;
        }
        my $x = $at[2]*(1+$achange/100)-$maxrad;
        my $y = $at[3]*(1+$achange/100)-$maxrad;
        my $z = $at[4]*(1+$cchange/100);
        unless (exists $atom_types{$k}{$v}){
            $atom_types{$k}{$v}=$atom_type_count;
            $atom_type_count+=1;
        }
        foreach(@dist) {
            my $temprad = $_*$asprat/2;
            unless ( sqrt($x**2 + $y**2) > $temprad || $z > $_ ||
((sqrt($x**2+$y**2+($z-$temprad)**2) > $temprad) && $z < $temprad) ||
(sqrt($x**2+$y**2+($z-$_+$temprad)**2) > $temprad) && $z > ($_-
$temprad) ){
                print {$handles{$_}} join("\t", $x, $y, $z,
$atom_types{$k}{$v}), "\n";
            }
        }
    }
#OPLATE - The way this is currently being implemented, it only pertains to the
orthorhombic lathanide fluoride plates in which the short axis is the b (y) axis and the
edge of the plate is along the (1 0 1) direction.
} elsif ($shape eq "oplate") {
    print "Go plate!\n";
    my $asprat = $alat/$clat;
    my $maxl = $dist[$num-1];
    while (my $line = <CLUST>) {
        chomp $line;
        @at = split("\t", $line);
        my $k = $at[0];
        my $v = $at[1];
        if ($k eq $at1e && $v eq $at1c && rand(100) < $doping) {
            $k = $at2e;
            $v = $at2c;
        }
        my $x = $at[2]*(1+$achange/100)-$maxl/2;
        my $y = $at[3]*(1+$achange/100);
        my $z = $at[4]*(1+$cchange/100)-$maxl/(2*$asprat);
        unless (exists $atom_types{$k}{$v}){
            $atom_types{$k}{$v}=$atom_type_count;
            $atom_type_count+=1;
```

```
        }
        foreach(@dist) {
            unless( abs($x) > (-$asprat*abs($z) + $_/2) || $y >
$t*$_/$l){
                print {$handles{$_}} join("\t", $x, $y, $z,
$atom_types{$k}{$v}), "\n";
            }
        }
    }
#HPLATE - The way this is currently being implemented, it only pertains to the hexagonal
plates in which the short axis is the c (z) axis.  Would also work for hexagonal rod,
just make thickness very long.
} elsif ($shape eq "hplate") {
    print "Go plate!\n";
    my $maxl = $dist[$num-1];
    while (my $line = <CLUST>) {
        chomp $line;
        @at = split("\t", $line);
        my $k = $at[0];
        my $v = $at[1];
        if ($k eq $at1e && $v eq $at1c && rand(100) < $doping) {
            $k = $at2e;
            $v = $at2c;
        }
        my $x = $at[2]*(1+$achange/100)-$maxl/2;;
        my $y = $at[3]*(1+$achange/100)-$maxl/2;;
        my $z = $at[4]*(1+$cchange/100);
        unless (exists $atom_types{$k}{$v}){
            $atom_types{$k}{$v}=$atom_type_count;
            $atom_type_count+=1;
        }
        foreach(@dist) {
            unless( abs($y) > ($l/2 - (abs($x)/(sqrt(3)))) || abs($x) >
$l*(sqrt(3)/4) || $z > $t*$_/$l){
                print {$handles{$_}} join("\t", $x, $y, $z,
$atom_types{$k}{$v}), "\n";
            }
        }
    }
#BIPYRAMID - This was made to simulate the pattern for truncated tetragonal bipyramids of
TiO2, should work for other bipyramidal structures which are c-axis elongated.
} elsif ($shape eq "bipyramid") {
    print "Go bipyramid!\n";
    my $unitAR = $alat/$clat;
    my $crystalAR = $w/$l;
    my $maxz = $dist[$num-1];
    my $maxw = $maxz*$crystalAR;
    while (my $line = <CLUST>) {
        chomp $line;
        @at = split("\t", $line);
        my $k = $at[0];
        my $v = $at[1];
        my $x = ($at[2]*(1+$achange/100))-$maxw/2;
```

```
        my $y = ($at[3]*(1+$achange/100))-$maxw/2;
        my $z = ($at[4]*(1+$cchange/100))-$maxz/2;
        unless (exists $atom_types{$k}{$v}){
            $atom_types{$k}{$v}=$atom_type_count;
            $atom_type_count+=1;
        }
        foreach(@dist) {
            unless(abs($x)+$unitAR*abs($z) > $crystalAR*$_/2 ||
abs($y)+$unitAR*abs($z) > $crystalAR*$_/2 || abs($z) > $_/2){
                print {$handles{$_}} join("\t", $x, $y, $z,
$atom_types{$k}{$v}), "\n";
            }
        }
    }
#OCTAHEDRON - This was made to simulate the pattern for octahedra of CdO, will work for
other octahedra.
} elsif ($shape eq "octahedron") {
    print "Go octahedron!\n";
    my $maxl = $dist[$num-1];
    while (my $line = <CLUST>) {
        chomp $line;
        @at = split("\t", $line);
        my $k = $at[0];
        my $v = $at[1];
        if ($k eq $at1e && $v eq $at1c && rand(100) < $doping) {
            $k = $at2e;
            $v = $at2c;
        }
        my $x = ($at[2]*(1+$achange/100))-$maxl/2;
        my $y = ($at[3]*(1+$achange/100))-$maxl/2;
        my $z = ($at[4]*(1+$cchange/100))-$maxl/2;
        unless (exists $atom_types{$k}{$v}){
            $atom_types{$k}{$v}=$atom_type_count;
            $atom_type_count+=1;
        }
        foreach(@dist) {
            unless(abs($x)+abs($y)+abs($z) > $_/2){
                print {$handles{$_}} join("\t", $x, $y, $z,
$atom_types{$k}{$v}), "\n";
            }
        }
    }
}
# This section of the script opens the scattering parameters file and extracts
parameters.  The program will issue an error if it finds an atomtype twice or if one is
missing
# (But if both happen, then it won't know the difference!
# Script also substitutes the parameters for a neutral atom if parameters are not
available for a given -1 or -2 ion (noteable examples include S, Se and Te).
my $found_ats=0;
my $neutrals=0;
open NOUT, "> $n_out" or die "Can't open $n_out : $!";
open POUT, "> $p_out" or die "Can't open $p_out : $!";
```

```
open XRS, "< $scattering_params" or die "Can't open $scattering_params
: $!";
print "\tIndex\tAtom\tOxidation #\n";
while(my $line=<XRS>){
    chomp $line;
    my @data=split("\t", $line);     #tab delimited scattering parameters are
split into @data array
    #scat[atom][charge]=((A's), (B's), C)
    #scattering parameters are resorted from a1, b1, a2, etc. to a1, a2, a3, b1, etc.
    if( exists $atom_types{$data[0]}{$data[1]}){
        $found_ats+=1;
        print  "Found: \t".$atom_types{$data[0]}{$data[1]} . "\t" .
$data[0] . "\t" . $data[1] . "\n";
        print POUT join("\t", $atom_types{$data[0]}{$data[1]},
$data[2], $data[4], $data[6], $data[8], $data[3], $data[5], $data[7],
$data[9],$data[10]) . "\n";
    } elsif ( (exists $atom_types{$data[0]}{-2}) && ($data[1]==0)) {
        print NOUT join("\t", $data[0], $data[1],
$atom_types{$data[0]}{-2}, $data[2], $data[4], $data[6], $data[8],
$data[3], $data[5], $data[7], $data[9],$data[10]) . "\n";
        $neutrals+=1;
    } elsif ( (exists $atom_types{$data[0]}{-1}) && ($data[1]==0)) {
        print NOUT join("\t", $data[0], $data[1],
$atom_types{$data[0]}{-1}, $data[2], $data[4], $data[6], $data[8],
$data[3], $data[5], $data[7], $data[9],$data[10]) . "\n";
        $neutrals+=1;
    }
}
close XRS;

# I expanded this section so that if an -2 or -1 ion was not found and a neutral atom is
available, it is inserted.
if(($found_ats!=$atom_type_count)) {
    if ($neutrals==0) {
        print "$atom_type_count atoms found from atomisitic document.
\n";
        print "$found_ats ion/neutral atom in scattering parameters
file $scattering_params. \n";
        print "Could not find an atom type.  Look above to see which
were found (internal count, element, charge)\n";
        exit;
    } else {
        open (NOUT, "<$n_out") or die "Can't open $n_out : $!";
        my $l = <NOUT>;
        close NOUT;
        my @v = split('\t', $l);
        open (POUT, ">>$p_out") or die "Can't open $p_out : $!";
        print POUT join("\t", @v[2..11]);
        close POUT;
        warn "Error - No parameters for $v[0] ion, will use parameters
for neutral atom (minimal error for Z>37)\nAdded:\tsub \t$v[0] \t$v[1]
\n";
    }
```

```
}
close NOUT;
unlink $n_out;
close POUT;

open P, "<p" || die "can't find p";
open PSORT, ">psort" || die "can't find p";
my $ii=0;
my @sort;
while (<P>) {$sort[$ii++]=$_;}
@sort = sort byAtom @sort;
foreach (@sort) { print PSORT $_; }
unlink $p_out;

sub byAtom {
    my @one = split( '\t', $a );
    my @two = split( '\t', $b );
    ($one[0] <=> $two[0]);
}

# This calls the C program to do Xray Diffraction (loop does xrd on each of the
nanocrystals).
print "\nStarting XRD (oh boy!)....\n\n";
my %sum;
foreach (@dist) {
    print "crystal_$_.txt...";
    my $result = `$xrd_exe $dir/crystal_$_.txt psort $lambda $theta0
$thetaM $thetaS $debyewaller`;
    # This foreach loop splits the results of the xrd script into $theta and $bigtot and
prints them to a tab delimited file and a graph.
    open OUTTAB, ">$dir/XRD_$_.txt" || die "Cannot open XRD output
file";
    foreach my $line (split("\n", $result)){
        my @tmp = split("\t", $line);
        print OUTTAB "$tmp[0]\t$tmp[1]\n";  #Print to separate files for each
nanocrystal size
        my $gaussweight = (1/sqrt(2*pi*($dev**2)))*exp(-(($_-
$l)**2)/(2*$dev**2)));  #This is the Gaussian function, used to weight the data.
Mean and Std dev are used as inputs.
        my $bigtot=$gaussweight*$tmp[1];    #Multiplying by intensity measured
to weight the intensities
        $sum{$tmp[0]}+=$bigtot;     #Sum the gaussian weighted terms for each
theta (store in hash)
    }
    close OUTTAB;
    print "done!\n";
}
print "\nFinished!\n\n";

print "Calculating Distribution...\n";

open OUTNEW, ">$dir/$out_tab" or die "Can't open $out_tab : $!";
foreach (sort {$a <=> $b} keys(%sum) ){
```

```
    print OUTNEW "$_\t$sum{$_}\n";       #output the two arrays to a tab-
delimited file
}

$datetime1 = localtime();
print LOG "\nEnd:\t$datetime1\n";
close LOG;

close OUTNEW;
# And we're done!
print "DONE\n";

exit;
```

Cromer-Mann Coefficients.

The following is a listing of the Cromer-Mann coefficients for every atom and ion listed in the International Tables for Crystallography.[129] O^{2-} is not listed in the International Tables, but an estimated value was reported by Hovestreydt, et al.[325]

```
H   0   0.489918    20.6593 0.262003    7.74039 0.196767    49.5519 0.049879    2.20159
0.001305
H   -1  0.897661    53.1368 0.565616    15.187  0.415815    186.576 0.116973    3.56709
0.002389
He  0   0.8734  9.1037  0.6309  3.3568  0.3112  22.9276 0.178   0.9821  0.0064
Li  0   1.1282  3.9546  0.7508  1.0524  0.6175  85.3905 0.4653  168.261 0.0377
Li  1   0.6968  4.6237  0.7888  1.9557  0.3414  0.6316  0.1563  10.0953 0.0167
Be  0   1.5919  43.6427 1.1278  1.8623  0.5391  103.483 0.7029  0.542   0.0385
Be  2   6.2603  0.0027  0.8849  0.8313  0.7993  2.2758  0.1647  5.1146  -6.1092
B   0   2.0545  23.2185 1.3326  1.021   1.0979  60.3498 0.7068  0.1403  -0.1932
C   0   2.31    20.8439 1.02    10.2075 1.5886  0.5687  0.865   51.6512 0.2156
N   0   12.2126 0.0057  3.1322  9.8933  2.0125  28.9975 1.1663  0.5826  -11.529
O   0   3.0485  13.2771 2.2868  5.7011  1.5463  0.3239  0.867   32.9089 0.2508
O   -1  4.1916  12.8573 1.63969 4.17236 1.52673 47.0179 -20.307 -0.01404    21.9412
O   -2  3.75040 16.5151 2.84294 6.59203 1.54298 0.319201    1.62091 43.3486 0.242060
F   0   3.5392  10.2825 2.6412  4.2944  1.517   0.2615  1.0243  26.1476 0.2776
F   -1  3.6322  5.27756 3.51057 14.7353 1.26064 0.442258    0.940706    47.3437 0.653396
Ne  0   3.9553  8.4042  3.1125  3.4262  1.4546  0.2306  1.1251  21.7184 0.3515
Na  0   4.7626  3.285   3.1736  8.8422  1.2674  0.3136  1.1128  129.424 0.676
Na  1   3.2565  2.6671  3.9362  6.1153  1.3998  0.2001  1.0032  14.039  0.404
Mg  0   5.4204  2.8275  2.1735  79.2611 1.2269  0.3808  2.3073  7.1937  0.8584
Mg  2   3.4988  2.1676  3.8378  4.7542  1.3284  0.185   0.8497  10.1411 0.4853
Al  0   6.4202  3.0387  1.9002  0.7426  1.5936  31.5472 1.9646  85.0886 1.1151
Al  3   4.17448 1.93816 3.3876  4.14553 1.20296 0.228753    0.528137    8.28524 0.706786
Si  0   6.2915  2.4386  3.0353  32.3337 1.9891  0.6785  1.541   81.6937 1.1407
Si  4   4.43918 1.64167 3.20345 3.43757 1.19453 0.2149  0.41653 6.65365 0.746297
P   0   6.4345  1.9067  4.1791  27.157  1.78    0.526   1.4908  68.1645 1.1149
S   0   6.9053  1.4679  5.2034  22.2151 1.4379  0.2536  1.5863  56.172  0.8669
Cl  0   11.4604 0.0104  7.1964  1.1662  6.2556  18.5194 1.6455  47.7784 -9.5574
Cl  -1  18.2915 0.0066  7.2084  1.1717  6.5337  19.5424 2.3386  60.4486 -16.378
Ar  0   7.4845  0.9072  6.7723  14.8407 0.6539  43.8983 1.6442  33.3929 1.4445
K   0   8.2186  12.7949 7.4398  0.7748  1.0519  213.187 0.8659  41.6841 1.4228
K   1   7.9578  12.6331 7.4917  0.7674  6.359   -0.002  1.1915  31.9128 -4.9978
Ca  0   8.6266  10.4421 7.3873  0.6599  1.5899  85.7484 1.0211  178.437 1.3751
Ca  2   15.6348 -0.0074 7.9518  0.6089  8.4372  10.3116 0.8537  25.9905 -14.875
```

```
Sc  0   9.189   9.0213  7.3679  0.5729  1.6409  136.108 1.468   51.3531 1.3329
Sc  3   13.4008 0.29854 8.0273  7.9629  1.65943 -0.28604    1.57936 16.0662 -6.6667
Ti  0   9.7595  7.8508  7.3558  0.5 1.6991  35.6338 1.9021  116.105 1.2807
Ti  2   9.11423 7.5243  7.62174 0.457585    2.2793  19.5361 0.087899    61.6558 0.897155
Ti  3   17.7344 0.22061 8.73816 7.04716 5.25691 -0.15762    1.92134 15.9768 -14.652
Ti  4   19.5114 0.178847    8.23473 6.67018 2.01341 -0.29263    1.5208  12.9464 -13.28
V   0   10.2971 6.8657  7.3511  0.4385  2.0703  26.8938 2.0571  102.478 1.2199
V   2   10.106  6.8818  7.3541  0.4409  2.2884  20.3004 0.0223  115.122 1.2298
V   3   9.43141 6.39535 7.7419  0.383349    2.15343 15.1908 0.016865    63.969  0.656565
V   5   15.6887 0.679003    8.14208 5.40135 2.03081 9.97278 -9.576  0.940464    1.7143
Cr  0   10.6406 6.1038  7.3537  0.392   3.324   20.2626 1.4922  98.7399 1.1832
Cr  2   9.54034 5.66078 7.7509  0.344261    3.58274 13.3075 0.509107    32.4224 0.616898
Cr  3   9.6809  5.59463 7.81136 0.334393    2.87603 12.8288 0.113575    32.8761 0.518275
Mn  0   11.2819 5.3409  7.3573  0.3432  3.0193  17.8674 2.2441  83.7543 1.0896
Mn  2   10.8061 5.2796  7.362   0.3435  3.5268  14.343  0.2184  41.3235 1.0874
Mn  3   9.84521 4.91797 7.87194 0.294393    3.56531 10.8171 0.323613    24.1281 0.393974
Mn  4   9.96253 4.8485  7.97057 0.283303    2.76067 10.4852 0.054447    27.573  0.251877
Fe  0   11.7695 4.7611  7.3573  0.3072  3.5222  15.3535 2.3045  76.8805 1.0369
Fe  2   11.0424 4.6538  7.374   0.3053  4.1346  12.0546 0.4399  31.2809 1.0097
Fe  3   11.1764 4.6147  7.3863  0.3005  3.3948  11.6729 0.0724  38.5566 0.9707
Co  0   12.2841 4.2791  7.3409  0.2784  4.0034  13.5359 2.3488  71.1692 1.0118
Co  2   11.2296 4.1231  7.3883  0.2726  4.7393  10.2443 0.7108  25.6466 0.9324
Co  3   10.338  3.90969 7.88173 0.238668    4.76795 8.35583 0.725591    18.3491 0.286667
Ni  0   12.8376 3.8785  7.292   0.2565  4.4438  12.1763 2.38    66.3421 1.0341
Ni  2   11.4166 3.6766  7.4005  0.2449  5.3442  8.873   0.9773  22.1626 0.8614
Ni  3   10.7806 3.5477  7.75868 0.22314 5.22746 7.64468 0.847114    16.9673 0.386044
Cu  0   13.338  3.5828  7.1676  0.247   5.6158  11.3966 1.6735  64.8126 1.191
Cu  1   11.9475 3.3669  7.3573  0.2274  6.2455  8.6625  1.5578  25.8487 0.89
Cu  2   11.8168 3.37484 7.11181 0.244078    5.78135 7.9876  1.14523 19.897  1.14431
Zn  0   14.0743 3.2655  7.0318  0.2333  5.1652  10.3163 2.41    58.7097 1.3041
Zn  2   11.9719 2.9946  7.3862  0.2031  6.4668  7.0826  1.394   18.0995 0.7807
Ga  0   15.2354 3.0669  6.7006  0.2412  4.3591  10.7805 2.9623  61.4135 1.7189
Ga  3   12.692  2.81262 6.69883 0.22789 6.06692 6.36441 1.0066  14.4122 1.53545
Ge  0   16.0816 2.8509  6.3747  0.2516  3.7068  11.4468 3.683   54.7625 2.1313
Ge  4   12.9172 2.53718 6.70003 0.205855    6.06791 5.47913 0.859041    11.603  1.45572
As  0   16.6723 2.6345  6.0701  0.2647  3.4313  12.9479 4.2779  47.7972 2.531
Se  0   17.0006 2.4098  5.8196  0.2726  3.9731  15.2372 4.3543  43.8163 2.8409
Br  0   17.1789 2.1723  5.2358  16.5796 5.6377  0.2609  3.9851  41.4328 2.9557
Br  -1  17.1718 2.2059  6.3338  19.3345 5.5754  0.2871  3.7272  58.1535 3.1776
Kr  0   17.3555 1.9384  6.7286  16.5623 5.5493  0.2261  3.5375  39.3972 2.825
Rb  0   17.1784 1.7888  9.6435  17.3151 5.1399  0.2748  1.5292  164.934 3.4873
Rb  1   17.5816 1.7139  7.6598  14.7957 5.8981  0.1603  2.7817  31.2087 2.0782
Sr  0   17.5663 1.5564  9.8184  14.0988 5.422   0.1664  2.6694  132.376 2.5064
Sr  2   18.0874 1.4907  8.1373  12.6963 2.5654  24.5651 -34.193 -0.0138 41.4025
Y   0   17.776  1.4029  10.2946 12.8006 5.72629 0.125599    3.26588 104.354 1.91213
Y   3   17.9268 1.35417 9.1531  11.2145 1.76795 22.6599 -33.108 -0.01319    40.2602
Zr  0   17.8765 1.27618 10.948  11.916  5.41732 0.117622    3.65721 87.6627 2.06929
Zr  4   18.1668 1.2148  10.0562 10.1483 1.01118 21.6054 -2.6479 -0.10276    9.41454
Nb  0   17.6142 1.18865 12.0144 11.766  4.04183 0.204785    3.53346 69.7957 3.75591
Nb  3   19.8812 0.019175    18.0653 1.13305 11.0177 10.1621 1.94715 28.3389 -12.912
Nb  5   17.9163 1.12446 13.3417 0.028781    10.799  9.28206 0.337905    25.7228 -6.3934
Mo  0   3.7025  0.2772  17.2356 1.0958  12.8876 11.004  3.7429  61.6584 4.3875
Mo  3   21.1664 0.014734    18.2017 1.03031 11.7423 9.53659 2.30951 26.6307 -14.421
Mo  5   21.0149 0.014345    18.0992 1.02238 11.4632 8.78809 0.740625    23.3452 -14.316
Mo  6   17.8871 1.03649 11.175  8.48061 6.57891 0.058881    0   0   0.344941
Tc  0   19.1301 0.864132    11.0948 8.14487 4.64901 21.5707 2.71263 86.8472 5.40428
Ru  0   19.2674 0.80852 12.9182 8.43467 4.86337 24.7997 1.56756 94.2928 5.37874
Ru  3   18.5638 0.847329    13.2885 8.37164 9.32602 0.017662    3.00964 22.887  -3.1892
Ru  4   18.5003 0.844582    13.1787 8.12534 4.71304 0.36495 2.18535 20.8504 1.42357
Rh  0   19.2957 0.751536    14.3501 8.21758 4.73425 25.8749 1.28918 98.6062 5.328
Rh  3   18.8785 0.764252    14.1259 7.84438 3.32515 21.2487 -6.1989 -0.01036    11.8678
Rh  4   18.8545 0.760825    13.9806 7.62436 2.53464 19.3317 -5.6526 -0.0102 11.2835
Pd  0   19.3319 0.698655    15.5017 7.98929 5.29537 25.2052 0.605844    76.8986 5.26593
Pd  2   19.1701 0.696219    15.2096 7.55573 4.32234 22.5057 0   0   5.2916
Pd  4   19.2493 0.683839    14.79   7.14833 2.89289 17.9144 -7.9492 0.005127    13.0174
```

```
Ag  0   19.2808 0.6446  16.6885 7.4726  4.8045  24.6605 1.0463  99.8156 5.179
Ag  1   19.1812 0.646179    15.9719 7.19123 5.27475 21.7326 0.357534    66.1147 5.21572
Ag  2   19.1643 0.645643    16.2456 7.18544 4.3709  21.4072 0   0   5.21404
Cd  0   19.2214 0.5946  17.6444 6.9089  4.461   24.7008 1.6029  87.4825 5.0694
Cd  2   19.1514 0.597922    17.2535 6.80639 4.47128 20.2521 0   0   5.11937
In  0   19.1624 0.5476  18.5596 6.3776  4.2948  25.8499 2.0396  92.8029 4.9391
In  3   19.1045 0.551522    18.1108 6.3247  3.78897 17.3595 0   0   4.99635
Sn  0   19.1889 5.8303  19.1005 0.5031  4.4585  26.8909 2.4663  83.9571 4.7821
Sn  2   19.1094 0.5036  19.0548 5.8378  4.5648  23.3752 0.487   62.2061 4.7861
Sn  4   18.9333 5.764   19.7131 0.4655  3.4182  14.0049 0.0193  -0.7583 3.9182
Sb  0   19.6418 5.3034  19.0455 0.4607  5.0371  27.9074 2.6827  75.2825 4.5909
Sb  3   18.9755 0.467196    18.933  5.22126 5.10789 19.5902 0.288753    55.5113 4.69626
Sb  5   19.8685 5.44853 19.0302 0.467973    2.41253 14.1259 0   0   4.69263
Te  0   19.9644 4.81742 19.0138 0.420885    6.14487 28.5284 2.5239  70.8403 4.352
I   0   20.1472 4.347   18.9949 0.3814  7.5138  27.766  2.2735  66.8776 4.0712
I   -1  20.2332 4.3579  18.997  0.3815  7.8069  29.5259 2.8868  84.9304 4.0714
Xe  0   20.2933 3.9282  19.0298 0.344   8.9767  26.4659 1.99    64.2658 3.7118
Cs  0   20.3892 3.569   19.1062 0.3107  10.662  24.3879 1.4953  213.904 3.3352
Cs  1   20.3524 3.552   19.1278 0.3086  10.2821 23.7128 0.9615  59.4565 3.2791
Ba  0   20.3361 3.216   19.297  0.2756  10.888  20.2073 2.6959  167.202 2.7731
Ba  2   20.1807 3.21367 19.1136 0.28331 10.9054 20.0558 0.77634 51.746  3.02902
La  0   20.578  2.94817 19.599  0.244475    11.3727 18.7726 3.28719 133.124 2.14678
La  3   20.2489 2.9207  19.3763 0.250698    11.6323 17.8211 0.336048    54.9453 2.4086
Ce  0   21.1671 2.81219 19.7695 0.226836    11.8513 17.6083 3.33049 127.113 1.86264
Ce  3   20.8036 2.77691 19.559  0.23154 11.9369 16.5408 0.612376    43.1692 2.09013
Ce  4   20.3235 2.65941 19.8186 0.21885 12.1233 15.7992 0.144583    62.2355 1.5918
Pr  0   22.044  2.77393 19.6697 0.222087    12.3856 16.7669 2.82428 143.644 2.0583
Pr  3   21.3727 2.6452  19.7491 0.214299    12.1329 15.323  0.97518 36.4065 1.77132
Pr  4   20.9413 2.54467 20.0539 0.202481    12.4668 14.8137 0.296689    45.4643 1.24285
Nd  0   22.6845 2.66248 19.6847 0.210628    12.774  15.885  2.85137 137.903 1.98486
Nd  3   21.961  2.52722 19.9339 0.199237    12.12   14.1783 1.51031 30.8717 1.47588
Pm  0   23.3405 2.5627  19.6095 0.202088    13.1235 15.1009 2.87516 132.721 2.02876
Pm  3   22.5527 2.4174  20.1108 0.185769    12.0671 13.1275 2.07492 27.4491 1.19499
Sm  0   24.0042 2.47274 19.4258 0.196451    13.4396 14.3996 2.89604 128.007 2.20963
Sm  3   23.1504 2.31641 20.2599 0.174081    11.9202 12.1571 2.71488 24.8242 0.954586
Eu  0   24.6274 2.3879  19.0886 0.1942  13.7603 13.7546 2.9227  123.174 2.5745
Eu  2   24.0063 2.27783 19.9504 0.17353 11.8034 11.6096 3.87243 26.5156 1.36389
Eu  3   23.7497 2.22258 20.3745 0.16394 11.8509 11.311  3.26503 22.9966 0.759344
Gd  0   25.0709 2.25341 19.0798 0.181951    13.8518 12.9331 3.54545 101.398 2.4196
Gd  3   24.3466 2.13553 20.4208 0.155525    11.8708 10.5782 3.7149  21.7029 0.645089
Tb  0   25.8976 2.24256 18.2185 0.196143    14.3167 12.6648 2.95354 115.362 3.58324
Tb  3   24.9559 2.05601 20.3271 0.149525    12.2471 10.0499 3.773   21.2773 0.691967
Dy  0   26.507  2.1802  17.6383 0.202172    14.5596 12.1899 2.96577 111.874 4.29728
Dy  3   25.5395 1.9804  20.2861 0.143384    11.9812 9.34972 4.50073 19.581  0.68969
Ho  0   26.9049 2.07051 17.294  0.19794 14.5583 11.4407 3.63837 92.6566 4.56796
Ho  3   26.1296 1.91072 20.0994 0.139358    11.9788 8.80018 4.93676 18.5908 0.852795
Er  0   27.6563 2.07356 16.4285 0.223545    14.9779 11.3604 2.98233 105.703 5.92046
Er  3   26.722  1.84659 19.7748 0.13729 12.1506 8.36225 5.17379 17.8974 1.17613
Tm  0   28.1819 2.02859 15.8851 0.238849    15.1542 10.9975 2.98706 102.961 6.75621
Tm  3   27.3083 1.78711 19.332  0.136974    12.3339 7.96778 5.38348 17.2922 1.63929
Yb  0   28.6641 1.9889  15.4345 0.257119    15.3087 10.6647 2.98963 100.417 7.56672
Yb  2   28.1209 1.78503 17.6817 0.15997 13.3335 8.18304 5.14657 20.39   3.70983
Yb  3   27.8917 1.73272 18.7614 0.13879 12.6072 7.64412 5.47647 16.8153 2.26001
Lu  0   28.9476 1.90182 15.2208 9.98519 15.1    0.261033    3.71601 84.3298 7.97628
Lu  3   28.4628 1.68216 18.121  0.142292    12.8429 7.33727 5.59415 16.3535 2.97573
Hf  0   29.144  1.83262 15.1726 9.5999  14.7586 0.275116    4.30013 72.029  8.58154
Hf  4   28.8131 1.59136 18.4601 0.128903    12.7285 6.76232 5.59927 14.0366 2.39699
Ta  0   29.2024 1.77333 15.2293 9.37046 14.5135 0.295977    4.76492 63.3644 9.24354
Ta  5   29.1587 1.50711 18.8407 0.116741    12.8268 6.31524 5.38695 12.4244 1.78555
W   0   29.0818 1.72029 15.43   9.2259  14.4327 0.321703    5.11982 57.056  9.8875
W   6   29.4936 1.42755 19.3763 0.104621    13.0544 5.93667 5.06412 11.1972 1.01074
Re  0   28.7621 1.67191 15.7189 9.09227 14.5564 0.3505  5.44174 52.0861 10.472
Os  0   28.1894 1.62903 16.155  8.97948 14.9305 0.382661    5.67589 48.1647 11.0005
Os  4   30.419  1.37113 15.2637 6.84706 14.7458 0.165191    5.06795 18.003  6.49804
Ir  0   27.3049 1.59279 16.7296 8.86553 15.6115 0.417916    5.83377 45.0011 11.4722
```

```
Ir  3   30.4156 1.34323 15.862  7.10909 13.6145 0.204633    5.82008 20.3254 8.27903
Ir  4   30.7058 1.30923 15.5512 6.71983 14.2326 0.167252    5.53672 17.4911 6.96824
Pt  0   27.0059 1.51293 17.7639 8.81174 15.7131 0.424593    5.7837  38.6103 11.6883
Pt  2   29.8429 1.32927 16.7224 7.38979 13.2153 0.263297    6.35234 22.9426 9.85329
Pt  4   30.9612 1.24813 15.9829 6.60834 13.7348 0.16864 5.92034 16.9392 7.39534
Au  0   16.8819 0.4611  18.5913 8.6216  25.5582 1.4826  5.86    36.3956 12.0658
Au  1   28.0109 1.35321 17.8204 7.7395  14.3359 0.356752    6.58077 26.4043 11.2299
Au  3   30.6886 1.2199  16.9029 6.82872 12.7801 0.212867    6.52354 18.659  9.0968
Hg  0   20.6809 0.545   19.0417 8.4484  21.6575 1.5729  5.9676  38.3246 12.6089
Hg  1   25.0853 1.39507 18.4973 7.65105 16.8883 0.443378    6.48216 28.2262 12.0205
Hg  2   29.5641 1.21152 18.06   7.05639 12.8374 0.284738    6.89912 20.7482 10.6268
Tl  0   27.5446 0.65515 19.1584 8.70751 15.538  1.96347 5.52593 45.8149 13.1746
Tl  1   21.3985 1.4711  20.4723 0.517394    18.7478 7.43463 6.82847 28.8482 12.5258
Tl  3   30.8695 1.1008  18.3481 6.53852 11.9328 0.219074    7.00574 17.2114 9.8027
Pb  0   31.0617 0.6902  13.0637 2.3576  18.442  8.618   5.9696  47.2579 13.4118
Pb  2   21.7886 1.3366  19.5682 0.488383    19.1406 6.7727  7.01107 23.8132 12.4734
Pb  4   32.1244 1.00566 18.8003 6.10926 12.0175 0.147041    6.96886 14.714  8.08428
Bi  0   33.3689 0.704   12.951  2.9238  16.5877 8.7937  6.4692  48.0093 13.5782
Bi  3   21.8053 1.2356  19.5026 6.24149 19.1053 0.469999    7.10295 20.3185 12.4711
Bi  5   33.5364 0.91654 25.0946 0.39042 19.2497 5.71414 6.91555 12.8285 -6.7994
Po  0   34.6726 0.700999    15.4733 3.55078 13.1138 9.55642 7.02588 47.0045 13.677
At  0   35.3163 0.68587 19.0211 3.97458 9.49887 11.3824 7.42518 45.4715 13.7108
Rn  0   35.5631 0.6631  21.2816 4.0691  8.0037  14.0422 7.4433  44.2473 13.6905
Fr  0   35.9299 0.646453    23.0547 4.17619 12.1439 23.1052 2.11253 150.645 13.7247
Ra  0   35.763  0.616341    22.9064 3.87135 12.4739 19.9887 3.21097 142.325 13.6211
Ra  2   35.215  0.604909    21.67   3.5767  7.91342 12.601  7.65078 29.8436 13.5431
Ac  0   35.6597 0.589092    23.1032 3.65155 12.5977 18.599  4.08655 117.02  13.5266
Ac  3   35.1736 0.579689    22.1112 3.41437 8.19216 12.9187 7.05545 25.9443 13.4637
Th  0   35.5645 0.563359    23.4219 3.46204 12.7473 17.8309 4.80703 99.1722 13.4314
Th  4   35.1007 0.555054    22.4418 3.24498 9.78554 13.4661 5.29444 23.9533 13.376
Pa  0   35.8847 0.547751    23.2948 3.41519 14.1891 16.9235 4.17287 105.251 13.4287
U   0   36.0228 0.5293  23.4128 3.3253  14.9491 16.0927 4.188   100.613 13.3966
U   3   35.5747 0.52048 22.5259 3.12293 12.2165 12.7148 5.37073 26.3394 13.3092
U   4   35.3715 0.516598    22.5326 3.05053 12.0291 12.5723 4.7984  23.4582 13.2671
U   6   34.8509 0.507079    22.7584 2.8903  14.0099 13.1767 1.21457 25.2017 13.1665
Np  0   36.1874 0.511929    23.5964 3.25396 15.6402 15.3622 4.1855  97.4908 13.3573
Np  3   35.7074 0.502322    22.613  3.03807 12.9898 12.1449 5.43227 25.4928 13.2544
Np  4   35.5103 0.498626    22.5787 2.96627 12.7766 11.9484 4.92159 22.7502 13.2116
Np  6   35.0136 0.48981 22.7286 2.81099 14.3884 12.33   1.75669 22.6581 13.113
Pu  0   36.5254 0.499384    23.8083 3.26371 16.7707 14.9455 3.47947 105.98  13.3812
Pu  3   35.84   0.484938    22.7169 2.96118 13.5807 11.5331 5.66016 24.3992 13.1991
Pu  4   35.6493 0.481422    22.646  2.8902  13.3595 11.316  5.18831 21.8301 13.1555
Pu  6   35.1736 0.473204    22.7181 2.73848 14.7635 11.553  2.28678 20.9303 13.0582
Am  0   36.6706 0.483629    24.0992 3.20647 17.3415 14.3136 3.49331 102.273 13.3592
Cm  0   36.6488 0.465154    24.4096 3.08997 17.399  13.4346 4.21665 88.4834 13.2887
Bk  0   36.7881 0.451018    24.7736 3.04619 17.8919 12.8946 4.23284 86.003  13.2754
Cf  0   36.9185 0.437533    25.1995 3.00775 18.3317 12.4044 4.24391 83.7881 13.2674
```

8. BIBLIOGRAPHY

(1) Tan, M. X.; Laibinis, P. E.; Nguyen, S. T.; Kesselman, J. M.; Stanton, C. E.; Lewis, N. S. In *Progress in Inorganic Chemistry Vol. 41*; Wiley: 1994; Vol. 41, p 21-145.
(2) Kittel, C. *Introduction to Solid State Physics*; John Wiley & Sons: Berkeley, CA, 2004.
(3) Tritt, T. M. *Annu. Rev. Mater. Res.* **2011**, *41*, 433-448.
(4) Seddon, A. B. *J. Non-Cryst. Solids* **1995**, *184*, 44-50.
(5) Khaselev, O.; Turner, J. A. *Science* **1998**, *280*, 425-427.
(6) Minh, N. Q. *J. Am. Ceram. Soc.* **1993**, *76*, 563-588.
(7) Niederberger, M.; Pinna, N. *Metal Oxide Nanoparticles in Organic Solvents*; Springer: London, 2009.
(8) Schwarz, J. A.; Contescu, C.; Contescu, A. *Chem. Rev.* **1995**, *95*, 477-510.
(9) Braun, J. H.; Baidins, A.; Marganski, R. E. *Prog. Org. Coat.* **1992**, *20*, 105-138.
(10) Braun, J. H. *J. Coat. Technol.* **1997**, *69*, 59-72.
(11) Jun, Y.-W.; Choi, J.-S.; Cheon, J. *Angew. Chem., Int. Ed.* **2006**, *45*, 3414-39.
(12) O'Regan, B.; Grätzel, M. *Nature* **1991**, *353*, 737-740.
(13) Eranna, G.; Joshi, B. C.; Runthala, D. P.; Gupta, R. P. *Crit. Rev. Solid State Mater. Sci.* **2004**, *29*, 111-188.
(14) Granqvist, C. G. *Sol. Energy Mater. Sol. Cells* **2011**, *99*, 1-13.
(15) Whittingham, M. S. *Chem. Rev.* **2004**, *104*, 4271-301.
(16) Ohtani, B.; Prieto-Mahaney, O. O.; Li, D.; Abe, R. *J. Photochem. Photobiol., A* **2010**, *216*, 179-182.
(17) Hurum, D. C.; Agrios, A. G.; Gray, K. A.; Rajh, T.; Thurnauer, M. C. *J. Phys. Chem. B* **2003**, *107*, 4545-4549.
(18) Hench, L. L.; West, J. K. *Chem. Rev.* **1990**, *90*, 33-72.
(19) Livage, J.; Henry, M.; Sanchez, C. *Prog. Solid State Chem.* **1988**, *18*, 259-341.
(20) Cushing, B. L.; Kolesnichenko, V. L.; O'Connor, C. J. *Chem. Rev.* **2004**, *104*, 3893-946.
(21) Rajamathi, M.; Seshadri, R. *Curr. Opin. Solid State Mater. Sci.* **2002**, *6*, 337-345.
(22) Vioux, A. *Chem. Mater.* **1997**, *9*, 2292-2299.
(23) Niederberger, M. *Acc. Chem. Res.* **2007**, *40*, 793-800.
(24) Murray, C. B.; Norris, D. J.; Bawendi, M. G. *J. Am. Chem. Soc.* **1993**, *115*, 8706-8715.
(25) Jun, Y.-w.; Choi, J.-s.; Cheon, J. *Angew. Chem., Int. Ed.* **2006**, *45*, 3414-39.

(26) Park, J.; Joo, J.; Kwon, S. G.; Jang, Y.; Hyeon, T. *Angew. Chem., Int. Ed.* **2007**, *46*, 4630-4660.
(27) Murray, C. B.; Kagan, C. R.; Bawendi, M. G. *Annu. Rev. Mater. Sci.* **2000**, *30*, 545-610.
(28) Murray, C. B.; Sun, S.; Gaschler, W.; Doyle, H.; Betley, T. A.; Kagan, C. R. *IBM J. Res. Devel.* **2001**, *45*, 47-56.
(29) Sun, S.; Murray, C. B. *J. Appl. Phys.* **1999**, *85*, 4325-4325.
(30) Sun, S.; Murray, C. B.; Weller, D.; Folks, L.; Moser, A. *Science* **2000**, *287*, 1989-1992.
(31) Trentler, T. J.; Denler, T. E.; Bertone, J. F.; Agrawal, A.; Colvin, V. L. *J. Am. Chem. Soc.* **1999**, *121*, 1613-1614.
(32) Rockenberger, J.; Scher, E. C.; Alivisatos, A. P. *J. Am. Chem. Soc.* **1999**, *121*, 11595-11596.
(33) Hyeon, T.; Lee, S. S.; Park, J.; Chung, Y.; Na, H. B. *J. Am. Chem. Soc.* **2001**, *123*, 12798-801.
(34) Micic, O. I.; Sprague, J. R.; Curtis, C. J.; Jones, K. M.; Machol, J. L.; Nozik, A. J.; Giessen, H.; Fluegel, B.; Mohs, G.; Peyghambarian, N. *J. Phys. Chem.* **1995**, *99*, 7754-7759.
(35) Henkes, A. E.; Vasquez, Y.; Schaak, R. E. *J. Am. Chem. Soc.* **2007**, *129*, 1896-7.
(36) Miao, S.; Hickey, S. G.; Waurisch, C.; Lesnyak, V.; Otto, T.; Rellinghaus, B.; Eychmueller, A. *ACS Nano* **2012**, *6*, 7059-65.
(37) Zhang, Y.-W.; Sun, X.; Si, R.; You, L.-P.; Yan, C.-H. *J. Am. Chem. Soc.* **2005**, *127*, 3260-1.
(38) Ye, X.; Collins, J. E.; Kang, Y.; Chen, J.; Chen, D. T. N.; Yodh, A. G.; Murray, C. B. *Proc. Nat. Acad. Sci.* **2010**, *107*, 22430-5.
(39) Paik, T.; Ko, D.-K.; Gordon, T. R.; Doan-Nguyen, V.; Murray, C. B. *ACS Nano* **2011**, *5*, 8322-30.
(40) O'Brien, S.; Brus, L.; Murray, C. B. *J. Am. Chem. Soc.* **2001**, *123*, 12085-12086.
(41) Sun, S.; Zeng, H.; Robinson, D. B.; Raoux, S.; Rice, P. M.; Wang, S. X.; Li, G. *J. Am. Chem. Soc.* **2004**, *126*, 273-9.
(42) Koo, B.; Patel, R. N.; Korgel, B. A. *J. Am. Chem. Soc.* **2009**, *131*, 3134-5.
(43) Park, J.; Kang, E.; Bae, C. J.; Park, J.-G.; Noh, H.-J.; Kim, J.-Y.; Park, J.-H.; Park, H. M.; Hyeon, T. *J. Phys. Chem. B* **2004**, *108*, 13594-13598.
(44) Joo, J.; Yu, T.; Kim, Y. W.; Park, H. M.; Wu, F.; Zhang, J. Z.; Hyeon, T. *J. Am. Chem. Soc.* **2003**, *125*, 6553-7.
(45) Park, J.; An, K.; Hwang, Y.; Park, J.-G.; Noh, H.-J.; Kim, J.-Y.; Park, J.-H.; Hwang, N.-M.; Hyeon, T. *Nature Mater.* **2004**, *3*, 891-5.
(46) Choi, S.-H.; Kim, E.-G.; Park, J.; An, K.; Lee, N.; Kim, S. C.; Hyeon, T. *J. Phys. Chem. B* **2005**, *109*, 14792-4.

(47) Joo, J.; Kwon, S. G.; Yu, T.; Cho, M.; Lee, J.; Yoon, J.; Hyeon, T. *J. Phys. Chem. B* **2005**, *109*, 15297-302.
(48) Yu, T.; Joo, J.; Park, Y. I.; Hyeon, T. *Angew. Chem., Int. Ed.* **2005**, *44*, 7411-4.
(49) Kwon, S. G.; Piao, Y.; Park, J.-G. J.; Angappane, S.; Jo, Y.; Hwang, N.-M.; Hyeon, T. *J. Am. Chem. Soc.* **2007**, *129*, 12571-84.
(50) Jana, N. R.; Gearheart, L.; Murphy, C. J. *Chem. Commun.* **2001**, 617-618.
(51) Yu, H.; Gibbons, P. C.; Kelton, K. F.; Buhro, W. E. *J. Am. Chem. Soc.* **2001**, *123*, 9198-9199.
(52) Park, J.; Lee, E.; Hwang, N.-M.; Kang, M.; Kim, S. C.; Hwang, Y.; Park, J.-G.; Noh, H.-J.; Kim, J.-Y.; Park, J.-H.; Hyeon, T. *Angew. Chem., Int. Ed.* **2005**, *44*, 2873-7.
(53) McBride, J.; Treadway, J.; Feldman, L. C.; Pennycook, S. J.; Rosenthal, S. J. *Nano Lett.* **2006**, *6*, 1496-501.
(54) Kim, B. H.; Lee, N.; Kim, H.; An, K.; Park, Y. I.; Choi, Y.; Shin, K.; Lee, Y.; Kwon, S. G.; Na, H. B.; Park, J.-G.; Ahn, T.-Y.; Kim, Y.-W.; Moon, W. K.; Choi, S. H.; Hyeon, T. *J. Am. Chem. Soc.* **2011**.
(55) Kamplain, J. W.; Zhu, Z. (QD VISION INC (QDVI-Non-standard)). Preparing semiconductor nanocrystals e.g. arsenic, involves adding precursor mixture comprising cation/anion precursors, and amines to ligand mixture including acid, phenol, and solvent to form reaction mixture and heating the mixture. U.S. Patent WO2012099653-A2, July, 26 2012.
(56) Radu, D. R.; Caspar, J. V.; Johnson, L. K.; Rosenfeld, H. D.; Malajovich, I.; Lu, M.; Caspar, J.; Johnson, L.; Rosenfeld, H. (E. I. Du Pont De Nemours & Co.). Quaternary nanoparticle used in ink and for forming thin films for electronic devices, comprises copper, zinc, tin, chalcogen, and capping agent. WO2010135622-A1; TW201107241-A; US2012055554-A1; EP2432842-A1; KR2012028933-A; CN102439098-A, Mar 28, 2012.
(57) Hyeon, T. H.; Kim, B. H.; Lee, N. H.; Kim, E. G.; Jeon, B. S.; Kwon, E. B.; Park, J. Y.; Myeong, W. J.; Hyeon, T.; Lee, N. (HANWHA CHEM CORP.). Preparing iron oxide nanoparticles used in magnetic resonance imaging T1 contrast agent for cell staining, and diagnosing and treating diseases, involves reacting iron complex, fatty acid, and aliphatic alcohol or aliphatic amine. U.S. Patent WO2012018240-A2, Feb, 9 2012.
(58) Herrmann, J.-M.; Disdier, J.; Pichat, P. *Chem. Phys. Lett.* **1984**, *108*, 618-622.
(59) Moser, J.; Grätzel, M.; Gallay, R. *Helv. Chim. Acta* **1987**, *70*, 1596-1604.
(60) Maruska, H. P.; Ghosh, A. K. *Sol. Energy Mater.* **1979**, *1*, 237-247.
(61) Choi, W.; Termin, A.; Hoffmann, M. R. *J. Phys. Chem.* **1994**, *98*, 13669-13679.
(62) Asahi, R.; Morikawa, T.; Ohwaki, T.; Aoki, K.; Taga, Y. *Science* **2001**, *293*, 269-71.

(63) Gombac, V.; Derogatis, L.; Gasparotto, A.; Vicario, G.; Montini, T.; Barreca, D.; Balducci, G.; Fornasiero, P.; Tondello, E.; Graziani, M. *Chem. Phys.* **2007**, *339*, 111-123.
(64) Li, D.; Haneda, H.; Labhsetwar, N.; Hishita, S.; Ohashi, N. *Chem. Phys. Lett.* **2005**, *401*, 579-584.
(65) Gasparotto, A.; Barreca, D.; Bekermann, D.; Devi, A.; Fischer, R. A.; Fornasiero, P.; Gombac, V.; Lebedev, O. I.; Maccato, C.; Montini, T.; Van Tendeloo, G.; Tondello, E. *J. Am. Chem. Soc.* **2011**, *133*, 19362-5.
(66) Umebayashi, T.; Yamaki, T.; Itoh, H.; Asai, K. *Appl. Phys. Lett.* **2002**, *81*, 454-454.
(67) Shaban, Y. A.; Khan, S. U. M. *Int. J. Hydrogen Energy* **2008**, *33*, 1118-1126.
(68) Serpone, N. *J. Phys. Chem. B* **2006**, *110*, 24287-93.
(69) Bryan, J. D.; Gamelin, D. R. In *Progress in Inorganic Chemistry, Volume 54*; John Wiley & Sons, Inc.: Hoboken, NJ, USA, 2005; Vol. 54, p 47-126.
(70) Bailey, R. E.; Nie, S. *J. Am. Chem. Soc.* **2003**, *125*, 7100-6.
(71) Norris, D. J.; Efros, A. L.; Erwin, S. C. *Science* **2008**, *319*, 1776-9.
(72) Sun, S.; Fullerton, E. E.; Weller, D.; Murray, C. B. *IEEE Trans. Magn.* **2001**, *37*, 1239-1243.
(73) Zeng, H.; Sun, S.; Sandstrom, R. L.; Murray, C. B. *J. Magn. Magn. Mater.* **2003**, *266*, 227-232.
(74) Kang, Y.; Murray, C. B. *J. Am. Chem. Soc.* **2010**, *132*, 7568-9.
(75) Yang, Y.; Jin, Y.; He, H.; Wang, Q.; Tu, Y.; Lu, H.; Ye, Z. *J. Am. Chem. Soc.* **2010**, *132*, 13381-94.
(76) Fujishima, A.; Honda, K. *Nature* **1972**, *238*, 37-38.
(77) Wu, J. C. S.; Lin, H.-M. *Intl. J. Photoen.* **2005**, *7*, 115-119.
(78) Magnuson, A.; Anderlund, M.; Johansson, O.; Lindblad, P.; Lomoth, R.; Polivka, T.; Ott, S.; Stensjö, K.; Styring, S.; Sundström, V.; Hammarström, L. *Acc. Chem. Res.* **2009**, *42*, 1899-909.
(79) Kaneko, M.; Okura, I. *Photocatalysis: Science and Technology*; Springer: New York, 2003.
(80) Carp, O.; Huisman, C. L.; Reller, A. *Prog. Solid State Chem.* **2004**, *32*, 33-177.
(81) Barreca, D.; Carraro, G.; Gombac, V.; Gasparotto, A.; Maccato, C.; Fornasiero, P.; Tondello, E. *Adv. Funct. Mater.* **2011**, *21*, 2611-2623.
(82) Cargnello, M.; Gasparotto, A.; Gombac, V.; Montini, T.; Barreca, D.; Fornasiero, P. *Eur. J. Inorg. Chem.* **2011**, *2011*, 4309-4323.
(83) Fox, M. A.; Dulay, M. T. *Chem. Rev.* **1993**, *93*, 341-357.
(84) Bowker, M.; Davies, P. R.; Al-Mazroai, L. S. *Catal. Lett.* **2008**, *128*, 253-255.
(85) Daskalaki, V. M.; Kondarides, D. I. *Catal. Today* **2009**, *144*, 75-80.
(86) Kim, J.; Choi, W. *Energ. Environ. Sci.* **2010**, *3*, 1042-1042.

(87) Linsebigler, A. L.; Lu, G.; Yates, J. T. *Chem. Rev.* **1995**, *95*, 735-758.
(88) Youngblood, W. J.; Lee, S.-h. A.; Kobayashi, Y.; Hernandez-Pagan, E. A.; Hoertz, P. G.; Moore, T. A.; Moore, A. L.; Gust, D.; Mallouk, T. E. *J. Am. Chem. Soc.* **2009**, *131*, 926-7.
(89) Steinmiller, E. M. P.; Choi, K.-S. *Proc. Nat. Acad. Sci.* **2009**, *106*.
(90) Maeda, K.; Domen, K. *J. Phys. Chem. Lett.* **2010**, 100826161650057-2661.
(91) Thompson, T. L.; Yates, J. T. *Chem. Rev.* **2006**, *106*, 4428-53.
(92) Bratlie, K. M.; Lee, H.; Komvopoulos, K.; Yang, P.; Somorjai, G. A. *Nano Lett.* **2007**, *7*, 3097-101.
(93) Lee, I.; Delbecq, F. o.; Morales, R.; Albiter, M. a.; Zaera, F. *Nature Mater.* **2009**, *8*, 132-8.
(94) Xia, Y.; Xiong, Y.; Lim, B.; Skrabalak, S. E. *Angew. Chem., Int. Ed.* **2009**, *48*, 60-103.
(95) Kang, Y.; Ye, X.; Murray, C. B. *Angew. Chem., Int. Ed.* **2010**, *49*, 6156-9.
(96) Yamada, Y.; Tsung, C.-K.; Huang, W.; Huo, Z.; Habas, S. E.; Soejima, T.; Aliaga, C. E.; Somorjai, G. A.; Yang, P. *Nat. Chem.* **2011**, *0871*, 1-5.
(97) Limpijumnong, S.; Zhang, S.; Wei, S.-H.; Park, C. *Phys. Rev. Lett.* **2004**, *92*, 1-4.
(98) Nozik, A. *Phys. Rev. B* **1972**, *6*, 453-459.
(99) Yan, M.; Lane, M.; Kannewurf, C. R.; Chang, R. P. H. *Appl. Phys. Lett.* **2001**, *78*, 2342-2342.
(100) Asahi, R.; Wang, A.; Babcock, J. R.; Edleman, N. L.; Metz, A. W.; Lane, M. A.; Dravid, V. P.; Kannewurf, C. R.; Freeman, A. J.; Marks, T. J. *Thin Solid Films* **2002**, *411*, 101-105.
(101) Kammler, D. R.; Mason, T. O.; Young, D. L.; Coutts, T. J.; Ko, D.; Poeppelmeier, K. R.; Williamson, D. L. *J. Appl. Phys.* **2001**, *90*, 5979-5979.
(102) Wang, A.; Babcock, J. R.; Edleman, N. L.; Metz, A. W.; Lane, M. A.; Asahi, R.; Dravid, V. P.; Kannewurf, C. R.; Freeman, A. J.; Marks, T. J. *Proc. Nat. Acad. Sci.* **2001**, *98*, 7113-6.
(103) Ba, J.; Fattakhova Rohlfing, D.; Feldhoff, A.; Brezesinski, T.; Djerdj, I.; Wark, M.; Niederberger, M. *Chem. Mater.* **2006**, *18*, 2848-2854.
(104) Al-Dahoudi, N.; Aegerter, M. A. *J. Sol-Gel Sci. Technol.* **2003**, *26*, 693-697.
(105) Ederth, J.; Johnsson, P.; Niklasson, G.; Hoel, A.; Hultåker, A.; Heszler, P.; Granqvist, C.; van Doorn, A.; Jongerius, M.; Burgard, D. *Phys. Rev. B* **2003**, *68*, 1-10.
(106) Goebbert, C.; Nonninger, R.; Aegerter, M. A.; Schmidt, H. *Thin Solid Films* **1999**, *351*, 79-84.
(107) Choi, S.-I.; Nam, K. M.; Park, B. K.; Seo, W. S.; Park, J. T. *Chem. Mater.* **2008**, *20*, 2609-2611.

(108) Kanehara, M.; Koike, H.; Yoshinaga, T.; Teranishi, T. *J. Am. Chem. Soc.* **2009**, *131*, 17736-7.
(109) Yarema, M.; Pichler, S.; Kriegner, D.; Stangl, J.; Yarema, O.; Kirchschlager, R.; Tollabimazraehno, S.; Humer, M.; Haringer, D.; Kohl, M.; Chen, G.; Heiss, W. *ACS Nano* **2012**, *6*, 4113-21.
(110) Müller, V.; Rasp, M.; Štefanić, G.; Ba, J.; Günther, S.; Rathousky, J.; Niederberger, M.; Fattakhova-Rohlfing, D. *Chem. Mater.* **2009**, *21*, 5229-5236.
(111) Buonsanti, R.; Llordes, A.; Aloni, S.; Helms, B. A.; Milliron, D. J. *Nano Lett.* **2011**, *11*, 4706-10.
(112) Wang, Q. L.; Yang, Y. F.; He, H. P.; Chen, D. D.; Ye, Z. Z.; Jin, Y. Z. *Nanoscale Res. Lett.* **2010**, *5*, 882-888.
(113) Ba, J.; Rohlfing, D. F.; Feldhoff, A.; Brezesinski, T.; Djerdj, I.; Wark, M.; Niederberger, M. *Chem. Mater.* **2006**, *18*, 2848-2854.
(114) Lee, J.; Lee, S.; Li, G.; Petruska, M. A.; Paine, D. C.; Sun, S. *J. Am. Chem. Soc.* **2012**, *134*, 13410-4.
(115) Link, S.; El-Sayed, M. A. *J. Phys. Chem. B* **1999**, *103*, 8410-8426.
(116) Manthiram, K.; Alivisatos, A. P. *J. Am. Chem. Soc.* **2012**, *134*, 3995-3998.
(117) Liu, Y.; Zhang, X. *Chem. Soc. Rev.* **2011**, *40*, 2494-507.
(118) Shelby, R. A.; Smith, D. R.; Schultz, S. *Science* **2001**, *292*, 77-9.
(119) Boltasseva, A.; Shalaev, V. M. *Metamaterials* **2008**, *2*, 1-17.
(120) Shalaev, V. M. *Nature Photon.* **2007**, *1*, 41-48.
(121) Naik, G. V.; Boltasseva, A. *Phys. Status Solidi RRL* **2010**, *4*, 295-297.
(122) Naik, G. V.; Liu, J.; Kildishev, A. V.; Shalaev, V. M.; Boltasseva, A. *Proc. Nat. Acad. Sci.* **2012**, *109*, 8834-8.
(123) Klar, T. A.; Kildishev, A. V.; Drachev, V. P.; Shalaev, V. M. *IEEE J. Quantum Electron.* **2006**, *12*, 1106-1115.
(124) Yoshida, H.; Kuwauchi, Y.; Jinschek, J. R.; Sun, K.; Tanaka, S.; Kohyama, M.; Shimada, S.; Haruta, M.; Takeda, S. *Science* **2012**, *335*, 317-319.
(125) Diociaiuti, M. *J. Electron. Spectrosc. Relat. Phenom.* **2005**, *143*, 189-203.
(126) Williams, D. B.; Carter, C. B. *Transmission Electron Microscopy*; 2nd ed.; Springer: New York, 2009.
(127) Chu, B.; Hsiao, B. S. *Chem. Rev.* **2001**, *101*, 1727-61.
(128) Svergun, D. I.; Petoukhov, M. V.; Koch, M. H. *Biophys. J.* **2001**, *80*, 2946-53.
(129) Brown, P. J.; Fox, A. G.; Maslen, E. N.; O'Keefe, M. A.; Willis, B. T. M. In *International Tables for Crystallography*; John Wiley & Sons, Ltd: 2006; Vol. C.
(130) Hall, B. D.; Monot, R. *Comput. Phys.* **1991**, *5*, 414-414.
(131) U. S. Geological Survey, Mineral commodity summaries 2011: U.S. Geological Survey, 2011, p. 172.
(132) Chen, X.; Mao, S. S. *Chem. Rev.* **2007**, *107*, 2891-959.

(133) Fujishima, A.; Zhang, X.; Tryk, D. A. *Surf. Sci. Rep.* **2008**, *63*, 515-582.
(134) Chen, X.; Shen, S.; Guo, L.; Mao, S. S. *Chem. Rev.* **2010**, *110*, 6503-70.
(135) Diebold, U. *Surf. Sci. Rep.* **2003**, *48*, 53-229.
(136) Kandiel, T. A.; Feldhoff, A.; Robben, L.; Dillert, R.; Bahnemann, D. W. *Chem. Mater.* **2010**, *22*, 2050-2060.
(137) Murray, C. B.; Sun, S.; Doyle, H.; Betley, T. *MRS Bull.* **2012**, *26*, 985-991.
(138) Ahmadi, T. S.; Wang, Z. L.; Green, T. C.; Henglein, A.; El-Sayed, M. A. *Science* **1996**, *272*, 1924-6.
(139) Burda, C.; Chen, X.; Narayanan, R.; El-Sayed, M. A. *Chem. Rev.* **2005**, *105*, 1025-102.
(140) Lee, I.; Delbecq, F.; Morales, R.; Albiter, M. A.; Zaera, F. *Nature Mater.* **2009**, *8*, 132-8.
(141) Comparelli, R.; Fanizza, E.; Curri, M. L.; Cozzoli, P. D.; Mascolo, G.; Passino, R.; Agostiano, A. *Appl. Catal. B-Environ.* **2005**, *55*, 81-91.
(142) Dong, A.; Ye, X.; Chen, J.; Kang, Y.; Gordon, T.; Kikkawa, J. M.; Murray, C. B. *J. Am. Chem. Soc.* **2011**, *133*, 998-1006.
(143) Kuipers, E. W.; Laszlo, C.; Wieldraaijer, W. *Catal. Lett.* **1993**, *17*, 71-79.
(144) Jun, Y.-W.; Casula, M. F.; Sim, J.-H.; Kim, S. Y.; Cheon, J.; Alivisatos, A. P. *J. Am. Chem. Soc.* **2003**, *125*, 15981-5.
(145) Zhang, Z.; Zhong, X.; Liu, S.; Li, D.; Han, M. *Angew. Chem., Int. Ed.* **2005**, *44*, 3466-70.
(146) Koo, B.; Park, J.; Kim, Y.; Choi, S.-H.; Sung, Y.-E.; Hyeon, T. *J. Phys. Chem. B* **2006**, *110*, 24318-23.
(147) Buonsanti, R.; Grillo, V.; Carlino, E.; Giannini, C.; Kipp, T.; Cingolani, R.; Cozzoli, P. D. *J. Am. Chem. Soc.* **2008**, *130*, 11223-33.
(148) Dinh, C.-T.; Nguyen, T.-D.; Kleitz, F.; Do, T.-O. *ACS Nano* **2009**, *3*, 3737-43.
(149) Chen, C.; Hu, R.; Mai, K.; Ren, Z.; Wang, H.; Qian, G.; Wang, Z. *Cryst. Growth Des.* **2011**, *11*, 5221–5226.
(150) Buonsanti, R.; Carlino, E.; Giannini, C.; Altamura, D.; De Marco, L.; Giannuzzi, R.; Manca, M.; Gigli, G.; Cozzoli, P. D. *J. Am. Chem. Soc.* **2011**, *133*, 19216-39.
(151) Yang, H. G.; Sun, C. H.; Qiao, S. Z.; Zou, J.; Liu, G.; Smith, S. C.; Cheng, H. M.; Lu, G. Q. *Nature* **2008**, *453*, 638-41.
(152) Fang, W. Q.; Gong, X.-Q.; Yang, H. G. *J. Phys. Chem. Lett.* **2011**, *2*, 725-734.
(153) Liu, G.; Yu, J. C.; Lu, G. Q. M.; Cheng, H.-M. *Chem. Commun.* **2011**, *47*, 6763-83.
(154) Henderson, M. A. *Surf. Sci. Rep.* **2011**, *66*, 185-297.
(155) Lazzeri, M.; Vittadini, A.; Selloni, A. *Phys. Rev. B* **2001**, *63*, 1-9.
(156) Vittadini, A.; Selloni, A.; Rotzinger, F. P.; Grätzel, M. *Phys. Rev. Lett.* **1998**, *81*, 2954-2957.

(157) Gong, X. Q.; Selloni, A. *J. Phys. Chem. B* **2005**, *109*, 19560-19562.
(158) Yang, H. G.; Liu, G.; Qiao, S. Z.; Sun, C. H.; Jin, Y. G.; Smith, S. C.; Zou, J.; Cheng, H. M.; Lu, G. Q. M. *J. Am. Chem. Soc.* **2009**, *131*, 4078-83.
(159) Wu, B.; Guo, C.; Zheng, N.; Xie, Z.; Stucky, G. D. *J. Am. Chem. Soc.* **2008**, *130*, 17563-7.
(160) Han, X.; Kuang, Q.; Jin, M.; Xie, Z.; Zheng, L. *J. Am. Chem. Soc.* **2009**, *131*, 3152-3153.
(161) Liu, G.; Yang, H. G.; Wang, X.; Cheng, L.; Lu, H.; Wang, L.; Lu, G. Q.; Cheng, H.-m. *J. Phys. Chem. C* **2009**, *113*, 21784-21788.
(162) Dai, Y.; Cobley, C. M.; Zeng, J.; Sun, Y.; Xia, Y. *Nano Lett.* **2009**, *9*, 2455-9.
(163) Pan, J.; Liu, G.; Lu, G. Q. M.; Cheng, H.-M. *Angew. Chem., Int. Ed.* **2011**, *50*, 2133-7.
(164) Jiang, H. B.; Cuan, Q.; Wen, C. Z.; Xing, J.; Wu, D.; Gong, X.-Q.; Li, C.; Yang, H. G. *Angew. Chem., Int. Ed.* **2011**, *50*, 3764-3768.
(165) Tachikawa, T.; Yamashita, S.; Majima, T. *J. Am. Chem. Soc.* **2011**, *133*, 7197-204.
(166) D'Arienzo, M.; Carbajo, J.; Bahamonde, A.; Crippa, M.; Polizzi, S.; Scotti, R.; Wahba, L.; Morazzoni, F. *J. Am. Chem. Soc.* **2011**, *133*, 17652-61.
(167) Wu, X.; Chen, Z.; Lu, G. Q. M.; Wang, L. *Adv. Funct. Mater.* **2011**, *21*, 4167–4172.
(168) Jana, N. R.; Gearheart, L.; Murphy, C. J. *Chem. Mater.* **2001**, *13*, 2313-2322.
(169) Minella, M.; Faga, M. G.; Maurino, V.; Minero, C.; Pelizzetti, E.; Coluccia, S.; Martra, G. *Langmuir* **2010**, *26*, 2521-7.
(170) Mangolini, F.; Ahlund, J.; Wabiszewski, G. E.; Adiga, V. P.; Egberts, P.; Streller, F.; Backlund, K.; Karlsson, P. G.; Wannberg, B.; Carpick, R. W. *Rev. Sci. Instrum.* **2012**, *83*, 093112-10.
(171) Powell, C. J. In *Quantitative Surface Analysis of Materials*; McIntyre, N. S., Ed.; American Society for Testing and Materials: Philadelphia, 1978, p 5-30.
(172) Scofield, J. H. *J. Electron Spectrosc. Relat. Phenom.* **1976**, *8*, 129-137.
(173) Reilman, R. F.; Msezane, A.; Manson, S. T. *J. Electron. Spectrosc. Relat. Phenom.* **1976**, *8*, 389-394.
(174) Tanuma, S.; Powell, C. J.; Penn, D. R. *Surf. Interface Anal.* **1994**, *21*, 165-176.
(175) Alcock, N. W.; Brown, D. A.; Illson, T. F.; Roe, S. M.; Wallbridge, M. G. H. *J. Chem. Soc., Dalton Trans.* **1991**, 873-873.
(176) Barrow, H.; Brown, D. A.; Alcock, N. W.; Clase, H. J.; Wallbridge, M. G. H. *J. Chem. Soc., Dalton Trans.* **1994**, *1*, 195-195.
(177) Gindl, J.; Liu, F.-Q.; Noltemeyer, M.; Schmidt, H.-G.; Roesky, H. W. *Inorg. Chem.* **1995**, *34*, 5711-5714.

(178) Niederberger, M.; Bartl, M. H.; Stucky, G. D. *Chem. Mater.* **2002**, *14*, 4364-4370.
(179) Niederberger, M.; Garnweitner, G.; Ba, J.; Polleux, J.; Pinna, N. *Int. J. Nanotechnol.* **2007**, *4*, 263-263.
(180) Chen, Y.; Kim, M.; Lian, G.; Johnson, M. B.; Peng, X. *J. Am. Chem. Soc.* **2005**, *127*, 13331-7.
(181) Padmanabhan, S. C.; Pillai, S. C.; Colreavy, J.; Balakrishnan, S.; McCormack, D. E.; Perova, T. S.; Hinder, S. J.; Kelly, J. M. *Chem. Mater.* **2007**, *19*, 4474-4481.
(182) Lv, Y.; Yu, L.; Huang, H.; Liu, H.; Feng, Y. *Appl. Surf. Sci.* **2009**, *255*, 9548-9552.
(183) Shian, S.; Sandhage, K. H. *J. Appl. Crystallogr.* **2010**, *43*, 757-761.
(184) Vorres, K.; Donohue, J. *Acta Crystallograph.* **1955**, *8*, 25-26.
(185) Wen, C. Z.; Hu, Q. H.; Guo, Y. N.; Gong, X. Q.; Qiao, S. Z.; Yang, H. G. *Chem. Commun.* **2011**, *47*, 6138-40.
(186) Zhu, J.; Zhang, D.; Bian, Z.; Li, G.; Huo, Y.; Lu, Y.; Li, H. *Chem. Commun.* **2009**, 5394-6.
(187) Zeng, Y.; Zhang, W.; Xu, C.; Xiao, N.; Huang, Y.; Yu, D. Y. W.; Hng, H. H.; Yan, Q. *Chem. Eur. J.* **2012**, *18*, 4026-30.
(188) Selloni, A. *Nature Mater.* **2008**, *7*, 613-5.
(189) Swamy, V.; Menzies, D.; Muddle, B. C.; Kuznetsov, A.; Dubrovinsky, L. S.; Dai, Q.; Dmitriev, V. *Appl. Phys. Lett.* **2006**, *88*, 243103-243103.
(190) Ahmad, M. I.; Bhattacharya, S. S. *Appl. Phys. Lett.* **2009**, *95*, 191906-191906.
(191) Khomenko, V. M.; Langer, K.; Rager, H.; Fett, A. *Phys. Chem. Miner.* **1998**, *25*, 338-346.
(192) Liu, H.; Ma, H. T.; Li, X. Z.; Li, W. Z.; Wu, M.; Bao, X. H. *Chemosphere* **2003**, *50*, 39-46.
(193) Teleki, A.; Pratsinis, S. E. *Phys. Chem. Chem. Phys.* **2009**, *11*, 3742.
(194) Zuo, F.; Wang, L.; Wu, T.; Zhang, Z.; Borchardt, D.; Feng, P. *J. Am. Chem. Soc.* **2010**, *132*, 11856-7.
(195) Howe, R. F.; Grätzel, M. *J. Phys. Chem.* **1985**, *89*, 4495-4499.
(196) Howe, R. F.; Grätzel, M. *J. Phys. Chem.* **1987**, *91*, 3906-3909.
(197) Torimoto, T.; Fox, R. J.; Fox, M. A. *J. Electrochem. Soc.* **1996**, *143*, 3712-3717.
(198) Rajh, T.; Ostafin, A. E.; Micic, O. I.; Tiede, D. M.; Thurnauer, M. C. *J. Phys. Chem.* **1996**, *100*, 4538-4545.
(199) Livraghi, S.; Chiesa, M.; Paganini, M. C.; Giamello, E. *J. Phys. Chem. C* **2011**, *115*, 25413-25421.
(200) Berger, T.; Sterrer, M.; Diwald, O.; Knözinger, E.; Panayotov, D.; Thompson, T. L.; Yates, J. T., Jr. *J. Phys. Chem. B* **2005**, *109*, 6061-8.

(201) Prokes, S. M.; Gole, J. L.; Chen, X.; Burda, C.; Carlos, W. E. *Adv. Funct. Mater.* **2005**, *15*, 161-167.
(202) Zhang, S.; Li, W.; Jin, Z.; Yang, J.; Zhang, J.; Du, Z.; Zhang, Z. *J. Solid State Chem.* **2004**, *177*, 1365-1371.
(203) Li, L.; Li, G.; Xu, J.; Zheng, J.; Tong, W.; Hu, W. *Phys. Chem. Chem. Phys.* **2010**, 10857-10864.
(204) Rhodes, C.; Franzen, S.; Maria, J.-P.; Losego, M.; Leonard, D. N.; Laughlin, B.; Duscher, G.; Weibel, S. *J. Appl. Phys.* **2006**, *100*, 054905-054905.
(205) Khader, M. M.; Kheiri, F. M. N.; El-Anadouli, B. E.; Ateya, B. G. *J. Phys. Chem.* **1993**, *97*, 6074-6077.
(206) Seo, H.; Baker, L. R.; Hervier, A.; Kim, J.; Whitten, J. L.; Somorjai, G. A. *Nano Lett.* **2011**, *11*, 751-6.
(207) Czoska, A. M.; Livraghi, S.; Chiesa, M.; Giamello, E.; Agnoli, S.; Granozzi, G.; Finazzi, E.; Valentin, C. D.; Pacchioni, G. *J. Phys. Chem. C* **2008**, *112*, 8951-8956.
(208) Yu, J. C.; Yu, J.; Ho, W.; Jiang, Z.; Zhang, L. *Chem. Mater.* **2002**, *14*, 3808-3816.
(209) Todorova, N.; Giannakopoulou, T.; Vaimakis, T.; Trapalis, C. *Mater. Sci. Eng., B* **2008**, *152*, 50-54.
(210) Liu, G.; Yang, H. G.; Wang, X.; Cheng, L.; Pan, J.; Lu, G. Q. M.; Cheng, H.-M. *J. Am. Chem. Soc.* **2009**, *131*, 12868-9.
(211) Moss, J. H.; Parfitt, G. D.; Fright, A. *Colloid. Polym. Sci.* **1978**, *256*, 1121-1130.
(212) Kondarides, D. I.; Daskalaki, V. M.; Patsoura, A.; Verykios, X. E. *Catal. Lett.* **2007**, *122*, 26-32.
(213) Osterloh, F. E. *Chem. Mater.* **2008**, *20*, 35-54.
(214) Chen, X.; Liu, L.; Yu, P. Y.; Mao, S. S. *Science* **2011**, *746*, 746-50.
(215) Liu, G.; Sun, C.; Yang, H. G.; Smith, S. C.; Wang, L.; Lu, G. Q. M.; Cheng, H.-M. *Chem. Commun.* **2010**, *46*, 755-757.
(216) Chiarello, G. L.; Ferri, D.; Selli, E. *J. Catal.* **2011**, *280*, 168-177.
(217) Amano, F.; Prieto-Mahaney, O.-O.; Terada, Y.; Yasumoto, T.; Shibayama, T.; Ohtani, B. *Chem. Mater.* **2009**, *21*, 2601-2603.
(218) Yu, J.; Qi, L.; Jaroniec, M. *J. Phys. Chem. C* **2010**, *114*, 13118-13125.
(219) Montoya, J. F.; Salvador, P. *Appl. Catal. B-Environ.* **2010**, *94*, 97-107.
(220) Braslavsky, S. E.; Braun, A. M.; Cassano, A. E.; Emeline, A. V.; Litter, M. I.; Palmisano, L.; Parmon, V. N.; Serpone, N. *Pure Appl. Chem.* **2011**, *83*, 931-1014.
(221) Huo, Z.; Tsung, C.-K.; Huang, W.; Fardy, M.; Yan, R.; Zhang, X.; Li, Y.; Yang, P. *Nano Lett.* **2009**, *9*, 1260-4.
(222) Seo, J.-W.; Jun, Y.-W.; Ko, S. J.; Cheon, J. *J. Phys. Chem. B* **2005**, *109*, 5389-91.

(223) Baker, J. L.; Widmer-Cooper, A.; Toney, M. F.; Geissler, P. L.; Alivisatos, A. P. *Nano Lett.* **2010**, *10*, 195-201.
(224) Dong, A.; Chen, J.; Vora, P. M.; Kikkawa, J. M.; Murray, C. B. *Nature* **2010**, *466*, 474-477.
(225) Ye, B.; Qian, G.; Fan, X.; Wang, Z. *Curr. Nanosci.* **2010**, *7*, 262-268.
(226) Oosawa, F.; Asakura, S. *J. Chem. Phys.* **1954**, *22*, 1255-1255.
(227) Baranov, D.; Fiore, A.; van Huis, M.; Giannini, C.; Falqui, A.; Lafont, U.; Zandbergen, H.; Zanella, M.; Cingolani, R.; Manna, L. *Nano Lett.* **2010**, *10*, 743-9.
(228) Bishop, K. J. M.; Wilmer, C. E.; Soh, S.; Grzybowski, B. A. *Small* **2009**, *5*, 1600-30.
(229) Min, Y.; Akbulut, M.; Kristiansen, K.; Golan, Y.; Israelachvili, J. *Nature Mater.* **2008**, *7*, 527-38.
(230) Zanella, M.; Bertoni, G.; Franchini, I. R.; Brescia, R.; Baranov, D.; Manna, L. *Chem. Commun.* **2011**, *47*, 203-5.
(231) Chang, H.; Su, C.; Lo, C.-H.; Chen, L.-C.; Tsung, T.-T.; Jwo, C.-S. *Mater. Trans.* **2004**, *45*, 3334-3337.
(232) Wu, C.-H.; Chern, J.-M. *Ind. Eng. Chem. Res.* **2006**, *45*, 6450-6457.
(233) Kominami, H.; Ishii, Y.; Kohno, M.; Konishi, S. *Catal. Lett.* **2003**, *91*, 41-47.
(234) Tomita, K.; Petrykin, V.; Kobayashi, M.; Shiro, M.; Yoshimura, M.; Kakihana, M. *Angew. Chem., Int. Ed.* **2006**, *45*, 2378-81.
(235) Kobayashi, M.; Tomita, K.; Petrykin, V.; Yoshimura, M.; Kakihana, M. *J. Mater. Sci.* **2007**, *43*, 2158-2162.
(236) Katsumata, K.-I.; Ohno, Y.; Tomita, K.; Taniguchi, T.; Matsushita, N.; Okada, K. *ACS Appl. Mater. Interfaces* **2012**, *4*, 4846.
(237) Kandiel, T. A.; Robben, L.; Alkaim, A.; Bahnemann, D. *Photochem. Photobiol. Sci.* **2012**.
(238) Buonsanti, R.; Grillo, V.; Carlino, E.; Giannini, C.; Gozzo, F.; Garcia-Hernandez, M.; Garcia, M. A.; Cingolani, R.; Cozzoli, P. D. *J. Am. Chem. Soc.* **2010**, *132*, 2437-64.
(239) Buonsanti, R.; Snoeck, E.; Giannini, C.; Gozzo, F.; Garcia-Hernandez, M.; Angel Garcia, M.; Cingolani, R.; Cozzoli, P. D. *Phys. Chem. Chem. Phys.* **2009**, *11*, 3680-91.
(240) Fan, Z.; Lu, J. G. *J. Nanosci. Nanotechno.* **2005**, *5*, 1561-73.
(241) Wang, Z. L.; Song, J. *Science* **2006**, *312*, 242-6.
(242) Frenzel, H.; Lajn, A.; von Wenckstern, H.; Lorenz, M.; Schein, F.; Zhang, Z.; Grundmann, M. *Adv. Mater.* **2010**, *22*, 5332-49.
(243) Minami, T. *Semicond. Sci. Technol.* **2005**, *20*, S35-S44.
(244) Liu, X.-M.; Lu, G. Q.; Yan, Z.-F.; Beltramini, J. *Ind. Eng. Chem. Res.* **2003**, *42*, 6518-6530.
(245) Sakthivel, S.; Neppolian, B.; Shankar, M. V.; Arabindoo, B.; Palanichamy, M.; Murugesan, V. *Sol. Energy Mater. Sol. Cells* **2003**, *77*, 65-82.

(246) Koch, U.; Fojtik, A.; Weller, H.; Henglein, A. *Chem. Phys. Lett.* **1985**, *122*, 507-510.
(247) Pacholski, C.; Kornowski, A.; Weller, H. *Angew. Chem., Int. Ed.* **2002**, *41*, 1188-91.
(248) Yin, M.; Gu, Y.; Kuskovsky, I. L.; Andelman, T.; Zhu, Y.; Neumark, G. F.; O'Brien, S. *J. Am. Chem. Soc.* **2004**, *126*, 6206-7.
(249) Zhong, X.; Knoll, W. *Chem. Commun.* **2005**, 1158-60.
(250) Andelman, T.; Gong, Y.; Polking, M.; Yin, M.; Kuskovsky, I.; Neumark, G.; O'Brien, S. *J. Phys. Chem. B* **2005**, *109*, 14314-8.
(251) Kim, S. Y.; Lee, I. S.; Yeon, Y. S.; Park, S. M.; Song, J. K. *Bull. Korean Chem. Soc.* **2008**, *29*, 1960-1964.
(252) McLaren, A.; Valdes-Solis, T.; Li, G.; Tsang, S. C. *J. Am. Chem. Soc.* **2009**, *131*, 12540-1.
(253) Chen, Y.; Kim, M.; Lian, G.; Johnson, M. B.; Peng, X. *J. Am. Chem. Soc.* **2005**, *127*, 13331-7.
(254) Lee, H.-J.; Jeong, S.-Y.; Cho, C. R.; Park, C. H. *Appl. Phys. Lett.* **2002**, *81*, 4020-4020.
(255) Radovanovic, P. V.; Norberg, N. S.; McNally, K. E.; Gamelin, D. R. *J. Am. Chem. Soc.* **2002**, *124*, 15192-15193.
(256) Han, X.; Wang, G.; Wang, Q.; Cao, L.; Liu, R.; Zou, B.; Hou, J. G. *Appl. Phys. Lett.* **2005**, *86*, 223106-223106.
(257) Weakliem, H. A. *J. Chem. Phys.* **1962**, *36*, 2117-2117.
(258) Schwartz, D. A.; Norberg, N. S.; Nguyen, Q. P.; Parker, J. M.; Gamelin, D. R. *J. Am. Chem. Soc.* **2003**, *125*, 13205-18.
(259) Vanheusden, K.; Seager, C. H.; Warren, W. L.; Tallant, D. R.; Voigt, J. A. *Appl. Phys. Lett.* **1996**, *68*, 403-403.
(260) Zhang, L.; Yin, L.; Wang, C.; Lun, N.; Qi, Y.; Xiang, D. *J. Phys. Chem. C* **2010**, *114*, 9651-9658.
(261) Vandijken, A.; Meulenkamp, E.; Vanmaekelbergh, D.; Meijerink, A. *J. Lumin.* **2000**, *87-89*, 454-456.
(262) Greene, L. E.; Yuhas, B. D.; Law, M.; Zitoun, D.; Yang, P. *Inorg. Chem.* **2006**, *45*, 7535-43.
(263) Fu, Y.-S.; Du, X.-W.; Kulinich, S. A.; Qiu, J.-S.; Qin, W.-J.; Li, R.; Sun, J.; Liu, J. *J. Am. Chem. Soc.* **2007**.
(264) Fu, Y.-S.; Du, X.-W.; Kulinich, S. A.; Qiu, J.-S.; Qin, W.-J.; Li, R.; Sun, J.; Liu, J. *J. Am. Chem. Soc.* **2007**, *129*, 16029-33.
(265) Yin, Y.; Alivisatos, A. P. *Nature* **2005**, *437*, 664-70.
(266) Yang, Z.; Cavalier, M.; Walls, M.; Bonville, P.; Lisiecki, I.; Pileni, M.-P. *J. Phys. Chem. C* **2012**, *116*, 15723-15730.
(267) Murphy, C. J.; Sau, T. K.; Gole, A. M.; Orendorff, C. J.; Gao, J.; Gou, L.; Hunyadi, S. E.; Li, T. *J. Phys. Chem. B* **2005**, *109*, 13857-70.

(268) Lu, X.; Rycenga, M.; Skrabalak, S. E.; Wiley, B.; Xia, Y. *Annu. Rev. Phys. Chem.* **2009**, *60*, 167-92.
(269) Tao, A. R.; Habas, S.; Yang, P. *Small* **2008**, *4*, 310-325.
(270) Ye, X.; Jin, L.; Caglayan, H.; Chen, J.; Xing, G.; Zheng, C.; Doan-Nguyen, V.; Kang, Y.; Engheta, N.; Kagan, C. R.; Murray, C. B. *ACS Nano* **2012**, *6*, 2804-2817.
(271) Sanchez-Gaytan, B. L.; Swanglap, P.; Lamkin, T. J.; Hickey, R. J.; Fakhraai, Z.; Link, S.; Park, S.-J. *J. Phys. Chem. C* **2012**, *116*, 10318-10324.
(272) Nie, S.; Emory, S. R. *Science* **1997**, *275*, 1102-1106.
(273) Willets, K. a.; Van Duyne, R. P. *Annu. Rev. Phys. Chem.* **2007**, *58*, 267-97.
(274) Stewart, M. E.; Anderton, C. R.; Thompson, L. B.; Maria, J.; Gray, S. K.; Rogers, J. a.; Nuzzo, R. G. *Chem. Rev.* **2008**, *108*, 494-521.
(275) El-Sayed, I. H.; Huang, X.; El-Sayed, M. a. *Cancer letters* **2006**, *239*, 129-35.
(276) Jain, P. K.; Huang, X.; El-Sayed, I. H.; El-Sayed, M. a. *Acc. Chem. Res.* **2008**, *41*, 1578-86.
(277) Chen, Y.; Munechika, K.; Ginger, D. S. *Nano Lett.* **2007**, *7*, 690-696.
(278) Ming, T.; Chen, H.; Jiang, R.; Li, Q.; Wang, J. *J. Phys. Chem. Lett.* **2012**, *3*, 191-202.
(279) Saboktakin, M.; Ye, X.; Oh, S. J.; Hong, S.-H.; Fafarman, A. T.; Chettiar, U. K.; Engheta, N.; Murray, C. B.; Kagan, C. R. *ACS Nano* **2012**, *6*, 8758-66.
(280) Zhao, Y.; Pan, H.; Lou, Y.; Qiu, X.; Zhu, J.; Burda, C. *J. Am. Chem. Soc.* **2009**, *131*, 4253-61.
(281) Luther, J. M.; Jain, P. K.; Ewers, T.; Alivisatos, A. P. *Nature Mater.* **2011**, *10*, 361-366.
(282) West, P. R.; Ishii, S.; Naik, G. V.; Emani, N. K.; Shalaev, V. M.; Boltasseva, A. *Laser Photon. Rev.* **2010**, *4*, 795-808.
(283) Boltasseva, A.; Atwater, H. A. *Science* **2011**, *331*, 290-291.
(284) Hessel, C. M.; Pattani, V. P.; Rasch, M.; Panthani, M. G.; Koo, B.; Tunnell, J. W.; Korgel, B. A. *Nano Lett.* **2011**, *11*, 2560-6.
(285) Hsu, S.-W.; On, K.; Tao, A. R. *J. Am. Chem. Soc.* **2011**, *133*, 19072-5.
(286) Hsu, S.-W.; Bryks, W.; Tao, A. R. *Chem. Mater.* **2012**, *24*, 3765-3771.
(287) Coutts, T. J.; Young, D. L.; Li, X.; Mulligan, W. P.; Wu, X. *J. Vac. Sci. Technol., A* **2000**, *18*, 2646-2646.
(288) Wang, A.; Babcock, J. R.; Edleman, N. L.; Metz, A. W.; Lane, M. A.; Asahi, R.; Dravid, V. P.; Kannewurf, C. R.; Freeman, A. J.; Marks, T. J. *Proc. Nat. Acad. Sci.* **2001**, *98*, 7113-6.

(289) Jin, S.; Yang, Y.; Medvedeva, J. E.; Wang, L.; Li, S.; Cortes, N.; Ireland, J. R.; Metz, A. W.; Ni, J.; Hersam, M. C.; Freeman, A. J.; Marks, T. J. *Chem. Mater.* **2008**, *20*, 220-230.
(290) Yang, Y.; Jin, S.; Medvedeva, J. E.; Ireland, J. R.; Metz, A. W.; Ni, J.; Hersam, M. C.; Freeman, A. J.; Marks, T. J. *J. Am. Chem. Soc.* **2005**, *127*, 8796-804.
(291) Naik, G. V.; Kim, J.; Boltasseva, A. *Opt. Mater. Express* **2011**, *1*, 1090-1090.
(292) Choi, D.-H.; Jeong, G.-H.; Kim, S.-W. *Bull. Korean Chem. Soc.* **2011**, *32*, 3851-3852.
(293) Peng, Z. A.; Peng, X. *J. Am. Chem. Soc.* **2001**, *123*, 183-4.
(294) Kloper, V.; Osovsky, R.; Kolny-Olesiak, J.; Sashchiuk, A.; Lifshitz, E. *J. Phys. Chem. C* **2007**, *111*, 10336-10341.
(295) Shevchenko, E. V.; Talapin, D. V.; Schnablegger, H.; Kornowski, A.; Festin, O.; Svedlindh, P.; Haase, M.; Weller, H. *J. Am. Chem. Soc.* **2003**, *125*, 9090-101.
(296) Gordon, T. R.; Cargnello, M.; Paik, T.; Mangolini, F.; Weber, R. T.; Fornasiero, P.; Murray, C. B. *J. Am. Chem. Soc.* **2012**, *134*, 6751-6761.
(297) Burstein, E. *Phys. Rev.* **1954**, *93*, 632-633.
(298) Link, S.; El-Sayed, M. A. *J. Phys. Chem. B* **1999**, *103*, 8410-8426.
(299) Li, C.; Shuford, K. L.; Park, Q. H.; Cai, W.; Li, Y.; Lee, E. J.; Cho, S. O. *Angew. Chem., Int. Ed.* **2007**, *46*, 3264-8.
(300) Sonnichsen, C.; Franzl, T.; Wilk, T.; von Plessen, G.; Feldmann, J. *Phys. Rev. Lett.* **2002**, *88*, 1-4.
(301) Liu, X.; Atwater, M.; Wang, J.; Huo, Q. *Colloids Surf., B* **2007**, *58*, 3-7.
(302) Oates, T. W. H.; Wormeester, H.; Arwin, H. *Prog. Surf. Sci.* **2011**, *86*, 328-376.
(303) Dong, A.; Chen, J.; Vora, P. M.; Kikkawa, J. M.; Murray, C. B. *Nature* **2010**, *466*, 474-477.
(304) Henzie, J.; Grünwald, M.; Widmer-Cooper, A.; Geissler, P. L.; Yang, P. *Nature Mater.* **2011**, *10*, 1-7.
(305) Ramakrishna, S. A. *Rep. Prog. Phys.* **2005**, *68*, 449-521.
(306) Naik, G. V.; Kim, J.; Boltasseva, A. *Opt. Mater. Express* **2011**, *1*, 1090-1090.
(307) Grigorenko, A. N.; Geim, A. K.; Gleeson, H. F.; Zhang, Y.; Firsov, A. A.; Khrushchev, I. Y.; Petrovic, J. *Nature* **2005**, *438*, 335-8.
(308) Shevchenko, E. V.; Talapin, D. V.; Murray, C. B.; O'Brien, S. *J. Am. Chem. Soc.* **2006**, *128*, 3620-37.
(309) Tao, A. R.; Ceperley, D. P.; Sinsermsuksakul, P.; Neureuther, A. R.; Yang, P. *Nano Lett.* **2008**, *8*, 4033-8.
(310) Gwo, S.; Lin, M.-H.; He, C.-L.; Chen, H.-Y.; Teranishi, T. *Langmuir* **2012**, *28*, 8902-8.

(311) Fafarman, A. T.; Hong, S.-H.; Caglayan, H.; Ye, X.; Diroll, B. T.; Paik, T.; Engheta, N.; Murray, C. B.; Kagan, C. R. *Nano Lett.* **2012**.
(312) Ghosh, S. K.; Pal, T. *Chem. Rev.* **2007**, *107*, 4797-862.
(313) Garcia, G.; Buonsanti, R.; Runnerstrom, E. L.; Mendelsberg, R. J.; Llordes, A.; Anders, A.; Richardson, T. J.; Milliron, D. J. *Nano Lett.* **2011**, *11*, 4415-20.
(314) Fafarman, A. T.; Koh, W.-K.; Diroll, B. T.; Kim, D. K.; Ko, D.-K.; Oh, S. J.; Ye, X.; Doan-Nguyen, V.; Crump, M. R.; Reifsnyder, D. C.; Murray, C. B.; Kagan, C. R. *J. Am. Chem. Soc.* **2011**, *133*, 15753-61.
(315) Rosen, E. L.; Buonsanti, R.; Llordes, A.; Sawvel, A. M.; Milliron, D. J.; Helms, B. a. *Angew. Chem., Int. Ed.* **2012**, *51*, 684-9.
(316) Dintinger, J.; Mühlig, S.; Rockstuhl, C.; Scharf, T. *Opt. Mater. Express* **2012**, *2*, 269-269.
(317) Nikoobakht, B.; El-Sayed, M. A. *Chem. Mater.* **2003**, *15*, 1957-1962.
(318) Munechika, K.; Chen, Y.; Tillack, A. F.; Kulkarni, A. P.; Plante, I. J.-L.; Munro, A. M.; Ginger, D. S. *Nano Lett.* **2010**, *10*, 2598-603.
(319) Xie, F.; Baker, M. S.; Goldys, E. M. *J. Phys. Chem. B* **2006**, *110*, 23085-91.
(320) Fry, H. C.; Lehmann, A.; Saven, J. G.; DeGrado, W. F.; Therien, M. J. *J. Am. Chem. Soc.* **2010**, *132*, 3997-4005.
(321) McAllister, K. A.; Zou, H.; Cochran, F. V.; Bender, G. M.; Senes, A.; Fry, H. C.; Nanda, V.; Keenan, P. A.; Lear, J. D.; Saven, J. G.; Therien, M. J.; Blasie, J. K.; DeGrado, W. F. *J. Am. Chem. Soc.* **2008**, *130*, 11921-11927.
(322) Gole, A.; Murphy, C. J. *Chem. Mater.* **2005**, *17*, 1325-1330.
(323) Lanci, C. J.; MacDermaid, C. M.; Kang, S. G.; Acharya, R.; North, B.; Yang, X.; Qiu, X. J.; DeGrado, W. F.; Saven, J. G. *Proc. Nat. Acad. Sci.* **2012**, *109*, 7304-7309.
(324) Stewart, W. W. *J. Am. Chem. Soc.* **1981**, *103*, 7615-7620.
(325) Hovestreydt, E. *Acta Crystallogr. A* **1983**, *39*, 268-269.